

Imperial College London

Multiphysics Simulations of Fire inside the Cavity of a Facade

A thesis submitted in partial fulfilment of the
requirements for the degree of

Doctor of Philosophy

in

Mechanical Engineering

by

Benjamin Khoo Sheng Yeong

2022

Copyright

Benjamin Khoo Sheng Yeong, 2022

All rights reserved

Declaration of Originality

I declare that this thesis and the work described within have been completed solely by myself under the supervision of Prof. Guillermo Rein. Where others have contributed, or other sources are quoted, full references are given.

Benjamin Khoo Sheng Yeong

2022

Copyright Declaration

The copyright of this thesis rests with the author. Unless otherwise indicated, its contents are licensed under a Creative Commons Attribution-NonCommercial 4.0 International Licence (CC BY-NC).

Under this licence, you may copy and redistribute the material in any medium or format. You may also create and distribute modified versions of the work. This is on the condition that: you credit the author and do not use it, or any derivative works, for a commercial purpose.

When reusing or sharing this work, ensure you make the licence terms clear to others by naming the licence and linking to the licence text. Where a work has been adapted, you should indicate that the work has been changed and describe those changes.

Please seek permission from the copyright holder for uses of this work that are not included in this licence or permitted under UK Copyright Law.

ABSTRACT

Multiphysics Simulation of Fire inside a Cavity of a Flammable Facade

by

Benjamin KHOO Sheng Yeong

Doctor of Philosophy in Mechanical Engineering

Imperial College London, 2022

Supervised by Prof. Guillermo Rein

The facade system is highly complex and requires achieving multiple objectives to provide occupants with a safe and comfortable environment. Any attempt to improve these objectives, such as aesthetic, thermal or acoustic insulation, could potentially affect the fire safety of the facade system. This is especially true as novel materials were introduced over the last decades, resulting in an ongoing rise in facade fires. Researchers have observed that a narrow cavity in a facade system encourages rapid facade fire spread. Unfortunately, there is little knowledge of quantifying the impact of cavities on a facade fire.

Computational Fluid Dynamics (CFD) fire simulation represents an excellent tool to complement experimental studies on fire inside a narrow cavity of a flammable facade. Cavity fire is a multiphysics phenomenon, and all physics, i.e. fluid flow, heat transfer, buoyancy, combustion and pyrolysis involved in the model must be coupled step-by-step for a narrow cavity fire scenario to ensure model reliability. This thesis provides a step-by-step development of a CFD simulation for a narrow cavity fire. We split the facade cavity fire into six different scenarios with increasing complexity and validated the model against experimental data in the literature to limit the compensation effect. The compensation effect is the concept where similar results could be obtained by varying two or more parameters. We studied how cavity barriers affect fire dynamics and performed parametric studies to quantify the impact of both material properties and cavity width on fire dynamics inside a cavity of a flammable facade. This work demonstrates that modelling represents a powerful tool to aid in understanding facade cavity fire to improve building fire safety.

ACKNOWLEDGEMENTS

In the past four years that it took for me to finish this thesis, I have received invaluable help and advice from friends, family, and colleagues. I would love to take this opportunity to thank everyone whose help I have received.

First of all, I would like to thank EPSRC and Ove Arup and Partners for sponsoring my study. Without their financial support, I could not have started my journey in the fire safety field that I have grown to love.

I would like to thank my parents who have been extremely supportive of my studies and have been always checking on my health despite being halfway around the world. I would also like to thank my partner, Seiko who has patiently supported my endeavour and has been doing this over a long distance.

Thank you to all the friends I met in Hazelab who have continuously given me help and advice on my research. Special thanks to Matt, who has been helping me with all the research questions and also the fun times we have. Francesca, for all the joy she brings to the office and Harry, for the discussions we have on Friday to solve the research issue and have a laugh.

Lastly, I would like to thank my supervisor, for guiding me through not just all the hurdles in this research but for being more active in outreaching. Throughout my time in Hazelab, I have learned so much about fire safety, and the need to reach out to the public and talk about what we do. My time in Hazelab has been nothing more than great, as I have got the opportunity to travel around before COVID-19 Lockdown. I am truly grateful for the time I have had in Hazelab. Thank you!

TABLE OF CONTENTS

Chapter 1	1
1.1 Motivation and Background.....	1
1.2 Difficulty in predicting rainscreen facade flammability	4
1.3 Literature Review of Cavity Fires	6
1.4 Aim and Objectives.....	12
1.5 Layout of Thesis	12
Chapter 2	14
2.1 History	14
2.2 Timeline.....	17
2.3 How Did This Happen?	18
2.3.1 Prevention Layer.....	19
2.3.2 Detection Layer	23
2.3.3 Evacuation Layer	24
2.3.4 Compartmentation Layer.....	26
2.3.5 Suppression Layer.....	27
2.4 Has The Lesson Been Learned?	28
2.5 Conclusion	28
Chapter 3	29
3.1 Introduction.....	31
3.2 Methodology	32
3.3 Experimental Setup	35
3.4 Numerical Modelling.....	38

3.4.1	Turbulence.....	40
3.4.2	Wall Heat Transfer	42
3.5	Computational Domain and Boundary Conditions	43
Results.....		48
3.5.1	Scenario 1 – Fluid Flow Validation.....	48
3.5.2	Scenario 2 – Heat Transfer Validation	50
3.5.3	Scenario 3 – Buoyancy Validation	53
3.6	Conclusion	56
Chapter 4		58
4.1	Introduction.....	59
4.2	Experimental Setup for Validation.....	60
4.3	Numerical Modelling.....	62
	Combustion.....	62
	Radiation Heat Transfer	63
	Solid-Gas phase coupling	65
4.4	Computational Domain and Boundary Conditions	66
4.5	Results	69
	Flame Height	69
	Flame Shape	72
	Upward exit velocity.....	74
	Incident Heatflux to the near wall.....	76
4.6	Conclusion	81
Chapter 5		83
5.1	Introduction.....	84
5.2	Methodology and Numerical Method.....	85

5.3	Computational Domain and Boundary Conditions	86
5.4	Results	88
	Closed Side	88
	Cavity Barrier.....	96
5.5	Conclusion	102
Chapter 6		105
6.1	Introduction.....	106
6.2	Experimental Setup	107
	6.2.1 Material Properties	108
6.3	Numerical Methods	110
	Pyrolysis	110
	Radiation	111
	Convection	112
6.4	Computational Domain and Simulation Setup	113
6.5	Results	117
	Pyrolysis Kinetics	117
	Cladding Junction Gap.....	121
	Parametric studies	123
6.6	Conclusion	127
Chapter 7		129
7.1	Detailed conclusions	129
7.2	Suggestions for Future work.....	131
7.3	Significance of findings	132

LIST OF FIGURES

Figure 1.1 Example of two different external flame spread mechanisms. A combustible exterior enables secondary fires to spread rapidly across several storeys within a short time. (Source BRE [3]).....	2
Figure 1.2 The most basic setup of the rainscreen facade consists of cladding, insulation and substrate. Weather-resistant barriers and vapour barriers may be introduced to improve lifespan and performance. [4].....	4
Figure 1.3 Physical phenomena involved in a cavity fire, i.e. fluid flow, heat transfer, combustion, buoyancy and pyrolysis. These physical phenomena are strongly coupled and affect each other, creating a highly complex non-linear behaviour.	6
Figure 2.1. Plot of facade fires reported by the media. The numbers represent large fires that warrant reporting and do not represent all facade fires. 1990–2019[4].....	15
Figure 2.2 The red arrow represents the area where the fire was believed to first start (left) [62]. Extensive fire on the facade of Summerland after around 20 minutes. (right) [63].....	18
Figure 2.3. A simplified Swiss-cheese model shows how each fire protection layer works. These layers might not all be present in a building, but the presence of multiple layers improves overall fire safety [65].....	19
Figure 2.4 Oroglas and Galbestos were used extensively across Summerland’s facade [58].	21
Figure 2.5 Two types of façade on the Summerland building, Oroglas and Galbestos/Decalin (Decalin not always present) (left). Note that the cavity formed between Galbestos and Decalin encouraged fire spread (right) [52]	22
Figure 2.6 Photos taken after the fire show some exits are still locked and obstructed. (Source: Police Photographs, Isle of Man Public Record Office).....	25

Figure 2.7 Summerland was designed to have a single, large space with limited compartmentation [58].	26
Figure 2.8 The northeast service stairs, one of the supposedly compartmentalised stairways, was surrounded by Galbestos (orange line), which is flammable (Source: Report of the Summerland Fire Commission)	27
Figure 3.1 The different physical phenomena involved in a cavity fire validated in 5 scenarios. Each physical phenomenon interacts with the other in the facade cavity to create a non-linear fire behaviour.	35
Figure 3.2 Simplified Schematic of Scenario 1 to Scenario 3. Each scenario represents one of the multiple physical phenomena the model intends to validate. The bracketed term is hereby used to refer to each scenario. Dimensions are in mm	37
Figure 3.3 Grid sensitivity analysis for Scenario 1. The comparison shows the minimal difference between mesh sizes for predicted mean velocity and turbulent velocity fluctuation. A slightly more significant difference is observed for the log law profile between the mesh sizes.	44
Figure 3.4 Grid sensitivity analysis for Scenario 2. The comparison shows minimal differences between mesh sizes for predicted mean velocity and temperature predictions.	45
Figure 3.5 Grid sensitivity analysis for Scenario 3. For Coarse mesh, simulation results show that huge differences are recorded when compared to both Medium and Fine mesh. The Medium mesh was chosen for validation due to negligible differences between the Fine mesh.	46
Figure 3.6 Setup of the simulations of the three Scenarios. Mesh refinement was present near the wall where cell size is halved in the normal direction.	47
Figure 3.7 Predicted a) wall normal variation of the mean velocity profile b) log law velocity profile c) Dimensionless velocity intensity profile d) Dimensionless velocity intensity profile near the wall of Scenario 1. The simulation result shows that all turbulence models accurately predict flow velocity in a narrow cavity.	49
Figure 3.8 Simulation results of Scenario 2 where a) All turbulence models captured the mean velocity and temperature profile with good accuracy. b) vanishing value of SGS viscosity at the wall was only predicted accurately by the WALE model	50

Figure 3.9 Simulation results of Scenario 2 were a) dimensionless mean temperature distribution. b) non-dimensional r.m.s temperature distribution model. The prediction shows that the WALE model performs slightly better near.....	52
Figure 3.10 Comparison of experimental and predicted velocity profiles for cavity widths of $W = 50$ mm, 100 mm, and 200 mm at the height of 3,865 mm for $q_w = 208 \text{ W m}^{-2}$. The model could capture the general velocity profile, although velocity tends to be overestimated near the wall.	53
Figure 3.11 Comparison of experimental and predicted heated wall temperature of a) 50 mm, b) 100 mm, and c) 200 mm cavity for $q_w = 104 \text{ W}$. The model captured the general trend, but local maxima tend to be predicted slightly higher up	54
Figure 3.12 Comparison of experimental and predicted velocity intensity profile for cavity widths of (a) 100 mm and (b) 200 mm velocity and (c) temperature intensity profile when $q_w = 104 \text{ W m}^{-2}$ at the height of 3865 mm for a cavity width of 100 mm. The model was able to capture the general trend of the turbulent characteristic.....	55
Figure 4.1 The time scales and length scale needed to resolve the required combustion phenomenon. As the engineering scale is of interest, there is no need for the model to resolve the chemical kinetics where a tremendous requirement is needed for both the time scale and length scale. (Source: [102])	60
Figure 4.2 Simplified schematic of the experimental setup of Livkiss et al. used to validate the combustion model [28]. The model is validated with cavity widths of 40 mm, 50 mm, 60 mm and 100 mm.....	61
Figure 4.3 Ray effect on the far war when 32 solid angles are used (left) and 112 solid angles are used (right).....	65
Figure 4.4 Comparison of incident heat flux between the three different mesh sizes. Results show that Coarse mesh underpredicts lower region significantly. Medium and Fine mesh was able to resolve the predicted heat flux more at this region.....	67
Figure 4.5 Computational Domain of Scenario 4. The size and location of the mesh refinement are as shown with further refinement applied near the panel where cell size was halved in the normal direction.	69

Figure 4.6 Comparison of flame height using three criteria: Stoichiometric Mixture Fraction, 99% cumulative HRR and $\Delta T = 550$ K. The comparison showed $\Delta T = 550$ K tends generally predict a higher flame height, while stoichiometric mixture fraction and 99% cumulative HRR predict a similar flame height.....	70
Figure 4.7 Comparison of Livkiss's experiments and prediction for the flame height where burner HRR is a) 6.5 kW and b) 12.9 kW. The model consistently underpredicts the flame height by an average of 14.9%, but the reduction of flame height with increasing cavity width is predicted well.	71
Figure 4.8 Comparison of flame height with both Livkiss et al. and Karlsson et al. experimental measurements [8, 16]. The model prediction is within the measurement of both data sets, suggesting that the model may be suitable for predicting flame height for different cavity configurations.	72
Figure 4.9 Instantaneous at $t = 40$ s (left) and average (right) flame shape for HRR of 6.5 kW for a cavity width of a) 40 mm and b) 60 mm. Simulation shows that the predicted flame shape is different as cavity width changes.	73
Figure 4.10 Streamline of average air entrainment from the sides for burner HRR of 12.9 kW for 40 mm and 100 mm cavity width at the height of 0.4 m above the burner. The air entrainment creates a circulation at the centre that moves the fuel away from the centre. This resulted in the flame being observed as two peaks.	74
Figure 4.11 Comparison of Scenario 4 result and experimental upward exit velocity data at various locations at the cavity for a cavity width of 40 mm with Burner HRR of a) 6.5 kW and b) 12.9 kW. Although underpredicted, the simulation results capture the general trend of the experimental data.	75
Figure 4.12 Comparison of experimental total heat flux to Scenario 4 prediction of HRR = 6.5 kW for a cavity width of a) 40 mm b) 50 mm c) 60 mm and d) 100 mm. A good match to experimental data was found qualitatively and quantitatively for varying cavity widths. ..	76
Figure 4.13 Comparison of experimental total heat flux to Scenario 4 prediction of HRR = 12.9 kW for a cavity width of a) 40 mm b) 50 mm c) 60 mm and d) 100 mm. The prediction was found to match the experimental data less at lower elevations.....	77

Figure 4.14 Vortical structure of the flame using Iso-contour of Q , $Q=1000 \text{ s}^{-1}$ - based on Ren et al. [45]. (Left) The iso-contour of Q using the Medium mesh shows turbulence inception occurs around 0.45 m. (Right) The iso-contour of Q using the Fine mesh shows turbulence inception occurs around 0.20 m.....	78
Figure 4.15 Comparison of Convective Heat Flux predicted by different mesh sizes in Scenario 4 and simulation by Livkiss. Results show that a finer grid predicts the laminar convective heat transfer better.	79
Figure 4.16 Incident heat flux for burner HRR of 12.9 kW at cavity widths of 40 mm, 50 mm, 60 mm, 80 mm and 100 mm. The results show that the height of the incident heat flux contour reduces with cavity width.	80
Figure 5.1 The numerical setup for the cavity with a closed side and the cavity barrier case. For cavities with closed sides, cavity widths of 40, 50, 60, 80, and 100 mm are studied. As for the cavity barrier case, a cavity width of 40, 60 and 100 mm was studied with three different gaps between the panel and the cavity barrier.	86
Figure 5.2 Flame height for closed sides is generally higher than for open sides. One reason for this increase is due to increased air entrainment velocity.	89
Figure 5.3 Continuous flame shape using stoichiometric mixture fraction for a closed side with a cavity width of a) 40 mm and b) 50 mm for HRR 6.5 kW (Left) and 12.9 kW (Right). The simulation results show that when the sides are closed flame is asymmetrical.	89
Figure 5.4 Time-average airflow in open-sided (left) and closed-sided (right) scenarios. Flames are symmetrical in an open-sided cavity, but not when the sides are closed.	90
Figure 5.5 a) 6.5 kW HRR, b) 12.9 kW HRR, at cavity width smaller than 60 mm, the incident heat flux was observed to have increased.....	91
Figure 5.6 a) 6.5 kW HRR, b) 12.9 kW HRR, at a wider cavity width, the increase in the incident heat flux was insignificant. This is likely due to the reduced chimney effect.	92
Figure 5.7 Incident heat flux contour for 40 mm cavity width at a)HRR 6.5 kW and b) HRR 12.9 kW. The left image represents a cavity with open sides, while the right image represents a cavity with closed sides.	93

Figure 5.8 Incident heat flux contour for 100 mm cavity width at a)HRR 6.5 kW and b) HRR 12.9 kW. The left image represents a cavity with open sides, while the right image represents a cavity with closed sides.	94
Figure 5.9 Cavity width of (clockwise from top left) 40mm, 60mm and 100mm. Flame height was observed to reduce with the presence of a cavity barrier generally.....	96
Figure 5.10 Airflow within the cavity is choked due to the presence of the cavity barrier. Flow circulation is observed near the cavity barrier, which affects the flame height even if it is below the barrier.....	98
Figure 5.11 Incident Heat flux measured at the centre of the rear wall. From top to bottom, the cavity widths are 40, 60, and 100 mm. Column (a) represents HRR 6.5 kW, and column (b) represents HRR 12.9 kW.....	99
Figure 5.12 Incident heat flux contour for 40 mm cavity width with various cavity barrier gaps at HRR 12.9 kW, a) Open, b) 20 mm, c) 10 mm, d) 4mm. The two black lines across the rear wall represent the location of the cavity barrier.	101
Figure 5.13 Incident heat flux contour for 60 mm cavity width with various cavity barrier gaps at HRR 6.5 kW, a) Open, b) 30 mm, c) 6 mm, d) 4mm. The two black lines across the rear wall represent the location of the cavity barrier.	102
Figure 6.1 General test setup arrangement based on ISO 13785-1. The dimensions of the facade system are as prescribed in the standard. [118], while the location of the panels, cavity width and cavity barrier and sensors are as defined by Guillaume et al. [27]. L1-L5 and S1-S5 are thermocouples embedded in the PIR, while LC1-LC2 and SC1-SC2 are suspended at the centre of the cavity.....	109
Figure 6.2 (Left) PIR temperature at the centre of the long wall at height 1.0 m. (Right) convective heat flux along the centre of the long wall. Results show that mesh sizes influence the result significantly at a lower height.	114
Figure 6.3 Computational Domain of Scenario 5 with Medium grid size (12.5 mm). The size and location of mesh refinement are as shown with further refinement at the PIR insulation and cladding, where the mesh size is halved to 6.25 mm.	114

Figure 6.4 The estimated pyrolysis kinetic of PIR in a nitrogen atmosphere obtained via inverse modelling. Note that mass loss rates between the two PIRs are drastically different due to fire retardants in PIRa.	117
Figure 6.5 Comparison of Temperature Prediction by different pyrolysis Kinetics. a) The PIR temperature at L1, L2 and L3 b) The predicted air temperature in the cavity. Plots on the left do not use the convective wall function, while plots on the right use the convective wall function.	119
Figure 6.6 The predicted HRR in Case 1-4 compared to the experimental results. The pyrolysis kinetics has a huge influence on the overall PIR HRR, although results are still greatly underpredicted compared to experimental results.	120
Figure 6.7 The results show the predicted temperature with and without the gaps between the cladding modelled. Simulation results show significant differences between the two, especially for prediction at the back wall.....	122
Figure 6.8 Flame shape in the cavity observed in the experiment, simulation without cladding junction gap, and simulation with cladding junction gap. Simulation shows that when the gap is present, the flame is split at the centre, potentially due to poorly resolved flow through the gap	123
Figure 6.9 The PIR HRR over 100s and the average HRR with various ΔH_c . The simulation results suggest that ΔH_c does not increase the pyrolysis rate of the panel, as seen in the linear increase of HRR with increasing ΔH_c in the current simulation settings.	124
Figure 6.10 Predicted incident heat flux for $\Delta H_c = 26 \text{ MJ kg}^{-1}$, 46 MJ kg^{-1} and 56 MJ kg^{-1} . Results show that with increasing ΔH_c , the incident heat flux on the PIR foam increases.	125
Figure 6.11 HRR contributed by the insulation with increasing cavity width. Simulation results suggest that at $\Delta H_c = 26 \text{ MJ kg}^{-1}$, cavity width has little effect on the over HRR. However, for $\Delta H_c = 36 \text{ MJ kg}^{-1}$, the effect of the cavity is slightly more pronounced, with a 5% HRR drop from a cavity width of 50 mm to 62.5 mm.	126
Figure 6.12 Predicted Incident Heat flux on the PIR foam at L1, L2 and L3. The simulation results show that while the predicted heat flux at L1 increases with cavity width, L2 and L3 do not decrease with cavity width.....	127

Figure 7.1 Hypothetical facade with different materials and facade configurations. At different cavity widths, these facade materials may perform differently due to different materials used in the construction.....	133
--	-----

LIST OF TABLES

Table 2.1 The list of high-rise facade fires from 1990 to 2020. This is a partial list that Bonner compiled by searching through news reports and research literature [53]. The incidents may therefore be more biased toward large fires.	16
Table 2.2 Bye-laws of Interest and the Materials Each Would Have Restricted.....	20
Table 3.1 Summary of the numerical settings for Scenario 1 – 3 and Reynolds number involved in each scenario. Note that Reynold numbers in Scenario 3 are not known as fluid flow is caused by buoyancy.....	47
Table 3.2 Mean Relative error and bounded relative error for Scenario 1 over the various measurements. Smagorinsky and K-equation model performs slightly better due to the Van Driest wall function.	49
Table 3.3 Mean Relative error and bounded relative error for Scenario 2 over the various measurements. WALE model performs better likely due to better prediction of v_{sgs} near walls	52
Table 3.4 Mean Relative error and bounded relative error for Scenario 3 over the various measurements. After the addition of buoyancy, the relative error increased drastically.	55
Table 4.1 Sensitivity analysis on the effect of radiant fraction.....	65
Table 4.2 The total numerical cell for gas and solid phases at different cavity widths.....	68
Table 4.3 Mean Relative error and bounded relative error for Scenario 4. Good accuracy was measured for flame height and velocity. However, relative errors for heat flux measurements are high.....	81
Table 5.1 Description of the cases investigated in the CFD analysis.	87
Table 6.1 Material thermal properties and their corresponding pyrolysis kinetics.	108
Table 6.2 Effect of the radiant fraction on heat flux and insulation HRR predictions.....	111
Table 6.3 Summary of the cases investigated with their respective settings.	116

NOMENCLATURE

Symbols

α	Thermal Diffusivity
C	Model Constant
c_p	Specific Heat Capacity
Δ	Cube root of grid volume
E	Experimental Value
g	Gravitational acceleration
ΔH_c	Heat of Combustion
I	Radiation Intensity
k	Thermal conductivity
k	Kinetic energy
χ	Radiative fraction constant
M	Predicted Value

\dot{m}	Mass flow rate
ν	viscosity
$\dot{\omega}$	Rate of reaction
p	Pressure
ϕ	General symbol in transport equation
$\tilde{\phi}$	The filtered general symbol in the transport equation
Pr	Prandtl Number
q	Heat flux
q''	Heat flux
R	Universal Gas constant
r	stoichiometric oxygen-to-fuel mass ratio.
RE^b	bounded relative error
RE^m	Mean relative error
ρ	Density

T	Temperature
T_τ	Friction Temperature
τ_{ij}	viscous stress tensor
θ	Excess Temperature
\mathbf{i}	velocity
U^+	Dimensionless Velocity
\bar{U}	Mean velocity
U_τ	Friction velocity
W	Cavity width
y^+	dimensionless wall distance
γ	Species Mass Fraction

Superscripts

'	Fluctuation
''	Flux

SGS	Subgrid-scale
-------	---------------

Subscripts

c	convective
-----	------------

f	fluid
-----	-------

F	fuel
-----	------

in	Incident
------	----------

O_2	Oxygen
-------	--------

pyr	pyrolyzate
-------	------------

r	radiative
-----	-----------

s	solid
-----	-------

sgs	Subgrid-scale
-------	---------------

v	Virgin material
-----	-----------------

w	Heated wall heat flux
-----	-----------------------

Abbreviations

ACM	Aluminium Composite Material
CFD	Computational Fluid Dynamics
DNS	Direct Numerical Simulation
EPS	Expanded Polystyrene insulation
FDS	Fire Dynamic Simulator
fvDOM	Finite Volume Discrete Ordinates Model
HRR	Heat Release Rate
LES	Large Eddy Simulation
PIR	Polyisocyanurate
PIR	Polyisocyanurate
RANS	Reynolds-Averaged Navier Stokes
RTE	Radiative transport equation
SGS	Subgrid-scale

SSFT	Simplified Stagnant Film Theory
TGA	Thermogravimetric Analysis
TRI	turbulent radiation interactio
TSC	Thin Skin Calorimeter
WALE	Wall adapting local eddy-viscosity

PREFACE

This thesis contains 7 Chapters. Chapter 1 provides an introduction and context to the thesis. Chapter 7 provides an overall conclusion to the thesis. The other chapters are either based on a published manuscript, submitted manuscript or partially completed manuscript that will be submitted for publication.

Chapter 2 is based on the published article to SFPE magazine:

B. Khoo, G. Rein, Building Fire Protection layers – How They Failed in the 1973 Summerland Fire, Fire Protection Engineering, (93), (ISSN 1524-900X)

Chapter 3 is based on a submitted paper to Fire Technology:

B. Khoo, W. Jahn, M. Bonner, P. Kotsovinos, G. Rein, Step-by-Step Development of Multiphysics Simulation in a Narrow Cavity fire.

Chapter 4 is based on a submitted paper to Fire Technology:

B. Khoo, W. Jahn, M. Bonner, P. Kotsovinos, G. Rein, Step-by-Step Development of Multiphysics Simulation in a Narrow Cavity fire.

Chapter 5 is based on a paper in progress:

B. Khoo, W. Jahn, P. Kotsovinos, G. Rein, Effect of Cavity Barriers inside the Narrow cavity of a Facade.

Chapter 6 is based on a paper in progress:

B. Khoo, W. Jahn, P. Kotsovinos, G. Rein, Addition of Pyrolysis Model inside the Narrow Cavity of a Flammable Facade.

Chapter 1

Introduction to Facade Cavity Fires

1.1 Motivation and Background

Building facades are often one of the most expensive and complex components in a building and can cost up to 25% of the total cost [1]. This is due to the multiple objectives it needs to achieve to provide an aesthetically pleasing, comfortable, and safe environment. Unfortunately, these objectives are not independent, and improving one objective can often negatively impact another. As a result, practitioners often struggle to optimise all objectives required of a facade design.

A major concern for practitioners is the fire safety of a facade system. Fire can spread externally from one storey to another through the “leap frog” effect. The “leap frog” effect refers to a mechanism where a fully developed fire from lower storeys ignites combustible material behind the upper storey window. This would result in flame spreading to the upper storey, and once the fire is fully developed in the upper storey, the same mechanism repeats itself to spread fire to the next storey. However, as it takes time for the flame to develop and spread to the next storey, rapid flame spread via the ‘leap frog’ mechanism is often limited. Another mechanism for flame spread over the building facade is through combustible materials on the facade [2]. This occurs when flames ignite the combustible facade and can spread along the building facade. As a result, the fire could spread to multiple storeys simultaneously, severely compromising one of the six layers of building fire protection: compartmentation (limit fire spread from the room of origin), as shown in Figure 1.1. The failure of compartmentation could endanger occupants in a high rise as the time available for the building to be evacuated and for the fire brigade to intervene is drastically reduced.

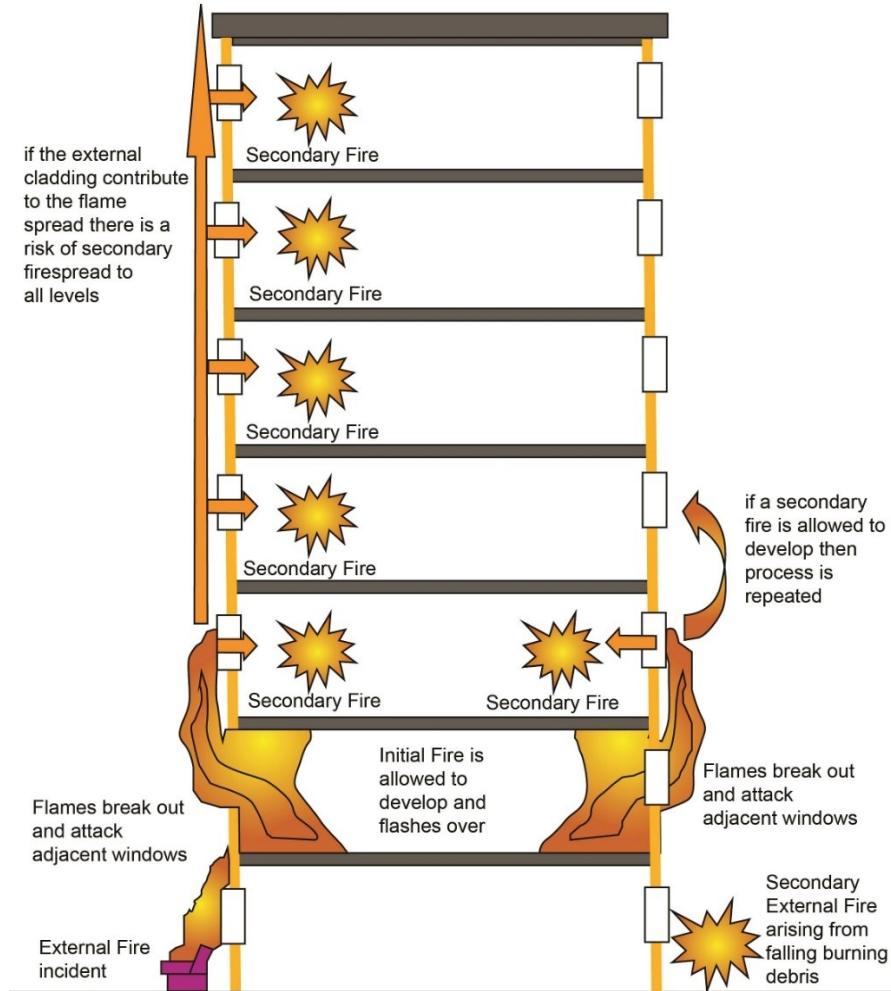


Figure 1.1 Example of two different external flame spread mechanisms. A combustible exterior enables secondary fires to spread rapidly across several storeys within a short time. (Source BRE [3])

According to Bonner et al. [4], facade fires involving flame spread have increased in recent years, with an annual average of 4.8 fires worldwide. In addition, they have also found that these fires are often more severe in modern facades because facade systems are becoming more flammable [5]. Historically, flame spread via building exteriors is minimised by restricting combustible material on the exterior walls to only buildings below 18 m[6]. However, since the energy crisis in the 1970s, buildings have been encouraged to have high heat insulating value to improve energy efficiency. This has increased pressure on regulators to change the building code to permit better-performing but combustible insulations on the exteriors of highrise buildings. To accommodate combustible materials on the building exterior without compromising safety, building codes around the world

often require the facade system to pass relevant facade tests [7]. However, these tests can be unreliable and may not represent a realistic fire scenario as the test assumes the facades would be installed without mistakes and also does not require weak points such as vents and ducts to be evaluated [8].

It is not unusual that a building requires several facade configurations to achieve specific objectives, such as achieving a certain aesthetic or improving lighting comfort. In such cases, the fire safety of each configuration would need to be evaluated individually with a large-scale fire test, and the cost could run up to hundreds of thousands of pounds. To reduce the number of large-scale facade tests, approval for some configurations could be obtained via assessment using previously tested systems with a similar configuration. After the Grenfell Tower fire in 2017, there has been much discussion on the suitability of approving facade systems based on these assessments. These assessments, also known as “Desktop Studies”, are often performed based on expert judgment. These assessments are criticised because they lack clarity on when they can be used and who is qualified to make them [4]. Furthermore, details on those who made the assessment are often not made public, even to the relevant authority. After the 2017 Grenfell fire, an independent review of the building regulation in the UK resulted in no combustible materials and desktop studies allowed for building facades for new buildings over 18 m containing flats, hospitals, and care premises in the UK [9, 10]

One of the key reasons that desktop studies are unreliable is the lack of established theories on fire dynamics on building facades. Instead, experts had to rely on their experience, which has no rigorous scientific basis when making these assessments. As a result, achieving consistent assessments is challenging. The banning of desktop studies has stopped unsafe facades from being installed on newer buildings. However, the lack of scientific literature on facade fires remains an obstacle for practitioners to design safe facades consistently. Therefore, improving our understanding of facade fire dynamics may be essential in improving facade fire safety. In this work, the focus will be placed on understanding the fire dynamics on the rainscreen facades.

1.2 Difficulty in predicting rainscreen facade flammability

One popular facade system is the rainscreen facade, where the most basic build-up consists of cladding, cavity, and insulation, as shown in Figure 1.2. The cladding refers to the outermost layer of the rainscreen facade, which protects the insulation from environmental damage and provides aesthetics to the building. The cladding can be made up of various materials such as metal, composite, polymer or a combination of the three materials. Depending on the makeup of the panels, the cladding can sometimes be combustible and promote flame spread via the building's exterior. An example of combustible cladding is the polyethylene aluminium composite panel (PE ACP), where polyethylene is sandwiched between two aluminium panels to provide a light and rigid structure.

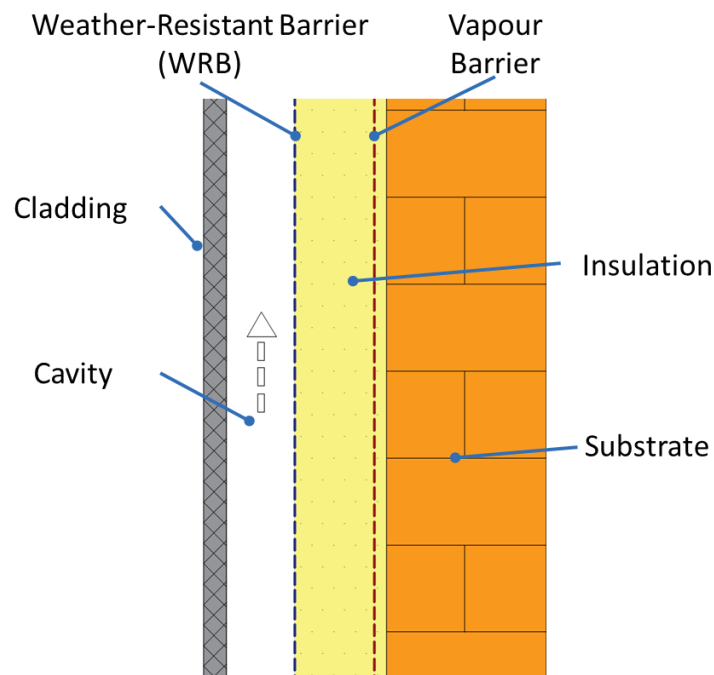


Figure 1.2 The most basic setup of the rainscreen facade consists of cladding, insulation and substrate. Weather-resistant barriers and vapour barriers may be introduced to improve lifespan and performance. [4]

The cavity is essential in allowing air to ventilate and remove moisture from the insulations, prolonging the insulations' lifespan by reducing degradation by water damage. However, a facade cavity may introduce an alternative path for spreading fire and smoke on a building [11–13]. Studies have also found that as flames enter a facade cavity, the

pressure difference inside and outside the cavity induces the chimney effect, which increases the upward buoyant flow. This process can extend the flame height by up to ten times, breaching building compartmentation even when the facade system is constructed with non-combustible materials [4, 14]. In addition, as the cavity width reduces, the heat flux on both cladding and insulation increases due to re-radiation, increasing fire spread risk. A cavity also allows fires to be concealed within it until it is well developed, reducing the time for occupants to evacuate, as observed in the Summerland Fire [15].

The insulation is the facade system component that provides improved heat insulation to the building. As aforementioned, the 1970s oil crisis resulted in demands for more energy-efficient buildings. This increased the drive to install insulation on newer buildings and to retrofit older ones with insulation. These insulations are typically made of minerals or polymers, of which the latter are combustible. Generally, mineral insulations are fire-safe but have lower insulation performance, resulting in a thicker construction which requires more building space [16]. The more efficient polymer-based insulations reduce the space needed, although they introduce fire hazards to the system.

As there are many possible facade configurations and various materials to choose from to construct a facade system, it is clear that predicting rainscreen facade flammability is not trivial [4]. The flammability of a facade system is a multiphysics problem where five physical phenomena, fluid flow, heat transfer, buoyancy, combustion and pyrolysis, are strongly coupled, as shown in Figure 1.3. For example, as cavity width reduces, heat flux on the cladding and insulation increases due to re-radiation. This, in turn, increases the pyrolysis rate, which potentially results in a more combustion facade system. However, as the pyrolyzate increases, more air entrainment into the cavity may be required to sustain combustion, which a narrow cavity, defined in this thesis as between 25 mm to 200 mm, may not be able to provide. Therefore, the cavity width effect on facade flammability does not exhibit a linear behaviour, as cavity width can drastically affect the fire dynamic within the facade system. Furthermore, different cladding and insulation materials could affect the heat release rate (HRR) and the total heat released (THR) during combustion, further complicating the task of predicting facade flammability.

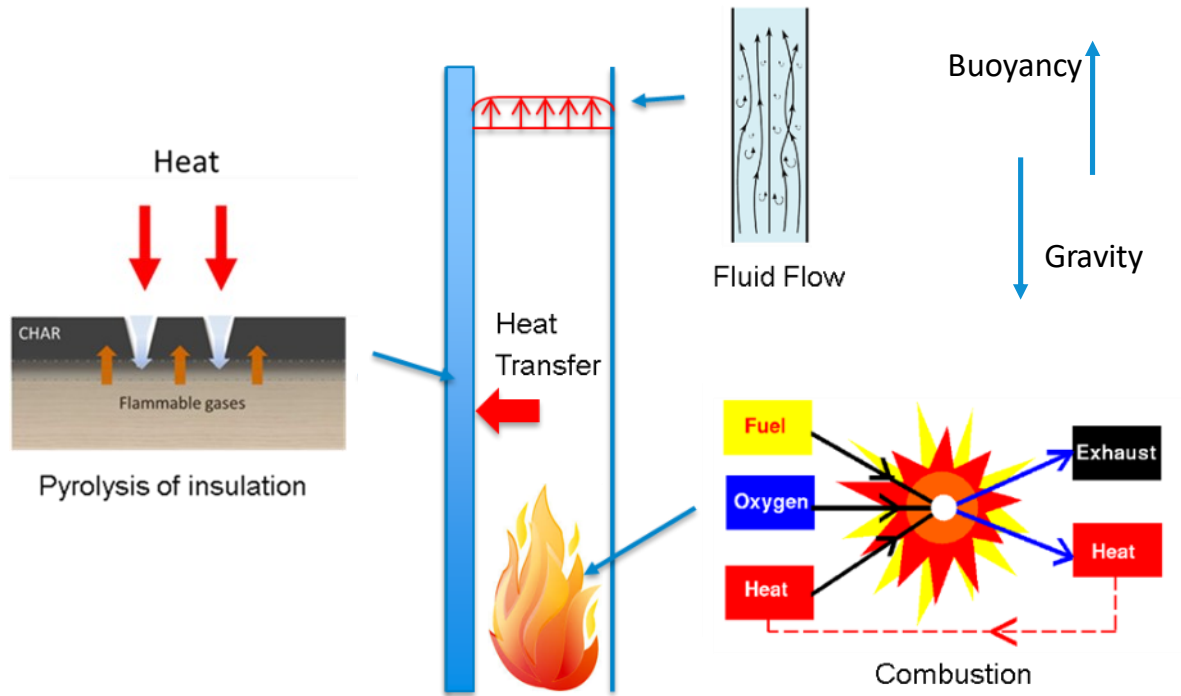


Figure 1.3 Physical phenomena involved in a cavity fire, i.e. fluid flow, heat transfer, combustion, buoyancy and pyrolysis. These physical phenomena are strongly coupled and affect each other, creating a highly complex non-linear behaviour.

It is clear that facade cavities introduce additional fire hazards to a building, especially when combustible materials are used. Without well-established theories to quantify the effect of cavity width on the facade cavity fire, it is difficult for practitioners to design a fire-safe facade system that satisfies the many objectives a facade system needs to achieve. Hence, there is a need for further research into the fire dynamic within a facade cavity.

1.3 Literature Review of Cavity Fires

One approach to developing our understanding of the effect of cavities on fire dynamics is to perform experimental studies where multiple parameters such as cavity width, type of insulation and cavity barriers are tested. These experimental studies intend to understand how facade systems behave with different cavity widths and facade buildup materials. Practitioners can then incorporate this knowledge into the design of facade systems. Lie performed one of the first studies on facade cavities in 1972 [17]. He used a channel that was 2.34 m tall and 0.91 m wide. Three of the four walls within the cavity are inert, and

one is attached with combustible insulation. At the bottom of the channel, a furnace is used to simulate a fire source. In this study, he found that the rate of flame spread within the cavity is dependent on the insulation material.

Further work on the effect of cavity width by Choi and Talyor found a critical width for continuous fire spread [18, 19]. The studies found that when the cavity width is sufficiently narrow, air entrainment into the cavity becomes insufficient, suffocating and preventing further combustion [19]. Experimental studies on rack storage mock-ups which are geometrically similar to a facade cavity were also investigated by several researchers [20–22]. Their study found that the width between storage racks influenced flame height and highlighted that different fuels have an impact on the heat flux measured.

Several researchers have also investigated the heat transfer mechanism in a cavity fire [12, 22–26]. Their studies found that heat transfer to cavity walls increases as cavity width reduces. They concluded that this is due to increased re-radiation between the cavity walls and increased convective heat transfer as a result of changes to the airflow into the cavity. Foley et al. [25] investigated the effect of cavity width with two parallel inert walls with open sides. They found that heat transfer becomes more sensitive to cavity width if only the base is sealed due to higher air entrainment velocity from the sides. The air entrainment from the side pushed the flames towards the centre, resulting in higher heat flux. They also found that the position of the burner between the walls affected the measured heat flux on the cavity walls, where it does not simply reduce when placed further from the measured wall. An investigation by Guillaume et al. [27] using an intermediate scale test found that combustible claddings can play a pivotal role in flame spread. They found that heat flux on the wall changes drastically depending on the combustibility of the claddings, and cavity barrier effectiveness reduces if the cladding panels are degraded or burnt away.

More recently, Livkiss et al. [28] used two inert parallel walls with open sides to investigate the effect of narrow cavity width on flame height and incident heat flux on a non-combustible panel. In this study, the burner power per burner length, Q' , was varied between 16 kW/m to 40.4 kW/m, and the cavity width, W , was varied between 20 mm and 100 mm. The experiments found that flame heights were relatively constant when $Q'/W < 300 \text{ kW/m}^2$. However, as Q'/W increases above 300 kW/m^2 , flame height was observed to

have increased by up to 2.2 times compared to open fire. The study also showed that incident heat flux on the all increases as the cavity width decreases.

While studies [12, 23–25, 28] suggest that reducing cavity width would increase incident heat flux on the facade cladding and insulations, a narrow cavity does not always result in the most severe fire. For example, a study by Jamison et al. found that a facade system with combustible insulation produces a more severe fire when the cavity is wider [29]. In this study, Jamison et al. experimented with a parallel panel with insulation installed on one panel with the HRR of the burner set to 323 kW/m² of the sand burner's surface area. The experiment is conducted with a cavity width of 51 mm or 102 mm with open sides. The result suggests that a wider cavity results in a higher peak HRR in the facade system due to increased air entrainment to support more combustion in the cavity.

These experimental studies suggest that the facade cavity fires problem is complex, and fire dynamics within the facade cavity do not behave linearly with increasing cavity width. Therefore, more experiments are needed to improve our understanding of how cavity width affects fire dynamics. However, one of the main challenges in conducting these experiments is the high cost and the time needed to set up the experiment. While predicting fire scenarios using a different smaller-scale experiment is a plausible option [30, 31], scaling methods requires great care, as perfectly preserving all dimensionless groups across scales is unlikely. However, with sufficient experimental data and a good understanding of the main phenomena in a given scenario [32], hand-calculated methods using scale modelling can estimate a specific fire effect using empirical correlations to yield good results. For example, McCaffrey, Quintiere and Harkleroad (MQH) method was developed from experimental observations that allow users to calculate the temperature increase in a pre-flashover room [33]. These methods are time efficient, and engineers can use these methods as preliminary calculations. However, hand-calculated methods are unsuitable for time-dependent analysis where highly coupled physical phenomena are present. However, the lack of empirical correlation and large-scale experimental data for facade fire makes scale modelling unsuitable for studying the fire dynamics within the facade cavity.

An alternate method to studying the effect of facade cavities is to use numerical methods to supplement experimental studies. Numerical studies can help to reduce the cost substantially when studying multiple parameters without substantially increasing

additional costs. Indeed, numerical methods have long been used to model fire behaviour for engineering purposes. Among the first models are zone models, where compartments are broken up into several zones or control volumes. Calculations were made between these zones to predict the overall fire effect in these volumes [34]. These models are transient and are suitable for probabilistic studies where zone-averaged output is sufficient to study a specific scenario. However, if the local effect of fire is of interest, zone models are unsuitable due to the large control volume used and the assumption that each zone's properties are uniform. These assumptions could lead to prediction errors, especially in facade cavity where fires are highly dynamic. One of the first models to study cavity-like fire was a two-dimensional zone model developed by Ingasson to study rack storage fire [21]. In this study, A simple 2D model was developed to predict flow velocity, flame height and temperature. While reasonable prediction for flow velocity and the temperature was obtained, the simplification and assumptions used in the model, such as a large control volume and no heat transfer to the wall, whilst allowing faster computation, have also affected the accuracy of flame height prediction due to poorer mass flow rate prediction.

A more suitable numerical method to investigate the fire dynamics within a cavity width is the field model, more widely known as computational fluid dynamics (CFD). In a CFD model, a computational domain is broken up into thousands or millions of small control volumes instead of just a few, as employed in zone models. The governing equations that describe mass, momentum, and energy transport via convection and diffusion are solved in each control volume, otherwise known as grids. In a large-scale fire such as a facade fire, heat transfer via the diffusive process can play a significant role, especially near a solid surface. Direct Numerical Simulation (DNS) can be used to fully resolve the fire near the solid surface without invoking any model to capture the small-scale diffusive process [35]. However, this technique requires a very fine spatial and temporal resolution that will require computational power that is often beyond the capabilities of a modern computer.

An alternative to DNS is RANS and LES, where subgrid-scale models are employed to predict small-scale diffusive processes smaller than the grid size. The RANS approach relies on averaging both spatial and temporal scales. As a result, the simulation requires significantly fewer computational resources than the DNS model. However, it is thought that the degree of time averaging by RANS may not allow for an accurate description of the

fire dynamics [36]. A study by Yan et al. [37] developed and validated a 3D RANS model for cavity fire. The model could reasonably reproduce the cavity width effect, although it underpredicts heat fluxes at the higher locations due to the poorly predicted buoyancy effect by the RANS turbulence model. In addition, the RANS model used in the study may not be suitable for cavity fire with combustible material as the time-averaged demanded by RANS does not allow for a good description of the fire dynamics.

On the other hand, LES employs only spatial averaging within the simulation. This allows for a more realistic-looking flow field than the time-averaged RANS model [35]. While LES is computationally more expensive than the RANS model, it is within the capabilities of modern computers. The LES model was first proposed by Smagorinsky in 1963 to predict atmospheric flow [38]. In fact, the early development and application of LES were made by the meteorological field to study atmospheric flow [39–41]. The first validation of the LES model for engineering application was performed by Deardorf in 1970, where he studied high Reynolds turbulent flow in a channel [42]. However, the development of the LES model at the time was slow due to limited computing power. As computing power increased over the years, LES development began to pick up in various fields, and in 1994, McGrattan et al. [43] provided a foundation for LES fire modelling by developing a 2D LES model using finite difference and vorticity stream function formula. While the 2D model is unsuitable for predicting turbulence, the model laid a foundation for the fire community to improve the model further to handle more complex phenomena. The model was eventually developed into the well-known Fire Dynamic Simulator (FDS). As computing power increases, the use of LES models to study fire dynamics has become more common in the literature [13, 44–46].

LES could be a vital tool in investigating facade cavity fire where RANS temporal averaging may not be able to capture the potentially fast fire spread in a cavity fire. Examples of the LES model used for investigating cavity fire are the various numerical studies on smoke spread within the facade cavities [13, 47]. Their research focused on smoke spread within a large-scale double-skin facade with a cavity width of 0.5 m to 2.0 m. However, these models were not validated against experiment results and were only used to study the effect of varying cavity width qualitatively. More recently, Drean et al. used LES models to complement previous experimental findings on an intermediate-scale facade

cavity fire [48]. The model shows good overall agreements, but thermal degradation was modelled by assigning a specific burning rate when the material reaches a specified temperature. As a result, the model is only suitable for investigating material with poor fire performance that degrades rapidly, as it could not simulate the charring effect of the burning materials. Lastly, Livkiss et al. compared their LES simulation to their cavity fire experiment [49]. In this work, Livkiss et al. developed a guide for simulating facade cavity fire in FDS. The model shows a good agreement in flame height and velocity prediction, although combustion and radiation effects on the wall were not considered.

The development of these models is essential in creating a simulation to study the effect of cavity width on fire dynamics in cavity fire. However, as cavity fire is a multiphysics process, all relevant physical phenomena must be validated for a narrow cavity fire scenario to ensure the model is robust for extrapolation for different facade configurations. Current cavity fire models validate these physical phenomena all at once, creating a model that might not be reliable due to the compensation effect. The compensation effect is widely recognised in chemical kinetic studies where similar results could be obtained by varying two or more parameters [50]. This creates a perception that the model is robust when a combination of two or more wrongly set model parameters results in a fortuitous prediction. It is important to note that while the compensation effect in the chemical kinetic studies may refer to a strict linear correlation between the logarithm of the preexponential factor and activation energy, the effect of achieving fortuitous prediction by varying other model parameters is also observed on various scenarios. For example, Bal and Rein explored the effect of inverse modelling in pyrolysis with various parameters [51]. Their study demonstrated that the same set of experimental pyrolysis data could be achieved by calibrating various model parameters, including but not limited to density, thermal conductivity, activation energy, order of reaction and preexponential factor.

This concept could also be used to explain the challenge of predicting the fire dynamics within a facade cavity. In a facade cavity fire, each physical phenomenon involved could interact and affect each other. For example, the combustion process is affected by fluid flow as it affects the rate of fuel mixing. This, in turn, affects the heat flux on the combustible materials and therefore affects the rate of pyrolysis. Lastly, the amount of pyrolysis released into the cavity will affect the amount of combustion, affecting the fluid flow due to

changes in the temperature and pressure in the cavity. From a modelling point of view, the compensation effect can be applied to cavity fire as each physical phenomenon present in the cavity could act as a model parameter. The same experimental data could be fortuitously predicted with multiple wrongly predicted physical phenomena due to their strong coupling. Therefore, validating all the submodels at once on a given experimental data may give false confidence in the model as the prediction can be obtained through multiple wrongly predicted physical phenomena

1.4 Aim and Objectives

This research aims to understand the potential danger of facade cavity fire and study how different parameters could affect fire dynamics in the cavity and the limitation of current CFD models in predicting facade fire. To achieve this goal, several objectives were set: 1) Perform a case study on the Summerland fire [52] to understand how a combination of cavity fire and poor fire safety strategy resulted in a loss of life, 2) Develop a numerical methodology to limit compensation effect during the simulation of facade cavity fire. 3) Perform validation of fluid flow, heat transfer and buoyancy in a cavity scenario, 4) Perform validation of combustion model in narrow cavity fire scenarios, 5) Extrapolate the model to study the effect of cavity barrier on fire dynamics in a cavity, and 6) Explore the current limitation of the pyrolysis model when simulating a cavity fire scenario and study the effect of different facade configuration on fire dynamic in a cavity.

1.5 Layout of Thesis

Chapter 2 presents a case study on the Summerland Fire. In this chapter, I looked into the shortcomings of Summerland's fire protection layers and drew parallels between some of the failures still found in the building industry. The findings in this chapter will help form an understanding of how a combination of cavity fire and failure of building fire safety layer could endanger occupants

Chapter 3 presents the methodology that is developed for validating the physical phenomena in a facade cavity fire. In this chapter, I have laid out the methodology to ensure the CFD model will be robust to study the effect of cavity width in a facade fire. The methodology involves validating one physical phenomenon at a time using experimental

data found in the literature to reduce the model's compensation effect. In this chapter, validation of fluid flow, heat transfer and buoyancy of FireFoam for a narrow cavity scenario is performed. The validation of these physical phenomena in a cavity scenario helps limit the number of degrees of freedom in subsequent chapters by validating one physical phenomenon at a time, hence allowing greater confidence in the model when it is extrapolated to study the effect of facade configuration.

Chapter 4 presents the validation of the combustion model of FireFOAM in a narrow cavity scenario. This chapter discusses the addition of combustions to the previously validated physical phenomena in a cavity fire scenario. The validation compared results on heat flux, flow velocity and flame height to ensure the model can accurately predict the fire dynamic within the cavity.

Chapter 5 presents a parametric study on the effect of cavity width, closed cavity sides to reduce air entrainment and partially closed cavity barrier using FireFoam. The results from these numerical studies are used to understand how facade cavity with closed sides and poorly installed cavity barriers would affect fire dynamics in a cavity.

Chapter 6 presents the limitation of the current CFD model on predicting facade fire. This chapter explores the limitations of the current pyrolysis model and how it affects the prediction of facade cavity fire. The study also explores the difficulty in modelling a realistic facade system due to the gaps between cladding. Finally, a parametric study was also used to explore the potential effect of varying cavity width on fire dynamics.

Chapter 7 presents the conclusion of this thesis and suggestions for future work. The chapter will discuss how numerical models could help understand fire dynamics in a cavity and the importance of improving the numerical models for cavity fire scenarios to help practitioners design a safer facade system.

Chapter 2

Building Fire Protection layers – How they failed in the 1973 Summerland Fire

Summary¹

On the 14th of June 2017 in London, a devastating fire broke out in Grenfell Tower, killing 72 people. The incident is the deadliest building fire in modern times. However, this was not the first facade fire that resulted in fatalities in the British Isles; the Summerland fire on the Isle of Man killed 50 people on the 2nd of August 1973 shares many similarities with the Grenfell fire. The Summerland building was a single, large, transparent structure with limited compartmentation. During the fire, the building lost five of the six fire protection layers: prevention, detection, evacuation, compartmentation and suppression, with only structural resistance not compromised. These layers were meant to work with each other to keep building users safe during a fire. Investigation into the incident found that these failures were primarily due to negligence resulting from the use of flammable materials, unauthorised modification of the building, and lack of staff training to deal with emergencies. As a consequence, the evacuation process was severely delayed, and fire brigades did not have much time to intervene to prevent the high death toll. The lessons from the past disaster must be learnt to avoid similar disasters in the future. Similar tragedies have repeated themselves and will continue to happen if lessons are not learnt from previous disasters.

2.1 History

Over the past decades, facade fire around the globe has been steadily increasing, as shown in Figure 2.1. Table 2.1 shows some of the high-rise fires taken from news outlets

¹ This chapter is based on the published article: B. Khoo, G. Rein, Building Fire Protection layers – How they failed in the 1973 Summerland Fire, Fire Protection Engineering, (93), (ISSN 1524-900X)

and literature from 1990 to 2020 by Bonner et al. [53]. The increase in high-rise fires has raised concern about the possible breach of compartmentation of high-rise buildings. Compartmentation, one of the six layers of fire protection, aims to contain the fire to its room of origin until the emergency service are able to arrive and extinguish it [54].

However, it is important to note that facade fires do not always result in fatal incidents. For example, previous incidents, such as the Lacrosse fire in Australia and The Marina Torch in Dubai, involved quick flame spread across the facade and had zero reported fatalities [55, 56]. This suggests that while compartmentation in the Lacrosse building and the Marina Torch failed, fatality due to facade fire may require the collapse of multiple layers of fire protection.

Indeed, one of the deadliest facade fires in the British Isles prior to the Grenfell Fire was the Summerland Fire in 1973. The incident started with a discarded match that resulted in 50 fatalities and 80 injured. A commission was appointed to investigate the incident, and it was found that multiple failures in building design had led to the massive loss of lives. Unfortunately, some of these defects can still be found in buildings built after the incident [57].

This chapter intends to describe the shortcomings in Summerland’s fire protection layers and draw parallels between some of the failures still found in the building industry.

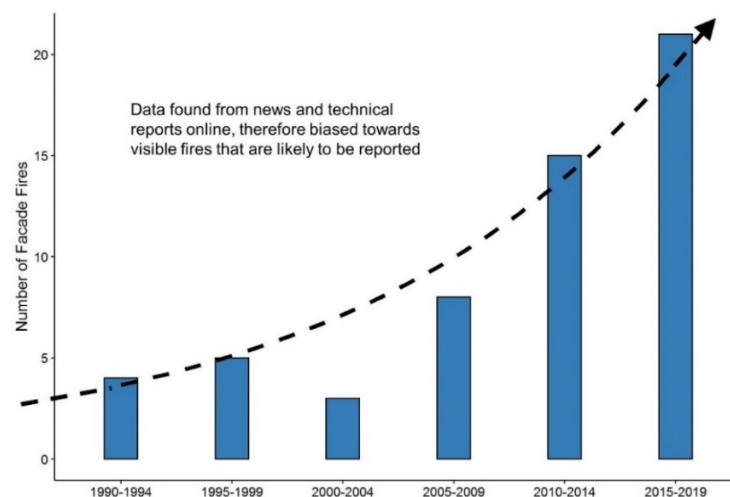


Figure 2.1. Plot of facade fires reported by the media. The numbers represent large fires that warrant reporting and do not represent all facade fires. 1990–2019[4]

Table 2.1 The list of high-rise facade fires from 1990 to 2020. This is a partial list that Bonner compiled by searching through news reports and research literature [53]. The incidents may therefore be more biased toward large fires.

Building	Location	Date
393 Kennedy St	Winnipeg, Canada	10/01/1990
Knowsley Heights	Liverpool, UK	05/04/1991
Mercantile Credit Building	Basingstoke	01/01/1991
Sun Valley Poultry Factory	Hereford, UK	01/09/1994
Motomachi Appartments	Hiroshima, Japan	28/10/1996
Eldorado Hotel	Reno, USA	30/09/1997
Palace Station Hotel and Casino	Las Vegas, USA	20/06/1998
Garnock Court	Irvine, Scotland	11/06/1999
Parque Central Complex	Caracas, Venezuela	17/10/2004
Windsor Tower Fire	Madrid, Spain	12/02/2005
Water Club Tower, Borgata Casino Hotel	Atlantic City, USA	23/09/2007
MGM Monte Carlo Hotel	Las Vegas, USA	25/01/2008
CCTV Tower	Beijing, China	09/02/2009
Lakanal House	London, UK	03/07/2009
Al Kuwait Tower	Sharjah, UAE	06/07/2010
Grozny-City Towers	Chechnya, Russia	03/04/2013
Lacrosse Building	Melbourne, Australia	25/11/2014
Torch Tower	Dubai, UAE	21/02/2015
Ajman One Complex	Ajman, UAE	28/03/2016
Grenfell Tower	London, UK	14/06/2017
Torch Tower	Dubai, UAE	04/08/2017
Zen Tower	Dubai, UAE	15/05/2018
Commercial Building	Luoyang, China	29/05/2019
The Cube Student Housing	Bolton, UK	16/11/2019

2.2 Timeline

The Summerland Leisure Centre was a new and innovative concept in the 1960s when it was first proposed. The concept can be traced to the reduced travel time from the UK to mainland Europe, which reduced the number of UK tourists to the Isle of Man. The Isle of Man, a country that relies heavily on tourism from the UK, was desperate to reattract tourists [58]. To achieve this, the government of Manx commissioned a leisure centre with a single, large and transparent structure that mimics the Mediterranean weather by admitting as much light into the building as possible, a popular tourist destination for the British at that time. The building was designed to hold 5000 people, and it was among the first buildings that contained different recreational activities, including but not limited to swimming pools, amusement areas, bars, and discos [59].

The construction of the Summerland building began in 1968. Throughout the construction process, financial issues contributed to several modifications to the building plan and project delays. The building was finally completed on the 25th of May 1971, when it opened its door to its first customer.

On the 2nd of August 1973, at 7:40 p.m., three Liverpool schoolboys were smoking near a dismantled kiosk. The boys discarded a lit match and caused a section of the kiosk to catch fire. The kiosk and its contents burned intensely within minutes, and flames started impinging onto the building's facade at the location, as shown in Figure 2.2 [60]. After around 20 minutes, an extensive fire was established on both the facade and within the building. At around 8.06 p.m., the first fire appliances arrived to suppress the fire [61]. Unfortunately, by this time, the fire was too well developed, and the fire brigade could only prevent further spread to other parts of the building. The fire was eventually extinguished around 9.00 a.m.

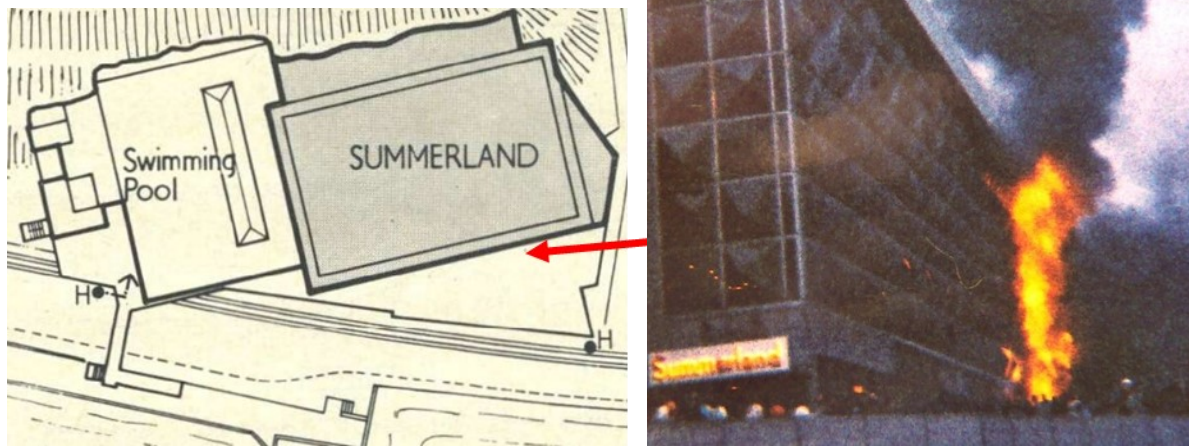


Figure 2.2 The red arrow represents the area where the fire was believed to first start (left) [62]. Extensive fire on the facade of Summerland after around 20 minutes. (right) [63]

2.3 How Did This Happen?

After the incident, the blame for the rapid flame spread was quickly assigned to the poor choice of construction materials. However, as aforementioned, failure of such magnitude is often caused by the collapse of multiple protection layers. In building fire safety, there are six layers of fire protection [64]:

1. Prevention
2. Detection
3. Evacuation
4. Compartmentation
5. Suppression
6. Structural Resistance

Each layer plays a role in preventing or reducing the severity of an incident. For example, Figure 2.3 shows how these layers work together to prevent cataphoric failure during a fire.

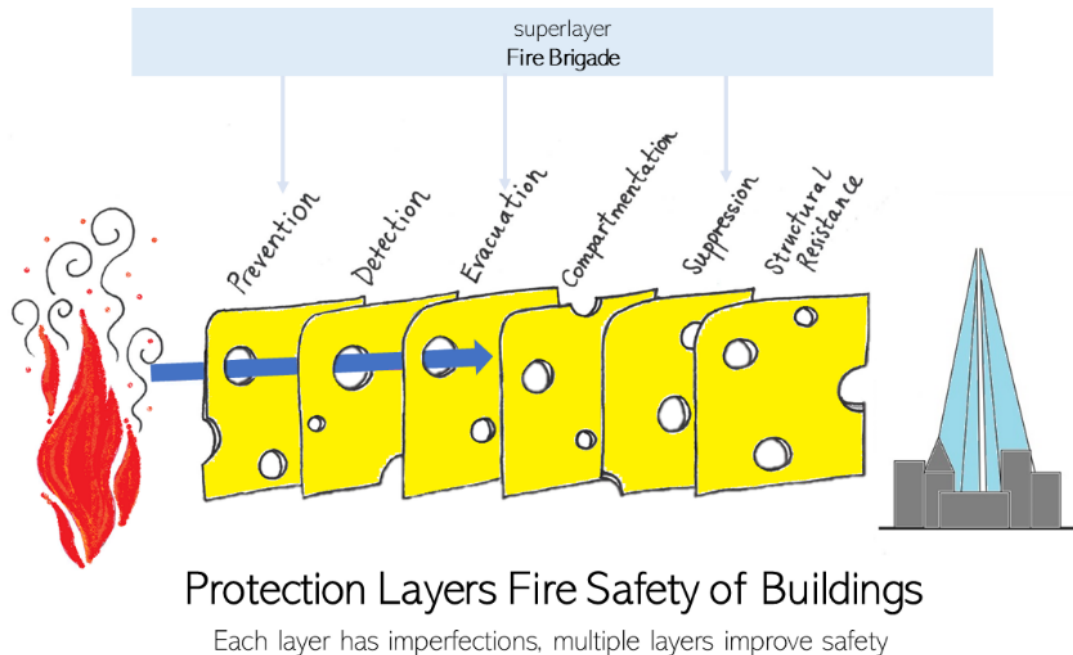


Figure 2.3. A simplified Swiss-cheese model shows how each fire protection layer works. These layers might not all be present in a building, but the presence of multiple layers improves overall fire safety [65].

Of these six layers of protection, all but the structural resistance layer failed in the Summerland building. These failed layers will be explored to understand how they are meant to prevent a fire disaster and how they failed in the Summerland disaster.

2.3.1 Prevention Layer

The prevention layer is responsible for ensuring that no self-sustaining fire can take place in the building. This is often achieved by using non-flammable materials or removing ignition sources in vulnerable areas. In the Summerland building, the prevention layer was compromised due to the presence of a fuel source near an extremely flammable facade.

Months before the fire, a storm damaged a kiosk outside the golf terrace near the building facade. The standard procedure by management was to disassemble the kiosk and store it safely [60]. However, although the kiosk was dismantled, it became a fuel source near the facade because it was not stored away.

Nevertheless, fuel alone was not enough to cause a fire of this magnitude. The use of flammable material as facades allowed the flame to spread quickly. The Summerland facades can be broken down into three different materials:

1. Oroglass (PMMA)
2. Galbestos (corrugated steel sheet coated in a mixture of asbestos and bitumen)
3. Decalin (a sound-absorbent fibreboard)

All three materials are extremely flammable and cover the building extensively, as shown in Figure 2.4 and Figure 2.5.

After the incident, questions were raised about the choice of materials and how they were approved under building regulations. Under the Isle of Man's Local Government (Building Bye-Laws) Act 1950, three Bye-Laws would have restricted the use of these materials, as shown in Table 1 [61].

Table 2.2 Bye-laws of Interest and the Materials Each Would Have Restricted

Bye-laws	Requirement	Affected Materials
Bye-law 39	Requires external walls of any building to be non-combustible and fire resistant for two hours	Oroglass, Galbestos
Bye-law 47	Cavity wall with combustible material shall be fire-stopped.	Galbestos, Decalin
Bye-law 50(1)	The roof should have adequate protection against the spread of fire.	Oroglass

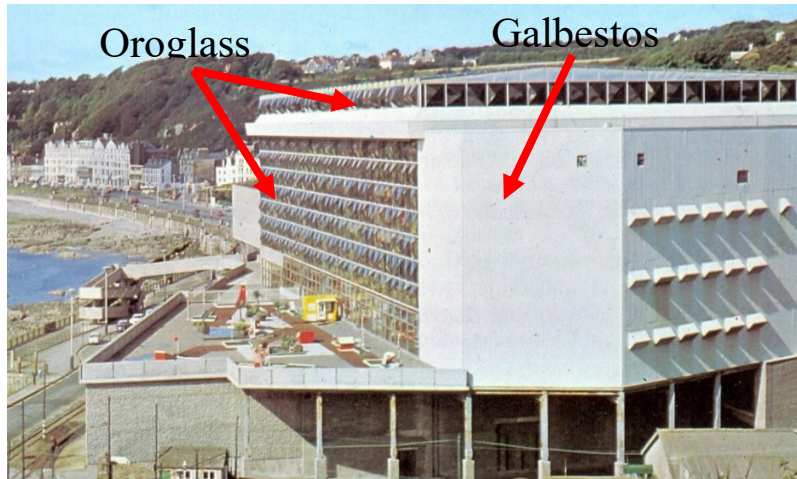


Figure 2.4 Oroglas and Galbestos were used extensively across Summerland's facade [58].

Oroglas

The use of Oroglas, a relatively new material at that time, was granted for use after the relaxation of the regulations. The relaxation was given on the basis that Oroglas was believed to be non-combustible although not fire resistant after passing the BS 467 Part 5 test (since withdrawn).

To pass this test, the material is held vertically and is subjected to a small flame at the centre for 10 seconds. The material passes the test if the sample ceases to burn within 10 seconds after the flame is removed. However, this test is inappropriate as almost all dense combustible material with more than 4 mm (0.04 in) thickness would pass [15]. The lack of understanding of the test result meant that the authority granted the relaxation without knowing the weakness they imposed on the building. Despite later evaluation by the Chief Fire Officer making clear that the Oroglas was combustible, he fell short of objecting to the relaxation as he believed the building had a generous fire evacuation strategy based on its initial building plan [61].

Galbestos

Galbestos was initially not included in the building plan and was introduced later as a substitute for reinforced concrete due to financial reasons [61]. The designer was aware that Galbestos would not comply with the regulation as it is both combustible and not fire

resistant. However, he believed the material would still be adequate to prevent rapid flame spread. The proposal to replace the reinforced concrete with Galbestos was then submitted without making clear that Galbestos required further relaxation of the regulation. The authority thought the application was to reconfirm the waiver for Oroglas and approved the submission without seeking further advice. The approved submission made no mention that the waiver was only for Oroglas, leading to a misunderstanding that both materials were approved.

Lastly, the 0.3 m gap formed between the Galbestos and Decalin allowed the fire to develop with great intensity from within without being visible to the outside, as shown in Figure 2.5 [15]. When the fire finally breached into the building compartment, it was already well-developed and quickly spread to the rest of the building. This gap was technically not considered a cavity under Bye-Law 47. However, from a fire engineering standpoint, it behaves similarly to a cavity and would still need to be fire-stopped as a matter of good practice [61]. The severity of the fire in the cavity was made worse with the use of Decalin. The decision to replace the plasterboard with Decalin was made hastily after the designer was introduced to it [61]. Under time pressure to find a sound-insulating board, the designer found that Decalin fit the requirements and replaced the less-combustible plasterboard without further investigating Decalin's fire properties.

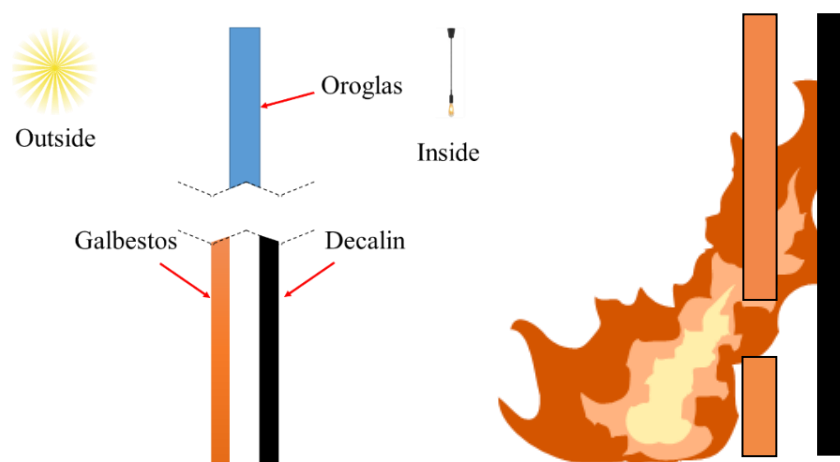


Figure 2.5 Two types of façade on the Summerland building, Oroglas and Galbestos/Decalin (Decalin not always present) (left). Note that the cavity formed between Galbestos and Decalin encouraged fire spread (right) [52]

As a result of all the novel flammable materials introduced into the cavity, the flammability of the overall system is very high and would allow flame to spread within the building quickly.

2.3.2 Detection Layer

Whenever a building's prevention layer fails, it relies on its detection layer to inform its occupants and emergency services of a fire. This is typically achieved by installing detection systems such as building fire alarms.

At Summerland, the fire was discovered almost immediately, but the detection layer was breached as the detection measures failed to inform the occupants and fire service of the fire until the fire was too well-developed. The fire service was informed of the fire by a passerby instead of Summerland staff or its automated system. This resulted in the fire service arriving at the scene about 21 mins after the fire was discovered [61].

To understand how the detection layer in Summerland failed, it is essential first to understand the detection systems available in the building. In essence, the detection system in Summerland was split into two systems: one accessible by the public and another accessible only by staff members. Both systems will immediately inform the fire brigade of the fire when activated. However, the difference between the systems was that siren would sound immediately if the staff's alarm were triggered, whereas the public alarm would not cause sirens to sound. During the incident, at least two public fire alarms were found to be activated.

Investigation into the matter found that building management tampered with the public alarm mechanism to delay the call to the fire brigade to allow more time for staff to investigate false alarms. The Chief Fire Officer was not informed of this change and told the public inquiry that he would have disapproved of the changes had he been informed of it [61]. Summerland staff members were also not trained to react to an emergency. This resulted in staff not triggering the alarms and announcing the fire to the public via a public speaker.

2.3.3 Evacuation Layer

The purpose of the evacuation layer is to enable the safe abandonment of the building by all users when a fire is detected. The failure of this layer in Summerland can be attributed to two factors: 1) the ill-defined responsibilities within management and 2) the poorly thought-out building layout.

The evacuation process is a complex procedure that cannot be improvised during an emergency. A well-executed evacuation procedure requires coordination between staff that is worked out well in advance and requires fire drills to be conducted periodically. Summerland management had a guidance document for all future general managers that showed all evacuation exits, outlined staff responsibilities, evacuation drill routines, and other best practices during an emergency. The inquiry committee believed this document would have helped prepare Summerland employees for the fire [61].

Unfortunately, as different general managers assumed the job, the lack of handover caused newer general managers not to be aware of this document. This resulted in management assuming that the responsibility to organise fire drills fell on other staff members, and no emergency procedures were in place. Consequently, during the emergency, staff were unaware of their responsibility to guide occupants out of the building nor unlock emergency exits, as shown in Figure 2.6. Some staff also committed a mistake by cutting off the electrical supply, believing it was the correct procedure to ensure public safety. This reduced visibility within the building due to the blackout, and it worsened the evacuation process.

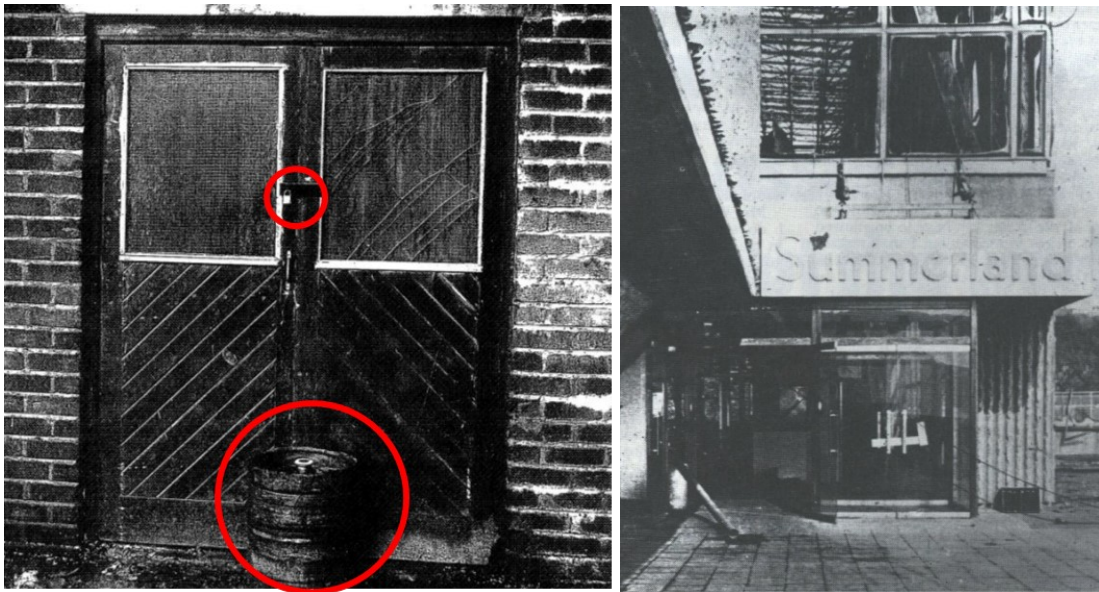


Figure 2.6 Photos taken after the fire show some exits are still locked and obstructed. (Source: Police Photographs, Isle of Man Public Record Office)

In addition, the building plan was poorly designed to allow an orderly evacuation. Throughout the construction stages, several changes to the design plan were made. These include removing and reducing the width of stairways. No advice was sought from the Chief Fire Officer on these changes. When the building was completed, the Chief Fire Officer's inspection revealed that many of these changes had created bottlenecks that would hinder evacuation. He required a few changes to improve this, but some areas were still inadequate to allow safe evacuation.

Furthermore, the building lacked exit and directional signs, which caused sheep syndrome among the occupants. Sheep syndrome is a condition where people instinctively choose to leave from the same entrance they entered. Therefore, buildings must have enough signs to direct the occupants out of the building from all possible exits. It was found that many exits in Summerland were not marked as emergency exits apart, which slowed down the evacuation process.

The Summerland building layout was also such that parents tended to be separated from their children [62]. This was due to the layout of the building, which had entertainment for children and adults located at different levels. As a result, some parents went against the

evacuation flow during the emergency to look for their children on different floors, slowing down the evacuation process.

2.3.4 Compartmentation Layer

The compartmentation layer of a building ensures that fire does not spread quickly throughout the building. This allows more time for emergency service and occupants to react to the fire. The nature of the Summerland building to have a single, large compartment meant that it could not be compartmentalised completely, as seen in Figure 2.7. However, the designers could have reduced flame spread from one level to another by installing fire-resistant guard rails and fire-stops, as identified in the inquiry. The lack of fire-stops between each level and the external wall meant that fire could spread upward quickly via the chimney effect [58]. Furthermore, as the fire spread to the roof via the facade cavity, Oroglas at the ceiling melted to vent the fire below and spread fire across the building via burning droplets.

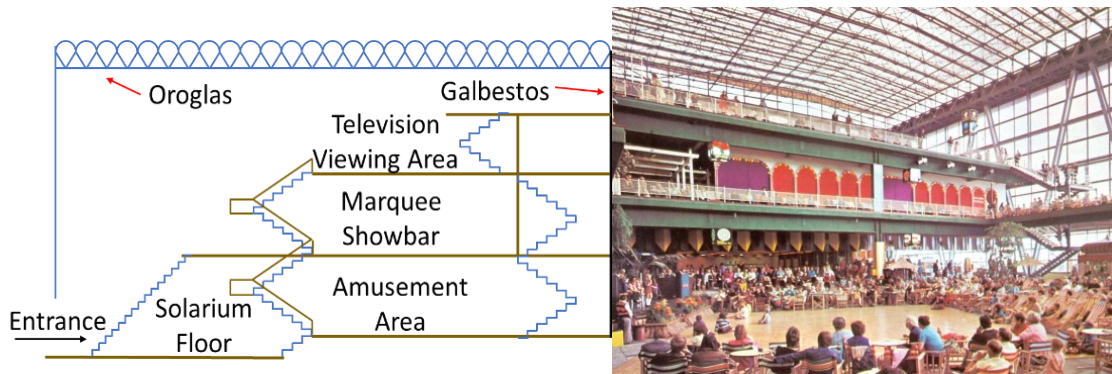


Figure 2.7 Summerland was designed to have a single, large space with limited compartmentation [58].

Lastly, stairways are normally compartmentalised to ensure the safe evacuation of the building users. When the Summerland building was first designed, some stairways were compartmentalised to facilitate an emergency evacuation. Unfortunately, when the reinforced concrete was replaced with Galbestos, the northeast service stair, as shown in Figure 2.8, was surrounded by combustible walls. A further breach of this compartmentalised stairway was made by an unauthorised doorway to allow easier

movement of goods into and out of a bar. The unauthorised doorway was responsible for a huge amount of smoke entering the stairway, which may have resulted in 12 people dead just 3 meters from the exit [61].

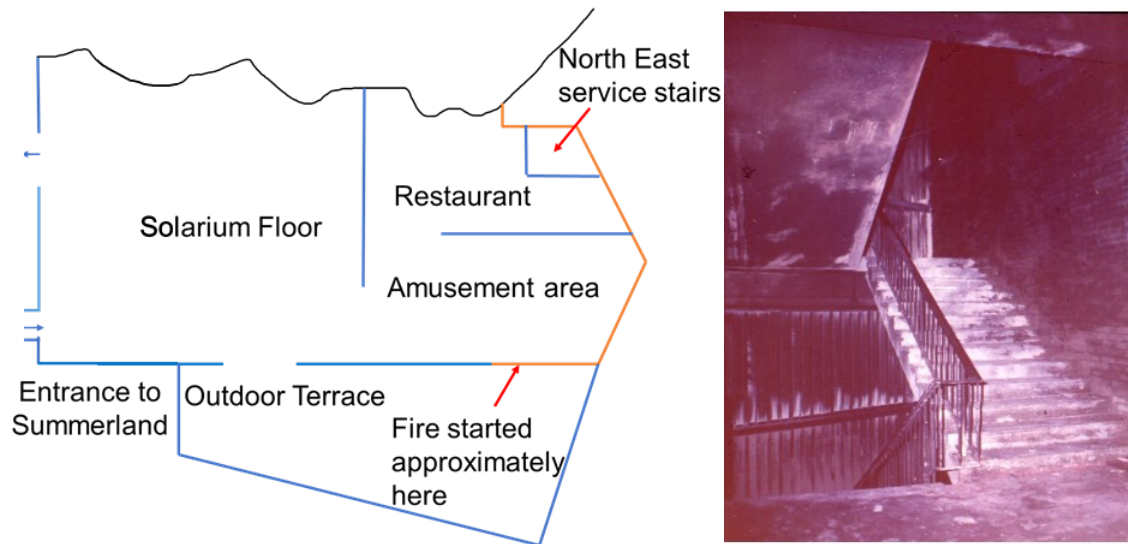


Figure 2.8 The northeast service stairs, one of the supposedly compartmentalised stairways, was surrounded by Galbestos (orange line), which is flammable (Source: Report of the Summerland Fire Commission)

2.3.5 Suppression Layer

The suppression layer acts to suppress or slow down the spread of fire to buy more time for building users to evacuate the building. Fire suppression can be achieved either automatically by using sprinklers or manually by using fire extinguishers by trained staff. After Summerland construction was completed, its insurance company offered a large reduction in premium if sprinklers were installed in the building. While installing sprinklers might not have suppressed the fire completely, the sprinklers could have helped offset the limited compartmentation and allowed more time for evacuation [66]. Unfortunately, the management deemed the sprinklers unnecessary and was not installed. Additionally, the lack of staff training meant that available firefighting equipment was not used correctly. This, together with the lack of sprinklers in the building, caused the suppression layer in Summerland to fail.

2.4 Has The Lesson Been Learned?

Ten years after the Summerland Incident, Dennis Harper, part of the three-man commission that investigated the incident, noted that many lessons from Summerland were not learned [57]. Indeed, after the 2017 Grenfell incident, an independent review into building regulations and fire safety chaired by Dame Judith Hackett found the building industry was “an industry that has not reflected and learned from itself, nor looked to other sectors.” [9].

The reason the Summerland fire spread so quickly was due to the failure of both the prevention and compartmentalisation layers. The failure of both layers can be attributed to the lack of understanding of the fire properties of innovative materials, failure to follow good practices when constructing the building, and failure to consider the effect of modifying building components on the system’s overall flammability. A similar failure was seen in the 2017 Grenfell incident, where the cavity barrier was found to be poorly fitted, and the building refurbishment allowed a kitchen fire to develop into a disastrous fire [67].

2.5 Conclusion

The 1973 Summerland disaster was due to the collective failure of five of the six fire protection layers: prevention, detection, evacuation, compartmentation, and suppression; only the structural protection layer remained intact. As a result, the tragedy took 50 lives and seriously injured 80.

While the high death toll was not solely due to human error, such as unauthorised alteration of the fire alarm and inadequate staff management, the lack of awareness by the senior management of their responsibility to provide training to staff to deal with fire emergencies contributed to the death toll. In addition, the management’s poor building layout and the lack of emergency exit signs also delayed the evacuation process due to bottlenecks at key areas of the evacuation path.

However, a large portion of the blame can be assigned to using flammable materials as the facade and having a fuel source near the facade. This resulted in a severe breach of the prevention layer, causing rapid fire spread on the building’s facades. The choice to use these

materials was driven by the need to achieve building facade objectives. However, the failure to understand the fire properties of these new materials and the poor communications between authorities and designers compromised the fire safety of the building. The prevention layer breach could have potentially been avoided if the procedures to remove any fuel source from flammable sections of the building had been followed, and the consequence of the regulation waiver on new materials had been fully understood. Unfortunately, the use of combustible material coupled with the cavity width allowed the fire to develop out of sight until it was too well developed. As a result, when the fire breached into Summerland, it became too large to put out quickly, allowing rapid fire spread throughout the building.

Forty-seven years later, the Summerland fire still echoes, with many similar failures to be found in modern building fires, especially flammable facades and cavities, which are poorly fire-stopped. The lessons from the Summerland fire should and must be learned, for if they are not, a similar disaster will repeat itself.

Chapter 3

Step-by-Step Development of Thermofluids Simulation inside a Narrow Cavity

Summary²

CFD fire modelling is an excellent tool to complement experimental studies on fire in a narrow cavity. However, the current CFD fire models are validated for building compartment fires and not narrow cavity fires. To ensure robust CFD modelling of a facade cavity fire, all physical phenomena involved in a facade cavity fire need to be validated. This chapter validates step-by-step the physical phenomena of fluid mechanics, heat transfer and buoyancy that create a non-linear and complex behaviour inside a narrow cavity on FireFOAM. The numerical methodology developed is split into three different scenarios of increasing complexity and is compared individually against experimental data from the literature. The results show that the model can accurately predict fluid flow and convective heat transfer with an average error of around 20%. Furthermore, the model could predict the effect of buoyancy and heat flux over different cavity widths, with an average error of between 14% - 50%. The limitations of the current model were also discussed. Finally, results show that the model can include more submodels to predict the cavity fire with a significant degree of credibility.

² This chapter is based on a submitted paper: B. Khoo, W. Jahn, M. Bonner, P. Kotsovinos, G. Rein, Step-by-Step Development of Multiphysics Simulation in a Narrow Cavity fire.

3.1 Introduction

In the previous chapters, I have stated that cavity fires can be hazardous as they allow the breach of building compartmentation and could allow the fire to be hidden away from sight. Additionally, facade cavity fire is a multiphysics problem that involves five different physical phenomena: 1) Fluid Flow, 2) Heat Transfer, 3) Buoyancy, 4) Combustion, and 5) Pyrolysis. These physical phenomena are strongly coupled, and inaccurate predictions of any physical phenomenon may impact the overall results due to compensation effects. Therefore, a numerical methodology that validates one physical phenomenon at a time is necessary to reduce compensation effects. To the best of my knowledge, current facade cavity simulations are sparse and mostly validated with all physical phenomena at once. It is important to note that the initial advancement of fire modelling, mainly in open fire and compartment fires, was validated with one physical phenomenon at a time. However, the assumption that these models are valid for narrow cavity fire is yet to be tested.

The first CFD fire model appeared in the late 1970s, where it was used to predict flows within a rectangular enclosure representing a building compartment [68]. Further developments in CFD fire modelling occurred in the late 1980s and early 1990s to study and understand the King's Cross fire in the London Underground station. The simulations during this period were limited in computational power and were inevitably simplified models. For example, the fire was modelled using a heat source term instead of a combustion model, and turbulence was modelled using the RANS approach. Buoyant force, however, was simulated, and its effect was essential in allowing engineers to understand how air and smoke flow was altered within a compartment. These models were crucial in discovering the trench effect in the King's Cross fire and allowed engineers to study smoke movement within a building.

As facade cavity fire becomes more frequent due to the use of innovative materials and facade designs, understanding the fire dynamics of a cavity fire becomes essential for practitioners to design a fire-safe facade. However, the high cost of facade fire experiments and the large number of experiments required can be prohibitively expensive. This makes CFD simulations an attractive tool for researchers to study the fire dynamics in a facade cavity. Unfortunately, numerical methodologies developed for narrow cavity fire scenarios

remains limited [48, 49], and most methodologies assume that fire models validated for compartment fire or open-air fire can be extended to narrow cavity fire scenario.

This chapter validates the first three physical phenomena involved in a narrow cavity. I will show that FireFoam, an open-source CFD code is capable of predicting the fluid flow, convective heat transfer and buoyant flow in a narrow facade cavity. Then, I will discuss some limitations of the FireFoam code in predicting each of these physical phenomena in a narrow cavity. The validation of the remaining physical phenomena will be discussed in Chapter 4 and Chapter 6.

3.2 Methodology

As aforementioned, facade cavity fire is a multiphysics process strongly coupled to five physical phenomena, i.e. fluid flow, heat transfer, buoyancy, combustion, and pyrolysis. Each of these physical phenomena could significantly impact the simulation's overall results. This section explains the importance of accurately predicting each physical phenomenon and the methodology developed to achieve this.

The fluid flow physical phenomenon in a narrow cavity needs to be accurately predicted because the boundary layer represents a significant portion of the fluid flow profile in a narrow cavity. Accurate prediction of the boundary layer is essential as they affect the heat transfer to walls. In addition, accurate prediction of fluid flow is essential for predicting turbulent viscosity near walls which also affects the calculation of the rate of combustion near walls [45, 69].

Secondly, the model also needs to accurately predict the heat transfer within a narrow cavity to study the fire dynamics reliably. Inaccurate heat flux predictions could underestimate the severity of the condition in a facade system. For example, if the heat flux needed for the piloted ignition is underpredicted [70], the model cannot predict the flame spread on the material, therefore, cannot predict the fire dynamic in the narrow cavity.

Similarly, buoyancy prediction is essential in predicting the fire dynamic in a cavity. Buoyancy allows hot gas to rise and plays a critical role in facade fire, where the chimney effect, a movement of air in a cavity due to buoyancy, allows for rapid fire spread in a cavity

fire [71]. It was found by Markatos et al. [72] that in a buoyancy-driven flow, a satisfactory prediction of buoyancy is essential in predicting fluid flow.

Additionally, an accurate combustion model is essential for predicting a facade fire. This is important as the rate of combustion affects the temperature and radiative heat transfer to the facade panel or insulation. As a result, the robustness of the combustion model used for a narrow cavity fire scenario directly affects the heat transfer prediction and, therefore, impacts fire dynamics in a facade cavity [73].

Lastly, an accurate prediction of pyrolysis, an endothermic process due to a solid's degradation, is also essential. The process releases pyrolyzate, a combustible gas which combusts to release more heat energy onto the degrading solid. Therefore, from a modelling perspective, an erroneous prediction of the pyrolysis rate will result in an inaccurate heat release rate (HRR) in the cavity, jeopardising the accuracy of the simulation.

As discussed above, accurately predicting all five physical phenomena is essential in predicting the fire dynamics within a narrow cavity. However, as all five physical phenomena are strongly coupled, it is difficult to validate all models at once, as any tweak to one parameter will affect the predictions of multiple physical phenomena. An approach of splitting facade cavity fire into five different scenarios with increasing complexity, as shown in Figure 3.1, was taken to reduce this effect. The rationale behind this approach is to limit the degree of freedom and hence the compensation effect model when modelling a cavity fire. With each scenario validated, the model parameters used in each scenario are fixed and are carried forward to the following scenario to limit the model's degree of freedom. It is important to note that various researchers have extensively studied the first three scenarios, Scenario 1, Scenario 2 and Scenario 3, where fluid flow, heat transfer and buoyancy physical phenomena are involved [74, 75, 84, 85, 76–83]. The approach to validate these scenarios is not to further the understanding of these phenomena but to establish model parameters that will be then used to simulate more complex narrow cavity fire scenarios.

One of the main challenges of validating a CFD model is defining the criteria by which the model is considered validated. Validation of a model cannot be mathematically proven and has to be assessed for individual scenarios, i.e. validation of one scenario does not imply

the codes are validated for all scenarios. Many researchers have tried to establish the activity required for CFD validation and what the validation process activity implies. One of the reasons for the difficulty in establishing a general validation criterion is that the model's ability to predict the experimental results becomes weaker as the complexity of the problem increases. Establishing a general validation criterion is difficult and remains an active research topic, especially for models involving multiple physical phenomena [86]. The current work does not attempt to solve and define the metrics required for validating the cavity fire scenario. Instead, the validation process will compare the global features to first-order statistical moments and, if experimental data is available, the second-order statistical moments. These comparisons are made by evaluating the mean relative error and bounded relative error between the experimental data and simulation prediction [87], as shown in (1) and (2)

$$RE^m = \frac{1}{N} \sum_{i=1}^{i=N} \left(\frac{M_i - E_i}{E_i} \right) \times 100 \quad (1)$$

$$RE^b = \sum_{i=1}^{i=N} \tanh \left(\frac{M_i - E_i}{E_i} \right) \times 100 \quad (2)$$

Where RE^m is the mean relative error, RE^b is the bounded relative error, M is the predicted value, and E is the experimental value. Uncertainty of the error is also calculated for experiments that provide information on experimental uncertainty.

RE^b was also used to avoid the large relative error when the measured value is close to zero.

In this chapter, only Scenarios 1 to 3 are presented, as the integration of combustion and pyrolysis chemistry into the CFD model corresponds to a major leap in complexity. Scenario 4, and 5, which validate combustion and pyrolysis chemistry, are presented in Chapter 4 and Chapter 5. The experimental data used to validate these scenarios are found in the literature [28, 74, 76, 88]. While the validation cases are not in the range of actual fire conditions, the validation of these scenarios represents the first step in developing a robust

model that can be used to study various cavity fire scenarios. Mechanical failures could also be present in a facade fire but were not modelled, as the simulation of mechanical failures is not within the scope of this thesis.

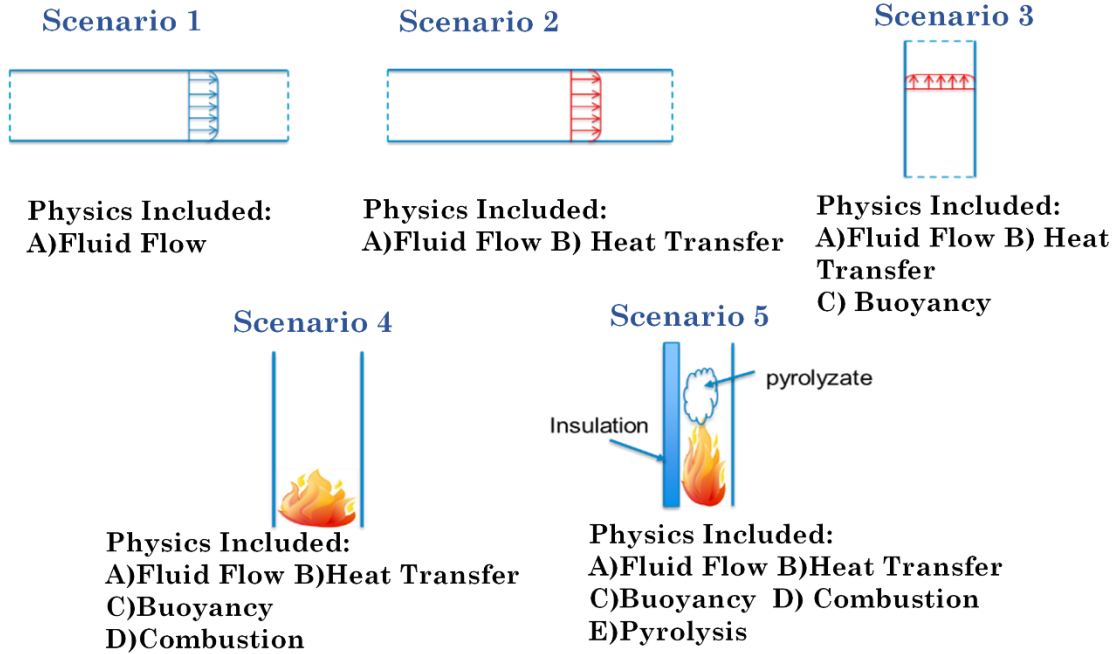


Figure 3.1 The different physical phenomena involved in a cavity fire validated in 5 scenarios. Each physical phenomenon interacts with the other in the facade cavity to create a non-linear fire behaviour.

3.3 Experimental Setup

The experimental setup of each scenario will only be discussed in brief, and the reader is referred to the original research for a more detailed setup of Scenario 1 [76], Scenario 2 [74], and Scenario 3 [88]. A simplified schematic of the experiment is shown in Figure 3.2.

For Scenario 1, the experiment consists of a narrow horizontal channel that is 14.630 m long, 1.143 m wide and has a cavity width of 0.0635 m. The channel is enclosed such that no inflow or outflow is induced spanwise. The airflow through the channel has a bulk velocity, defined as the volume flow rate over a cross-section area, of 5.77 m s^{-1} and a Reynolds number, $Re = 13,800$, and the velocity profile of the developed flow was measured using an anemometer.

Scenario 2's setup is similar to that of Scenario 1, except its length, width and cavity width are 3.962 m, 0.3048 m, and 0.0178 m, respectively. The air is blown through the cavity at a bulk velocity of 4.66 m s^{-1} and $\text{Re} = 9370$. The ambient air temperature is 37°C , and the bottom and the upper plate temperature are 30°C and 46°C , respectively. Anemometers and thermometers are used to measure the velocity and temperature profile of the developed flow.

In Scenario 3, a parallel channel of 4.98 m in height and 1.03 m in width was constructed with a single vertical plate with uniform heat generation placed between two polycarbonate plates. The experimental result showed that the temperature gradient near the polycarbonate plates is minimal; therefore, the panel is assumed to be adiabatic. Similarly, the channels are enclosed to prevent spanwise airflow. The distance between the heated plate and adiabatic plates is identical and separated by distance W , where $W = 50 \text{ mm}$, 100 mm , and 200 mm . The generated wall heat flux investigated in the paper was 104 W m^{-2} and 208 W m^{-2} . For measurements, velocities are measured along the cavity at the height of 0.82 m , 2.665 m and 3.865 m using laser doppler velocimetry (LDV) and temperatures are measured using a thermocouple along the heated wall.

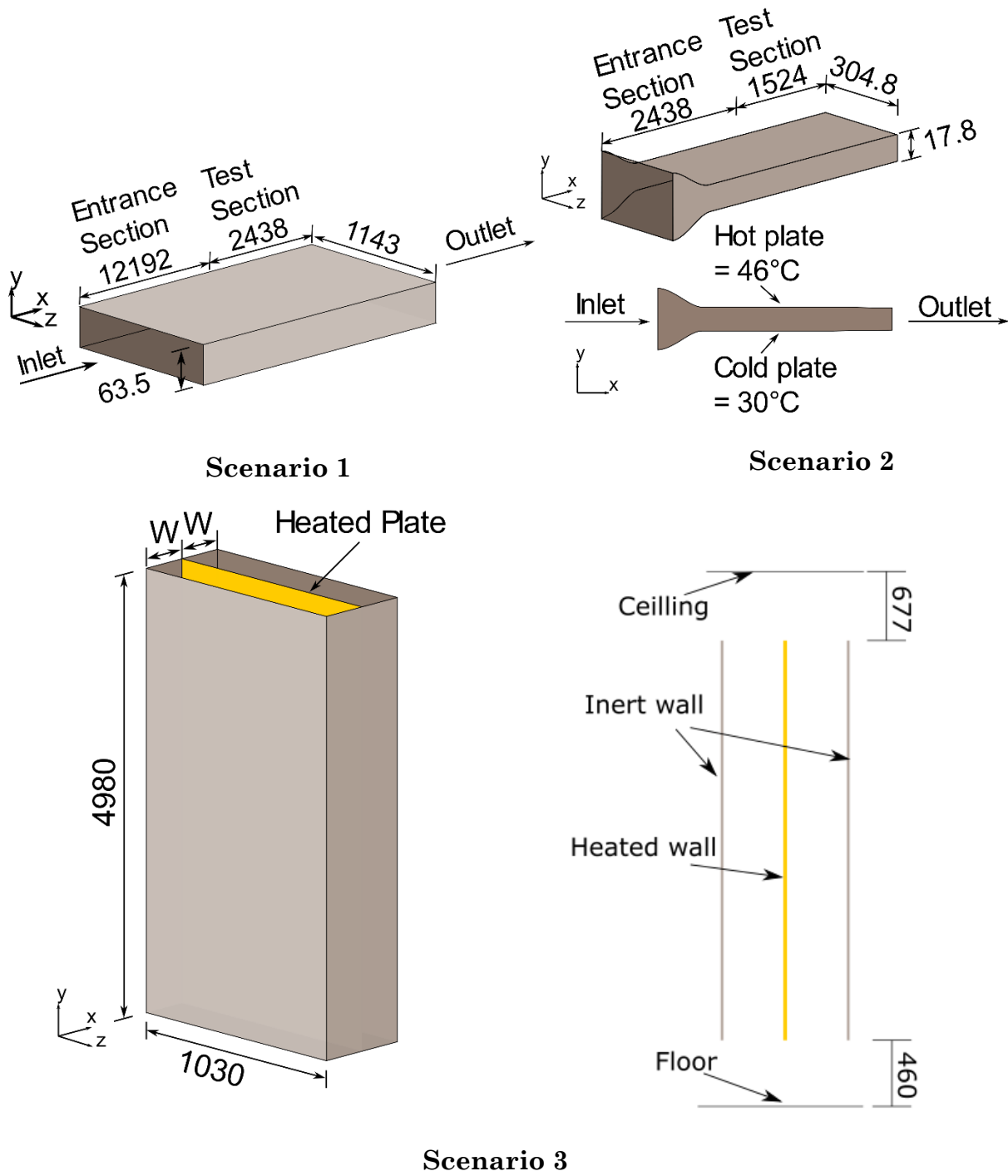


Figure 3.2 Simplified Schematic of Scenario 1 to Scenario 3. Each scenario represents one of the multiple physical phenomena the model intends to validate. The bracketed term is hereby used to refer to each scenario.

Dimensions are in mm

3.4 Numerical Modelling

The numerical methodology developed was performed using FireFoam-dev [89], a solver based on the open-source framework, OpenFOAM. OpenFOAM provides numerical routines for solving partial differential equations by discretising them using the Finite Volume technique on both structured and unstructured meshes [90]. FireFoam is an unsteady solver for buoyancy-driven turbulent reacting flows. It is a LES-based solver that solves the spatially filtered Navier-Stokes equation using a fully compressible flow formulation. The decomposition of the filtered and unresolved part of any flow field $\phi(x, t)$ is:

$$\phi(x, t) = \bar{\phi}(x, t) + \phi''(x, t) \quad (3.3)$$

where ϕ is the unfiltered term, $\bar{\phi}$ is the filtered functions with spatial variation, which are resolved by the LES computation and ϕ'' is the unresolved spatial variation, x is a vector and t is time.

The following mathematical expression is the filtering operation used to filter any given flow field:

$$\bar{\phi}(x, t) = \iiint_{-\infty}^{\infty} \phi(x, t) G(i - i', \Delta) d^3 x' \quad (3.4)$$

where G is the kernel and Δ is the filter's cut-off width with the following expression

$$G(i - i', \Delta) = \begin{cases} \frac{1}{\Delta^3}, & |i - i'| \leq \frac{\Delta}{2} \\ 0, & \text{otherwise} \end{cases}$$

$$\Delta = \sqrt[3]{\Delta i \Delta j \Delta k}$$

where $\Delta i, \Delta j, \Delta k$ are the cell sizes along the corresponding axis.

To avoid generating additional terms for continuity equations, the Favre filtering such that $\overline{\rho\phi} \equiv \bar{\rho}\tilde{\phi}$ is introduced to separate the terms [91]. Therefore the mass, momentum, species and energy conservation equation are expressed as follows:

- Conservation of mass

$$\frac{\partial \bar{\rho}}{\partial t} + \frac{\partial}{\partial x_i} (\bar{\rho} \tilde{u}_i) = 0 \quad (3.5)$$

where ρ is the density, u_i is the flow velocity at direction i .

- Conservation of Momentum

$$\frac{\partial \bar{\rho} \tilde{u}_i}{\partial t} + \frac{\partial}{\partial x_j} (\bar{\rho} \tilde{u}_i \tilde{u}_j) = -\frac{\partial \bar{p}}{\partial x_i} - \frac{\partial \bar{\tau}_{ij}}{\partial x_j} - \frac{\partial \tau_{ij}^{SGS}}{\partial x_j} + \bar{\rho} g_i \quad j = 1, 2, 3 \quad (3.6)$$

where p is the pressure, τ_{ij} is the viscous stress tensor, τ_{ij}^{SGS} is the subgrid-scale (SGS) stress and g is the gravitational acceleration.

- Conservation of Species:

$$\frac{\partial}{\partial t} (\bar{\rho} \tilde{Y}_k) + \frac{\partial}{\partial x_i} (\bar{\rho} \tilde{Y}_k \tilde{u}_i) = \frac{\partial}{\partial x_i} [\bar{\rho} (\widetilde{u_i Y_k} - \tilde{u}_i \tilde{Y}_k)] + \bar{\omega}_k, \quad k = 1, \dots, n \quad (3.7)$$

where $\bar{\omega}_k$, is the reaction source term of gaseous species k that is simulated.

- Conservation of Energy:

$$\frac{\partial (\bar{\rho} \tilde{h})}{\partial t} + \frac{\partial}{\partial x_i} (\bar{\rho} \tilde{h} \tilde{u}_i) = \frac{\partial}{\partial x_i} [\bar{\rho} (\widetilde{h u_i} - \tilde{h} \tilde{u}_i)] + \frac{\partial p}{\partial t} + \frac{\partial}{\partial x_i} (\bar{J}_i^h + \overline{u_i \tau_{ij}}) + \bar{S}_h \quad (3.8)$$

where h is the total enthalpy, and J_i^h is the diffusion flux vector and S_h is the energy source term.

In this thesis, gas is assumed to be ideal, and the density, temperature and pressure are defined by the following equation.

$$\rho = \frac{p}{RT} \quad (3.9)$$

Where R is the specific gas constant.

The FireFOAM code assumes unity Lewis number for all species so that the thermal diffusivity is always equal to the mass diffusivity. The algorithm used by the code for pressure-velocity coupling is PIMPLE, a combination of PISO and SIMPLE, using three inner and outer corrections.

This work used a maximum Courant number of 0.8 to solve the time term to ensure numerical stability, following a second-order backward scheme. The convective terms are discretised using the LUST scheme, a scheme with a blending factor of 0.75 central differenced and 0.25 linear upwind scheme. The diffusive terms are discretised using the central differencing scheme with an explicit non-orthogonal correction. As for species mass transport, the terms are discretised using a second-order Total Variation Diminishing (TVD) scheme with Sweby limiter to ensure a bounded solution.

FireFOAM provides several subgrid-scale (SGS) turbulence, combustion, and thermal radiation modelling options. In the section below, the models used in these scenarios are explained.

3.4.1 Turbulence

There are several turbulence LES models available in FireFoam, such as the Smagorinsky model, the k -equation eddy viscosity model (k -equation model), and the wall adapting local eddy-viscosity (WALE) model.

In the present study, the SGS turbulence was modelled mainly with wall adapting local eddy-viscosity (WALE) model, as it predicts the SGS kinetic energy, k_{sgs} , and SGS eddy viscosity, ν_{sgs} , better in the near-wall region compared to the default k -equation model used in FireFOAM [45, 92]. The WALE model computes the SGS eddy viscosity, ν_{sgs} as follows:

$$\nu_{sgs} = (C_w \Delta^2) \frac{(S_{ij}^d S_{ij}^d)^{\frac{3}{2}}}{(\tilde{S}_{ij} \tilde{S}_{ij})^{\frac{5}{2}} + (S_{ij}^d S_{ij}^d)^{\frac{5}{4}}} \quad (3.10)$$

where C_w is the model constant with a coefficient of $C_w=0.55$ based on [93]. Δ is the LES filter size, S_{ij}^d is the special tensor defined by Nicoud [92], and \tilde{S}_{ij} is the resolved scale strain rate tensor. The SGS turbulent kinetic energy, k_{sgs} and the rate of dissipation of SGS turbulent kinetic energy in WALE is expressed as:

$$k_{sgs} = \left(\frac{\nu_{sgs}}{C_k \Delta} \right)^2 \quad (3.11)$$

$$\varepsilon_{sgs} = C_E \frac{k_{sgs}^{\frac{3}{2}}}{\Delta} \quad (3.12)$$

Where C_k and C_E are the model constants, where values are based on [93] ($C_k=0.29$ and $C_E=1.048$). These model constants were chosen based on work done by Ren et al., where single wall fire simulations were performed [93].

However, to ensure the implemented WALE model is suitable for cavity flow, both Smagorinsky and k-equation eddy viscosity models are used in Scenario 1 and Scenario 2 to compare the differences between the models.

In the Smagorinsky model, ν_{sgs} is modelled as follows:

$$\nu_{sgs} = (C_s \Delta)^2 |\tilde{S}| \quad (3.13)$$

where C_s is the model constant in the range of 0.1 to 0.25 [94]. In the present study, the coefficient $C_s=0.1$ used was based on the default model constant for fire scenarios [95]. $|\tilde{S}| = \sqrt{\tilde{S}_{ij}\tilde{S}_{ij}}$ is the strain rate tensor. To obtain k_{sgs} , the Smagorinsky model solves the balance equation shown in (3.14), with the value of ε_{sgs} obtained through (3.11)

$$\tilde{S}:B + \frac{C_E k_{sgs}^{\frac{3}{2}}}{\Delta} = 0 \quad (3.14)$$

where “:” is the double inner product operator, $B = \frac{2}{3}k_{sgs}I - 2C_k\sqrt{k_{sgs}}\Delta\tilde{S}_D$ is the SGS stress tensor with \tilde{S}_D being the deviatoric component of the strain rate tensor. The model constants C_k and C_E have a coefficient of 0.05 and 1.048, respectively.

For the k-equation model, the ν_{sgs} is calculated as:

$$\nu_{sgs} = C_k \Delta \sqrt{k_{sgs}} \quad (3.15)$$

where C_k is 0.05 To obtain the k_{sgs} , a transport equation is solved as shown:

$$\begin{aligned} \frac{\partial(\bar{\rho}k_{sgs})}{\partial t} + \frac{\partial(\bar{\rho}\tilde{u}_i k_{sgs})}{\partial x_i} - \frac{\partial}{\partial x_i} \left(\bar{\rho}(\nu + \nu_{sgs}) \frac{\partial k_{sgs}}{\partial x_i} \right) \\ = -\frac{2}{3} \left(\bar{\rho}k_{sgs} + \bar{\rho}\nu_{sgs} \frac{\partial \tilde{u}_k}{\partial x_k} \right) \frac{\partial \tilde{u}_i}{\partial x_i} + 2\bar{\rho}\nu_{sgs} \frac{\partial \tilde{u}_i}{\partial x_j} \frac{\partial \tilde{u}_j}{\partial x_i} - \bar{\rho}\varepsilon_{sgs} \end{aligned} \quad (3.16)$$

The closure expression for ε_{sgs} uses the same expression in (5) with $C_E=1.048$, chosen based on the default model constant [96].

As mentioned previously, both Smagorinsky and k-equation eddy viscosity models have been shown to overpredict near-wall ν_{sgs} and k_{sgs} . To mitigate this issue, the Van Driest wall damping function, as shown in (11), was used to suppress ν_{sgs} near the wall by altering the LES filter size.

$$D = 1 - e^{-\frac{y^+}{A^+}} \quad (3.17)$$

$$\Delta = \min\left(\frac{\kappa y}{C_\delta} D, \Delta_g\right) \quad (3.18)$$

$$y^+ = \frac{u^* \Delta}{\nu} \quad (3.19)$$

where y^+ is the dimensionless wall distance calculated in each time step using (3.19), $A^+ = 26$ and $C_\delta = 0.158$ is the damping function constant, $\kappa = 0.41$ is the von Karman constant, and Δ_g is the cubic root of the volume, u^* is the friction velocity, ν is the kinematic viscosity and Δ is the grid size at the normal to the wall.

3.4.2 Wall Heat Transfer

Coarse grid modelling for convective heat transfer has been developed in FireFoam for industrial-scale study [45, 97]. However, the model has a drawback where it has a specific grid size requirement and straying away from this value requires recalibration of multiple model parameters. Therefore, in the current work, a wall-resolved simulation is performed

where no wall model is used to estimate the convective wall heat transfer. The convective heat transfer is calculated as shown below.

$$q_c'' = k_f \frac{dT_f}{dx} \quad (3.20)$$

Where q_c'' is the convective heat flux, k_f is the fluid thermal conductivity and, $\frac{dT_f}{dx}$ is the thermal gradient of fluid and the wall surface temperature in the first cell next to the wall.

3.5 Computational Domain and Boundary Conditions

For all Scenarios, the meshes are hexahedra structured mesh generated using the OpenFOAM default utility. All cells are generated as cubic cells except those near the wall where cell direction is normal to the wall, Δy , is halved. In Scenario 1, the numerical domain was $200 \times 100 \times 63.5 \text{ mm}^3$. The boundary condition of the simulation for both streamwise and spanwise was set as periodic boundaries. Note that while periodic boundaries are not suitable when a fire is introduced, the purpose of using periodic boundaries in this study is to validate the model capabilities in modelling fluid flow without increasing the required computational resources unnecessarily. For both the top and bottom of the domain, a no-slip boundary was applied. Lastly, the velocity in the domain is perturbed to generate the initial turbulent field, and the bulk velocity in the domain was set to 5.77 m/s. The perturbation of the turbulent field is performed using the boxTurb tool available in OpenFOAM, where divergence-free turbulence conforming to a given turbulence energy spectrum is created.

For Scenario 1, the grid sensitivity was performed using three different grid sizes $\Delta y = 0.78 \text{ mm}$ (Coarse), 0.62 mm (Medium), and 0.50 mm (Fine) with a total cell of 531,441, 1,061,208 and 2,097,152 respectively. The analysis found that the difference between all grid sizes is almost negligible for the predicted mean velocity and velocity fluctuation, as shown in Figure 3.3. However, the log law velocity profile prediction shows an average error of 21.2% for Coarse mesh and 15.1% for Medium mesh and 11.7% for Fine mesh when compared to experimental results. As the improvement in accuracy reduces by almost 50% from Medium to Fine, the Medium mesh was chosen to investigate different turbulence models.

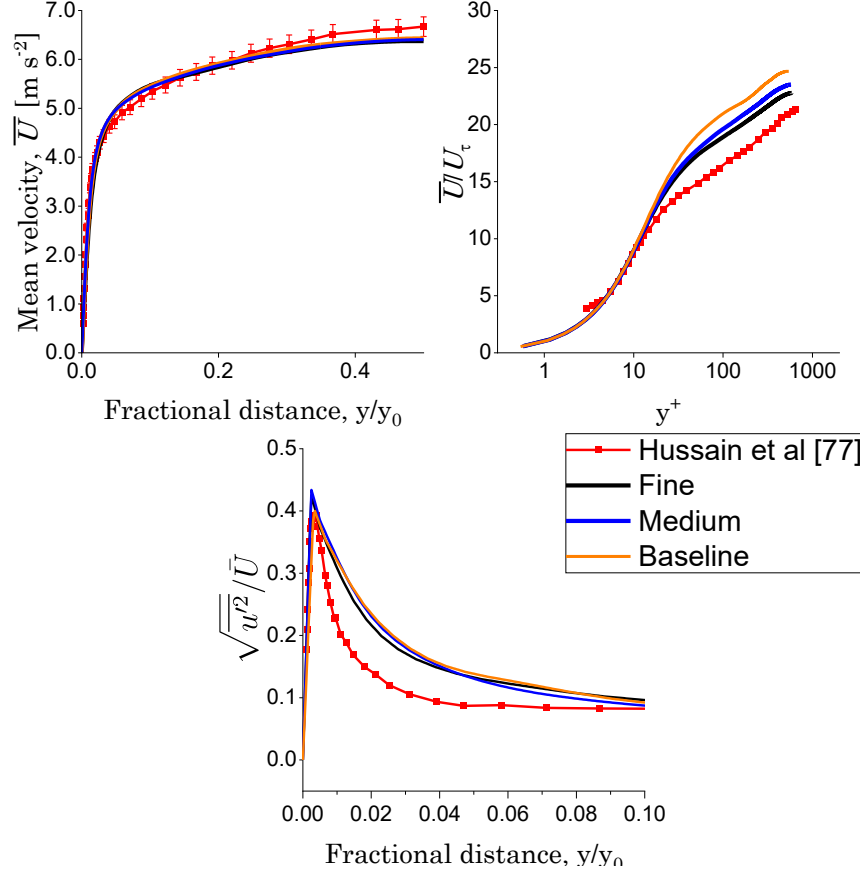


Figure 3.3 Grid sensitivity analysis for Scenario 1. The comparison shows the minimal difference between mesh sizes for predicted mean velocity and turbulent velocity fluctuation. A slightly more significant difference is observed for the log law profile between the mesh sizes.

For Scenario 2, a similar numerical domain for Scenario 1 was used with the cavity width changed to replicate the experiment's cavity width. The top and bottom walls were set with a fixed temperature of 46°C and 30°C, respectively. As for the bulk velocity, it was set to 4.66 m/s. Grid sensitivity was analysed using the same grid sizes as Scenario 1. The setup was found to be grid insensitive for the mean velocity and temperature, as shown in Figure 3.4. The log law profile was not compared as it was not measured in the experiment. As the results from Scenario 1 show that a Medium mesh is required to capture the log-law profile, the Medium mesh was also chosen for this scenario.

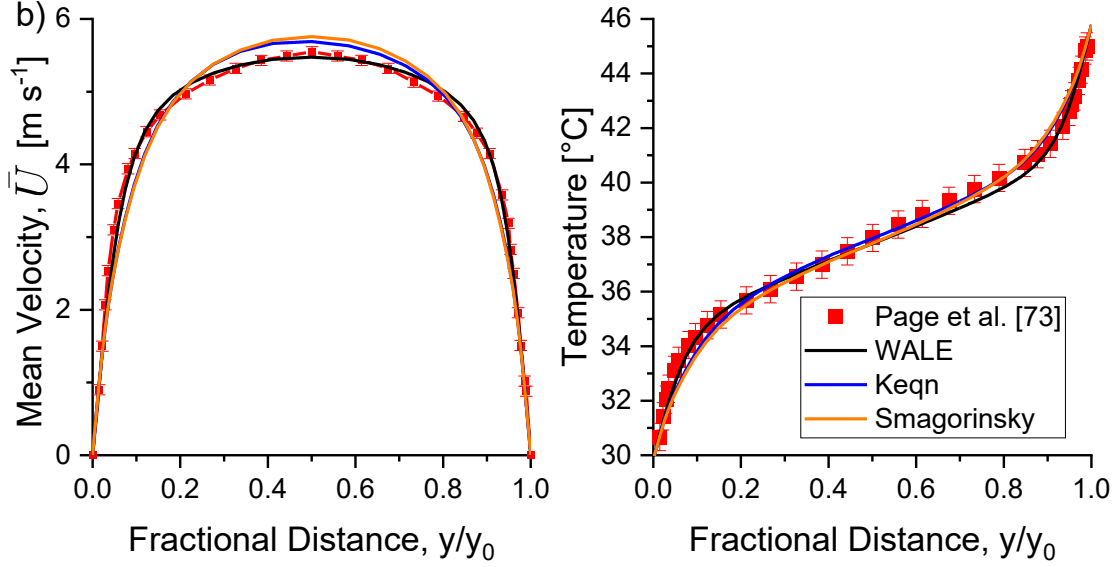


Figure 3.4 Grid sensitivity analysis for Scenario 2. The comparison shows minimal differences between mesh sizes for predicted mean velocity and temperature predictions.

Finally, for Scenario 3, the numerical domain is 600 x 6117 x 960 mm³. Due to the symmetrical setup of the experiment, only one cavity was simulated. The domain behind the adiabatic wall was also removed to reduce the computational resources required, as analysis found that the removal had a negligible effect on the result. The outlets were defined with an open boundary. A total of six different cases were investigated with cavity widths of $W = 50$ mm, 100 mm, and 200 mm for each wall heat flux of 104 W m⁻² and 208 W m⁻². The convective heat flux at the heated wall was prescribed as 83.2 W m⁻² and 166.4 W m⁻², respectively, as estimated in the experiment [88]. The boundary condition of the heated wall is as follows:

$$-k_f \frac{dT_f}{dx} = q + q_r \quad (3.21)$$

where q is the prescribed heat flux and q_r is the radiation heat flux.

For setup where the wall heat flux is 104 W m⁻², the heated wall temperature along its height was measured, while for configuration with 208 W m⁻², the velocity along the cavity was measured. The grid sensitivity analysis was performed with grid sizes of $\Delta y = 4$ mm (Coarse), 2 mm (Medium), and 1 mm (Fine) with a total cell number of 487,250, 3,898,000

and 13,155,750, respectively. As shown in Figure 3.5, the grid sensitivity analysis shows that when a coarse mesh is used, a significant difference in the predicted velocity is observed, where the average difference between Fine and Coarse mesh is 28.7%. Conversely, the difference between Fine and Medium mesh is only 4.0%. For the predicted temperature, the average difference between Fine and Coarse is 15.2%, while between Fine and Medium, it is 3.2%. Since the difference between Fine and Medium is small, the Medium mesh size was chosen for validation in this scenario. Figure 3.6 shows the final numerical setup and configuration of each scenario.

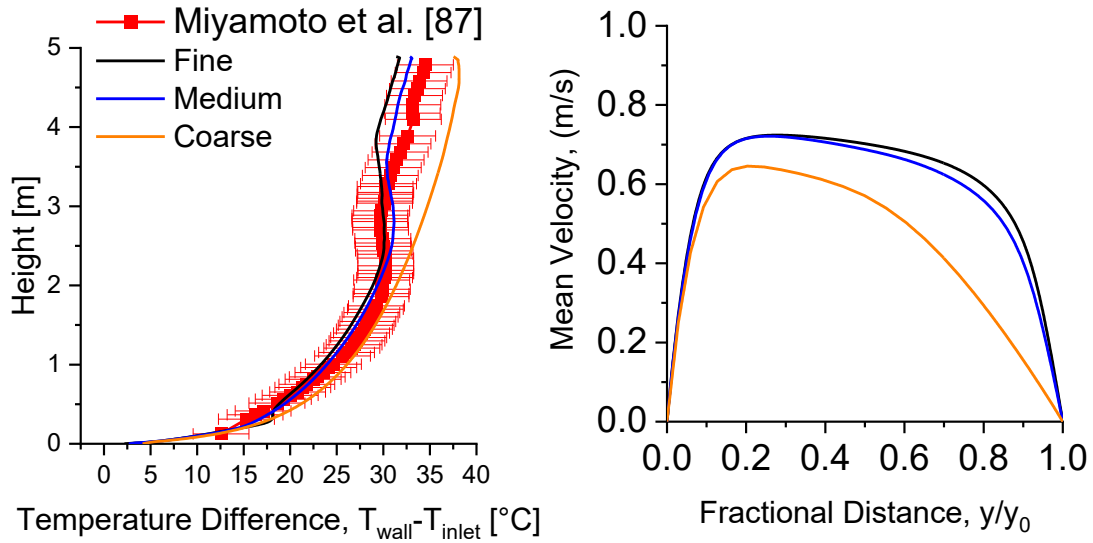


Figure 3.5 Grid sensitivity analysis for Scenario 3. For Coarse mesh, simulation results show that huge differences are recorded when compared to both Medium and Fine mesh. The Medium mesh was chosen for validation due to negligible differences between the Fine mesh.

Table 3.1 Summary of the numerical settings for Scenario 1 – 3 and Reynolds number involved in each scenario.

Note that Reynold numbers in Scenario 3 are not known as fluid flow is caused by buoyancy.

Scenario	Grid size (mm)	Reynolds number	Total Numerical cell
Scenario 1	0.62	13,800	1,400,000
Scenario 2	0.62	9,370	480,000
Scenario 3	2.00	-	3,898,000

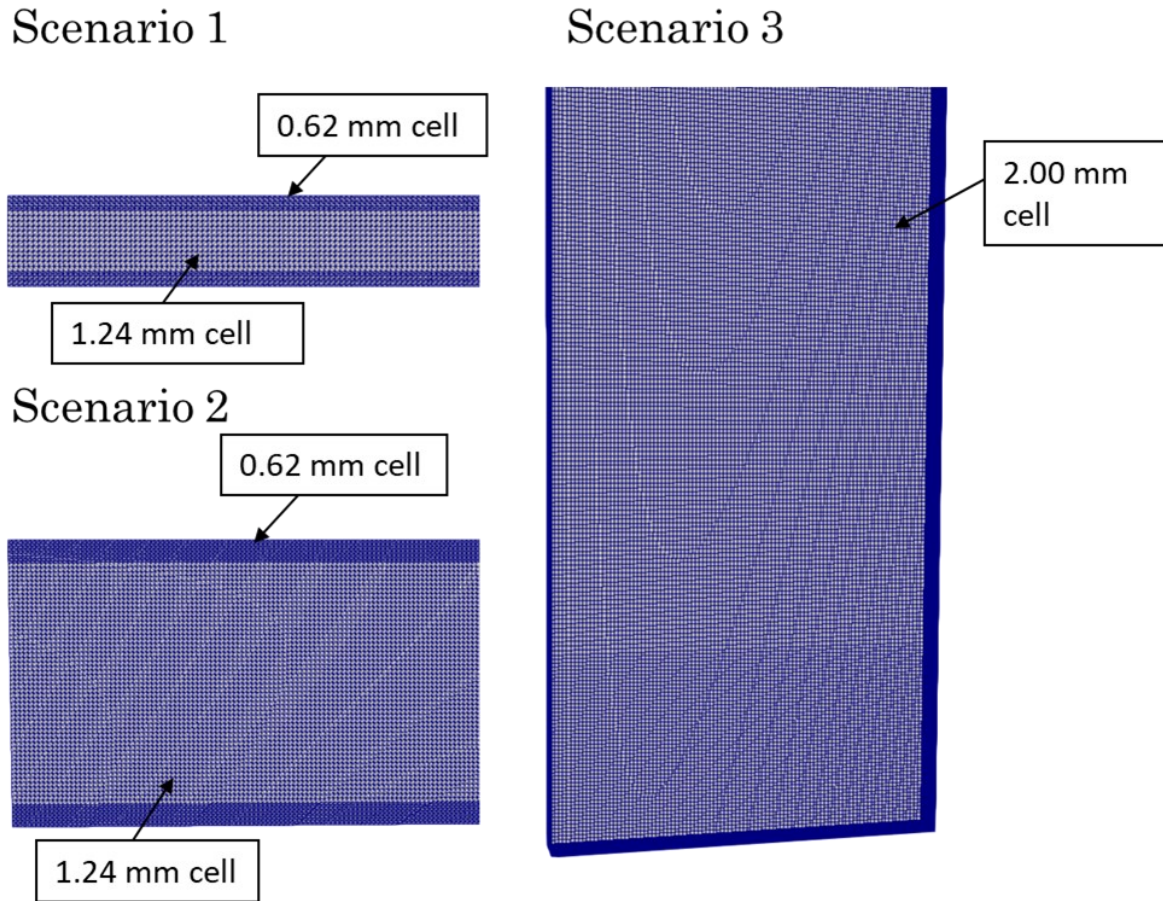


Figure 3.6 Setup of the simulations of the three Scenarios. Mesh refinement was present near the wall where cell size is halved in the normal direction.

Results

3.5.1 Scenario 1 – Fluid Flow Validation

The analysis shows that predictions of the three turbulence models' mean velocity profile, friction velocity, and turbulent velocity fluctuation fit the experimental data with reasonable accuracy, as presented in Figure 3.7a. The results show that all models can predict the fluid flow to a high degree of accuracy found to be within 10% of the experimental measurement, as shown in Table 3.2. The results show that the k-equation and Smagorinsky model performs slightly better at predicting the log law velocity profile when compared to the WALE model, as shown in Figure 3.7b. This is attributed to the Van Driest damping function that helps to predict velocity gradient correctly and, therefore, better friction velocity prediction [98]. However, one slight disadvantage of this damping function is that it does not work well in a complex turbulent flow due to its global dependence on the dimensionless wall distance, which could differ in different areas of the domain.

To ensure the turbulence quantity is captured with reasonable accuracy, the velocity fluctuation of different turbulence models is compared to the experimental measurement, as shown in Figure 3.7c and Figure 3.7d. The results found that the predicted velocity fluctuations by the three models at the centre of the channel and the peak fluctuation were similar to the experimental result. However, all three models overpredict at the near-wall region by an average of 30%, with both k-equation and Smagorinsky models predicting the fluctuations better than the WALE model initially before overpredicting the fluctuation closer to the centre of the channel. As aforementioned, using the Van Driest damping function for both k-equation and Smagorinsky models may have improved the prediction in a less complex flow.

Table 3.2 Mean Relative error and bounded relative error for Scenario 1 over the various measurements.

Smagorinsky and K-equation model performs slightly better due to the Van Driest wall function.

	Mean velocity, \bar{U}		Log law velocity, $\frac{U^+}{U_\tau}$		Velocity intensity, $\frac{\sqrt{u'^2}}{\bar{U}}$	
	RE^M	RE^b	RE^M	RE^b	RE^M	RE^b
WALE	6.4%	6.3%	12.4%	12.3%	24.8%	23.2%
Smagorinsky	5.9%	5.9%	7.9%	7.8%	19.7%	18.2%
K-equation	5.8%	5.6%	7.6%	7.6%	21.4%	19.7%

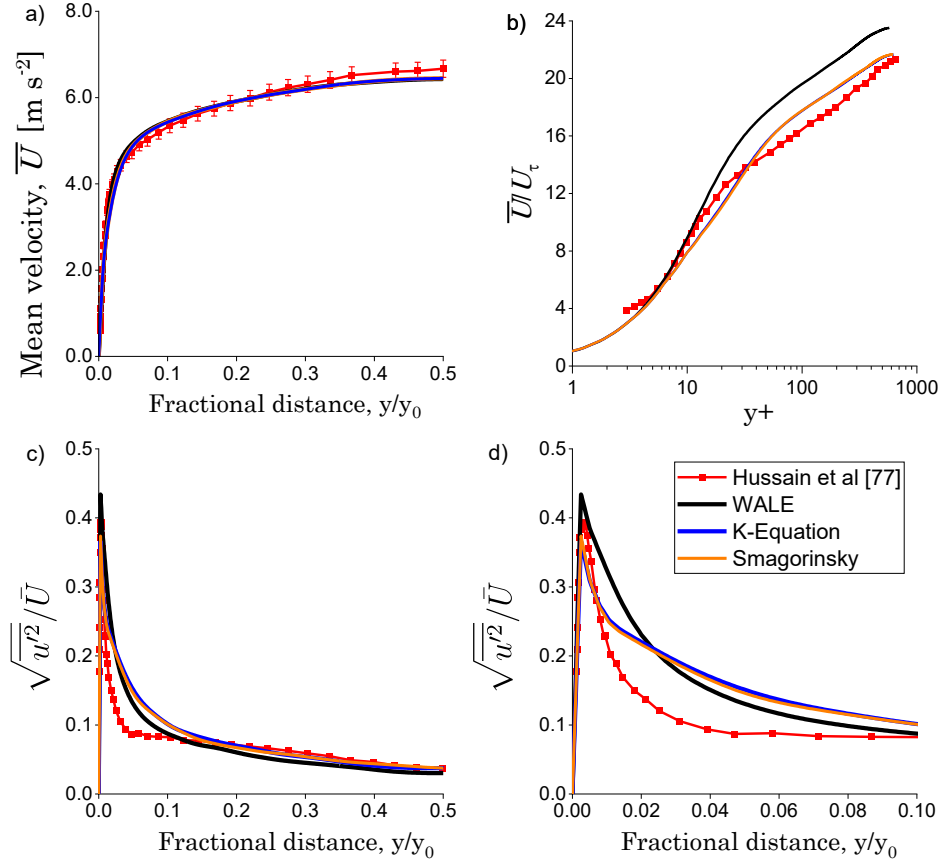


Figure 3.7 Predicted a) wall normal variation of the mean velocity profile b) log law velocity profile c) Dimensionless velocity intensity profile d) Dimensionless velocity intensity profile near the wall of Scenario 1.

The simulation result shows that all turbulence models accurately predict flow velocity in a narrow cavity.

3.5.2 Scenario 2 – Heat Transfer Validation

For Scenario 2, all three turbulence models could accurately capture the velocity and temperature profile with a maximum error of approximately 20%, as shown in Figure 3.8a and

Table 3.3. For the heat flux, the WALE model was able to predict the heat flux slightly more accurately compared to both k-equation and Smagorinsky. The wall heat flux, q_w measured in the experiment is 150 W m^{-2} . The WALE model predicted a heat flux of 102 W m^{-2} , while k-equation and Smagorinsky both predicted 93 W m^{-2} . The reason for this discrepancy is that both k-equation and Smagorinsky models tend to take an incorrect value of ν_{sgs} near the walls as the model fails to eliminate ν_{sgs} near the wall, increasing substantially before a sudden reduction to zero due to the Van Driest damping function, as shown in Figure 3.8b. This meant that k-equation and Smagorinsky models might predict a more turbulent flow near the wall. This phenomenon was observed by Yuen et al. [69], who found that turbulent generation at the ceiling in a compartment fire is greater for models that require a damping function. In contrast, the WALE model could predict the vanishing value of ν_{sgs} near the wall without a damping function and hence a more accurate flow at the wall.

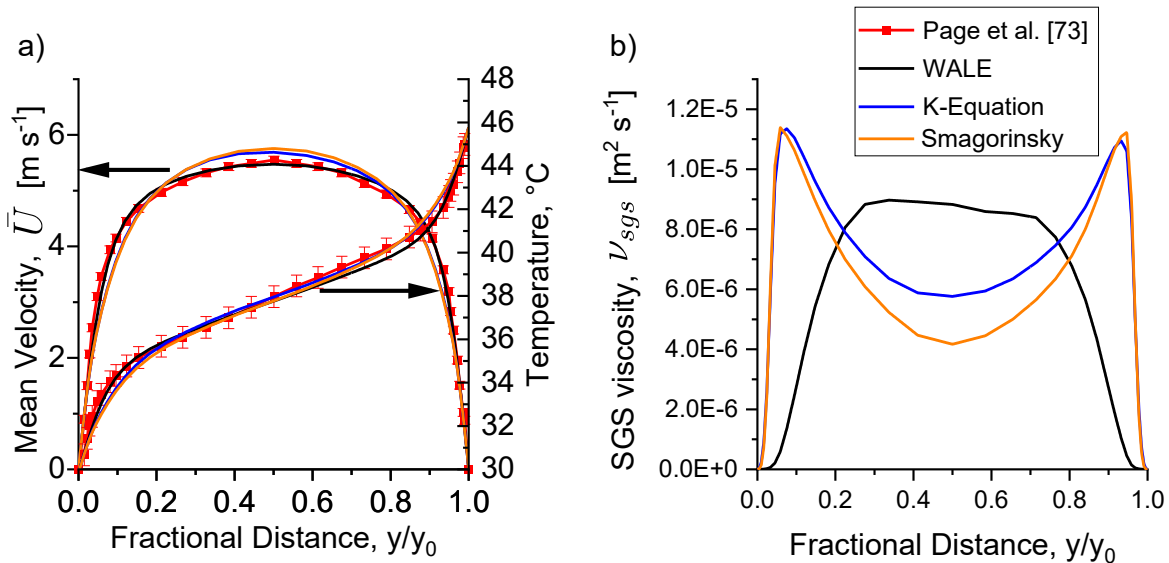


Figure 3.8 Simulation results of Scenario 2 where a) All turbulence models captured the mean velocity and temperature profile with good accuracy. b) vanishing value of SGS viscosity at the wall was only predicted accurately by the WALE model

The simulation results were further non-dimensionalised and compared to the DNS results by Lyon et al.[82] to validate the accuracy of the fluctuating temperature prediction. DNS simulation result was used to validate the model due to the lack of reliable temperature measurement near the wall at high flow speed [99]. The two variables that are evaluated were the normalised temperature and the normalised r.m.s temperature distribution, described as (3.22) and (3.23) respectively:

$$\bar{T}^+ = \frac{T_w - \bar{T}}{T_\tau} \quad (3.22)$$

$$\theta'^+ = \frac{\theta'}{T_\tau} \quad (3.23)$$

$$T_\tau = \frac{q_w}{\rho c_p U_\tau} \quad (3.24)$$

where the superscript + denotes normalisation by wall variable i.e. friction velocity U_τ , and friction temperature, T_τ . T_w is the wall temperature \bar{T} is the mean temperature, θ is the excess temperature, and the superscript ' denotes fluctuating component.

Figure 3.9 and

Table 3.3 shows that when compared to DNS results, all three turbulence models show an accurate prediction of the mean temperature measurements with an error of within 20% at the centre, but when comparing the temperature fluctuation, the WALE model was observed to have a closer prediction to the DNS result with an average error of 6.7%.

The simulation results in Scenario 2 show that the WALE model could predict v_{sgs} more accurately near the wall and the fluctuation temperature, both of which are vital in the accurate prediction of near-wall combustions and wall heat flux [45, 69]. Hence, the chosen turbulence model is the WALE model for future scenarios.

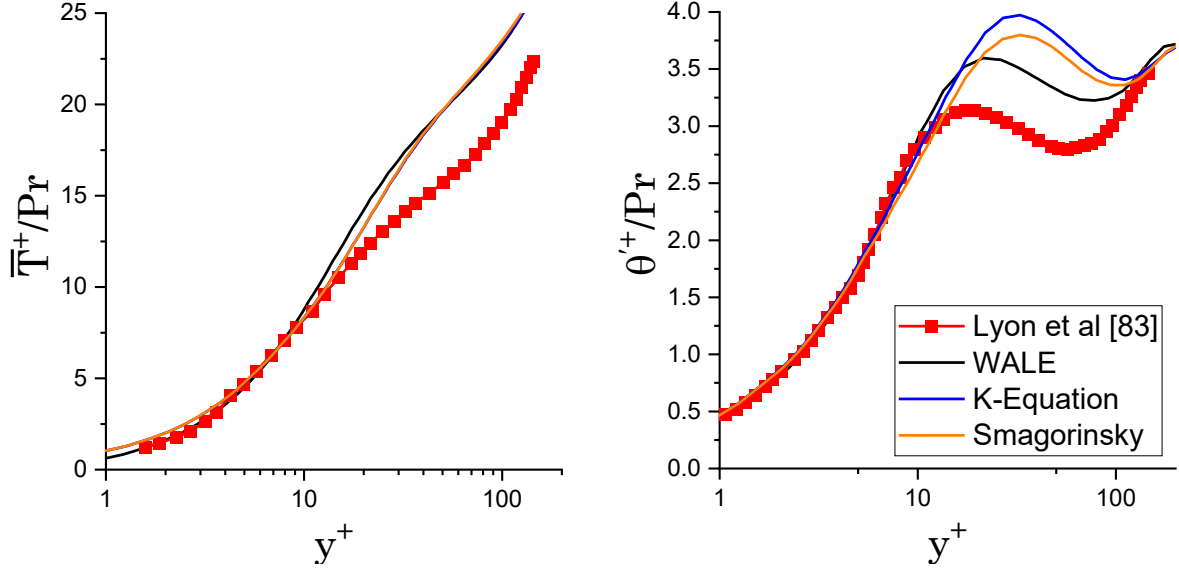


Figure 3.9 Simulation results of Scenario 2 were a) dimensionless mean temperature distribution. b) non-dimensional r.m.s temperature distribution model. The prediction shows that the WALE model performs slightly better near

Table 3.3 Mean Relative error and bounded relative error for Scenario 2 over the various measurements. WALE model performs better likely due to better prediction of v_{sgs} near walls

	Mean velocity, \bar{U}		Temperature, T		Dimensionless Mean Temperature, $\frac{\bar{T}^+}{Pr}$		Dimensionless Temperature Fluctuation, $\frac{\theta'^+}{Pr}$	
	RE^M	RE^b	RE^M	RE^b	RE^M	RE^b	RE^M	RE^b
WALE	4.6%	4.6%	0.6%	0.6%	14.7%	14.5%	8.8%	6.7%
Smagorinsky	11.9%	11.7%	1.3%	1.3%	16.1%	15.8%	12.4%	9.6%
K-equation	8.8%	8.8%	0.9%	0.9%	15.7%	15.5%	14.5%	11.2%

3.5.3 Scenario 3 – Buoyancy Validation

When the wall heat flux is 208 W m^{-2} , the results show that the model could capture the velocity profile due to buoyancy within an average of 30% error for all cavity widths, as demonstrated in Figure 3.10 and Table 3.4. The uncertainty of the convection heat flux generated from the heated wall may partially explain the differences, although it is unlikely that it is the main reason for the discrepancies.

As for the 104 W m^{-2} case where the heated wall temperature was measured, the local maxima of the heated wall temperature were predicted to be slightly higher than the experiment errors within 20%, although the general temperature trend was captured, as shown in Figure 3.11. The simulation results showed that the convective heat transfer coefficient on the wall was in the range of $3 \text{ W m}^{-2} \text{ K}^{-1}$ to $20 \text{ W m}^{-2} \text{ K}^{-1}$.

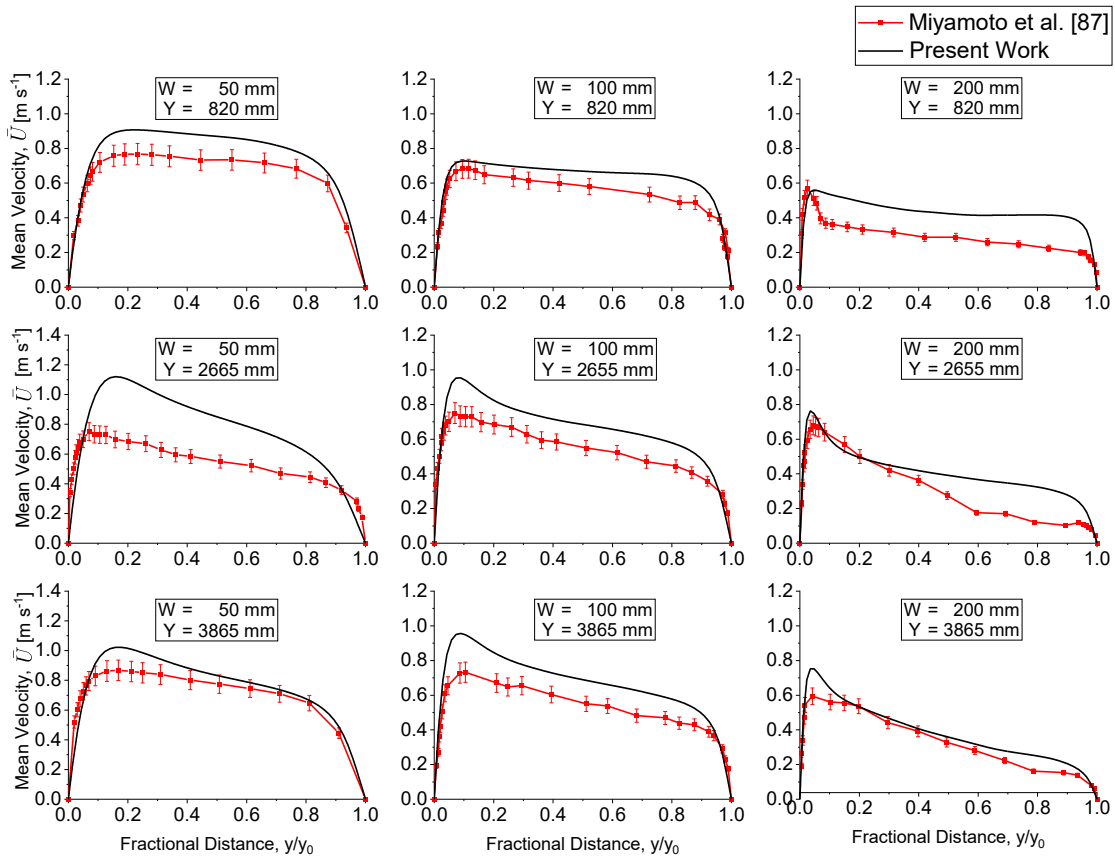


Figure 3.10 Comparison of experimental and predicted velocity profiles for cavity widths of $W = 50 \text{ mm}$, 100 mm , and 200 mm at the height of $3,865 \text{ mm}$ for $q_w = 208 \text{ W m}^{-2}$. The model could capture the general velocity profile, although velocity tends to be overestimated near the wall.

The turbulent characteristic for 104 W m^{-2} was also compared to the experimental result for cavity widths of 100 mm and 200 mm at $Y = 3,840 \text{ mm}$. The result shows that it could predict both velocity and temperature intensity profile and temperature to a reasonable degree with errors within 35%, as shown in Figure 3.12 and Table 3.4. However, similar to the prediction of the velocity profile, the model tends to overpredict the vertical velocity intensity near the heated wall for the cavity width of 100 mm. At the centre of the cavity, the vertical velocity intensity was underpredicted for both cavity widths. As for the normal velocity intensity, the model overpredicts for 100 mm cavity width, while for 200mm cavity width, the simulation was found to be predicted accurately predicted. One potential reason for these errors was the simulation's ability to predict the convective heat transfer at the laminar region, where mesh size is required to be very fine. Lastly, the temperature intensity prediction by the model was found to be accurately predicted throughout the cavity.

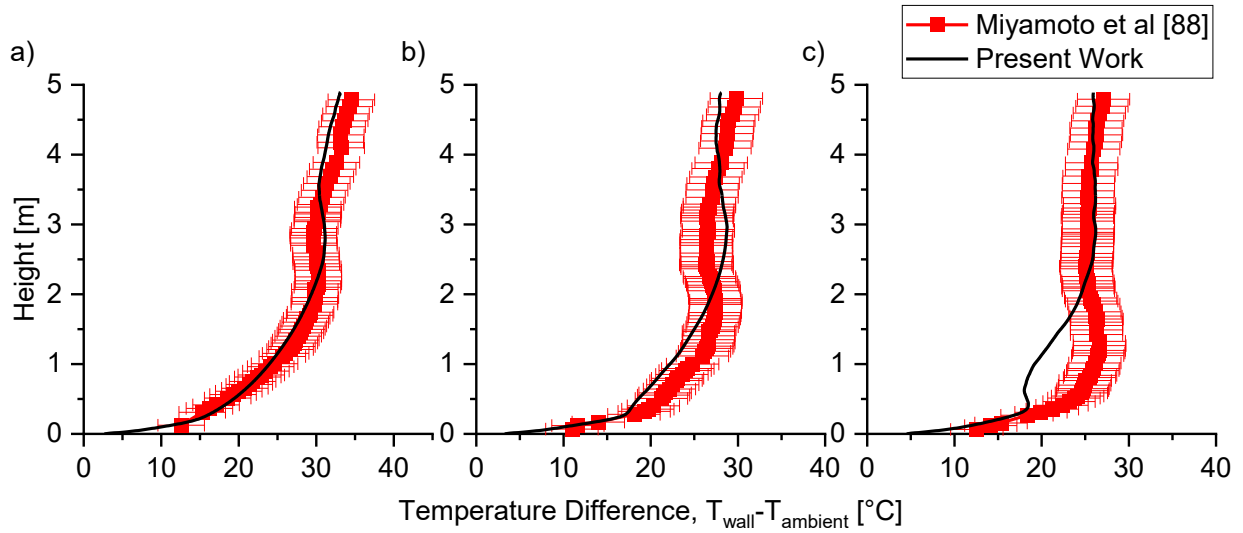


Figure 3.11 Comparison of experimental and predicted heated wall temperature of a) 50 mm, b) 100 mm, and c) 200 mm cavity for $q_w = 104 \text{ W}$. The model captured the general trend, but local maxima tend to be predicted slightly higher up

These results indicate that the model could predict the general trend of both wall temperature and velocity profile in a cavity due to natural convection and buoyancy. However, the results show that the introduction of buoyancy significantly increased the complexity of the problem and the difficulty of predicting fluid dynamics in the cavity.

Therefore, it is essential to be aware that while the model can accurately predict the general trend, it should still be used with caution as local field predictions may be erroneous.

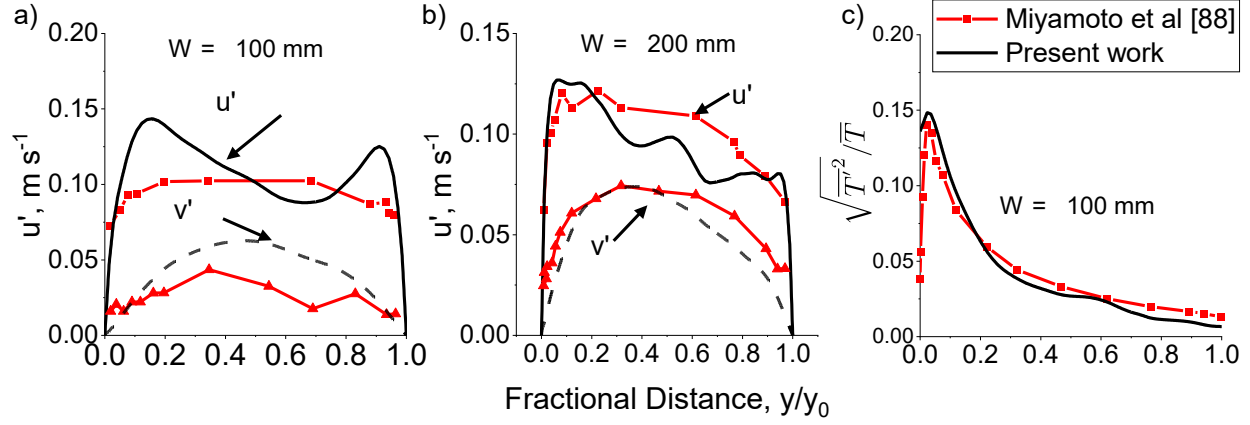


Figure 3.12 Comparison of experimental and predicted velocity intensity profile for cavity widths of (a) 100 mm and (b) 200 mm velocity and (c) temperature intensity profile when $q_w = 104 \text{ W m}^{-2}$ at the height of 3865 mm for a cavity width of 100 mm. The model was able to capture the general trend of the turbulent characteristic.

Table 3.4 Mean Relative error and bounded relative error for Scenario 3 over the various measurements. After the addition of buoyancy, the relative error increased drastically.

Cavity width, mm	Mean velocity, \bar{U} (208 W m ⁻²)		Temperature, T (104 W m ⁻²)		Velocity intensity, (104W)		Temperature intensity fluctuation, $\frac{\sqrt{T'^2}}{T}$ (104 W)	
	RE^M	RE^b	RE^M	RE^b	RE^M	RE^b	RE^M	RE^b
50	24.6 ± 8%	23.9 ± 8%	17.1 ± 10%	16.9 ± 10%	N/A	N/A	N/A	N/A
100	28.4 ± 8%	27.3 ± 8%	16.8 ± 10%	16.6 ± 10%	40.3%	34.6%	23.4%	22.4%
200	49.0 ± 8%	39.7 ± 8%	14.0 ± 10%	13.9 ± 10%	24.2%	22.3%	N/A	N/A

3.6 Conclusion

I study the ability of the FireFOAM model to predict the cavity fire with varying widths and configurations here. As facade cavity fire is a multiphysics process where different physical phenomena interact with each other to produce a non-linear and complex problem, the present work proposed an approach to validate each physical phenomenon in a narrow cavity configuration. Current cavity fire models are validated with all physical phenomena involved at once, which may not be appropriate for a narrow cavity fire scenario. This is because the validated model may be affected by the compensation effect, where a fortuitous validation result could be obtained due to multiple wrongly predicted physical phenomena. To limit the compensation effect of the model, the current work performs a step-by-step validation to ensure each physical phenomenon is predicted accurately in a narrow cavity configuration. The present work includes fluid flow, heat transfer, and buoyancy models.

Simulation results from Scenario 1 and Scenario 2 show that the presented model can simulate both fluid flow and heat transfer accurately. Analysis from both scenarios indicates that the WALE turbulence model is a more appropriate model for facade cavity fire due to the walls' proximity in the cavity. The result shows that the WALE model can predict the temperature gradient, velocity profile, and fluctuating velocity and temperature in a turbulent flow more accurately than the k-equation and Smagorinsky models in a narrow cavity. In addition, the ability of the WALE model to predict the vanishing value of SGS viscosity and kinetic energy without relying on the damping function meant that it might be more suitable for predicting convective heat flux and combustion near the walls.

The model's ability to predict buoyancy was also validated. The simulation results show that the model slightly overpredicts the airflow in the cavity by an average of 30%. This overprediction could be due to applying a higher convective heat flux as a boundary condition due to the experimental convective heat flux uncertainty. The results also show that the model could predict the general trend of the heated wall temperature and turbulence characteristic with reasonable accuracy, indicating that the model is capable of predicting the overall effect of buoyancy in a narrow cavity. However, caution needs to be taken as local field predictions may be erroneous.

Lastly, the validated scenarios show that the model prediction of various fluid dynamics in a cavity was affected as more physical phenomena were introduced. This is expected as flow in a narrow cavity is a strongly coupled problem, and any additional physical phenomena may affect the overall predictions. The results from the numerical methodology developed show that a step-by-step validation can help to develop a robust and reliable model for a cavity fire scenario as it reduces the degrees of freedom when modelling a more complex scenario. The results show that the three physical phenomena simulated by the model show good agreement with the experimental result.

Chapter 4

Addition of a Combustion Model inside the Narrow Cavity of a Facade

Summary³

This chapter studied the combustion physical phenomena for FireFOAM in a narrow cavity fire. The study of combustion inside a non-combustible facade cavity is an important first step in understanding the fire dynamics in a cavity, as modelling pyrolysis at the same time may result in compensating effects. Studying combustion in a non-combustible facade would also provide information on the effect of combustible materials in a cavity fire. A total of ten cases are studied with five different cavity widths and two different burner heat release rates (HRR). Eight of the ten cases were validated against experimental data from the literature. Simulation results show that the model accurately predicts the flame height decreases with increasing cavity width within an average error of 14.9%. However, for a higher burner HRR and narrower cavity width, the predicted flame height error increases to 30%. As for the maximum upward exit velocity, the model could predict it with an accuracy of 20%. The model also found that flame splits at the centre in a narrower cavity due to air entrainment from the sides, creating flow circulation that moves fuel laterally. The model predicts the overall incident heat flux to decrease with increasing cavity width. The results show that the model can study cavity fires with significant credibility.

³ This chapter is based on a submitted paper: B. Khoo, W. Jahn, M. Bonner, P. Kotsovinos, G. Rein, Step-by-Step Development of Multiphysics Simulation in a narrow Cavity.

4.1 Introduction

In chapter 2, I discussed the development of fire modelling and how fire modelling could help to improve our understanding of narrow cavity fire. I have also mentioned that the physical phenomena of current CFD models of fire-driven flow are validated step-by-step for open-air fire or compartment fire. Furthermore, I stated that the five physical phenomena involved in a cavity fire are strongly coupled, resulting in the need to validate the model step-by-step for each physical phenomenon in a narrow cavity. In the previous chapter, I demonstrated that the model could capture three of the five physical phenomena; fluid flow, heat transfer and buoyancy; with reasonable accuracy, and in this chapter, the ability of the model to predict combustion in a narrow cavity will be explored.

The combustion process is a complex phenomenon that involves many stages. Early treatment to fire modelling is approached using a volumetric heat source where the source term in the energy equation is modified. This neglects the need to model combustion chemistry whilst allowing practitioners to study the buoyancy effect on fluid flows [100]. Unfortunately, this approach does not consider the flame's combustion products, fire development, or radiation heat transfer which could significantly affect temperature prediction near the wall [73]. As computation power increases, combustion and flame radiation models have been developed to overcome these shortcomings. The combustion process can be described as a single global exothermic reaction in its simplest form. However, such descriptions only define the energy released by fuel and do not describe the reaction rate. Hence, the challenge associated with modelling fire accurately is having an accurate expression of the mean reaction rate [101].

The primary considerations in calculating the mean reaction rate are the air-fuel mixture time scale and chemical kinetics. Depending on the length scale of the fire we are investigating, the physical expression can be simplified without losing much accuracy [102]. Figure 4.1 shows the length and time scales of each of the processes present during a fire. Since the engineering length scale is of interest to our problem, the chemical kinetics involved in the fire need not be resolved to obtain an accurate result. This is due to the overall reaction rate of these fires being controlled primarily by the turbulent mixing time scale of fuel and oxidant at this length scale. Since the chemical reaction plays a lesser role, the combustion model can assume very fast chemistry to reduce the required computational

resources. Examples of combustion models developed for these fires are the eddy break-up model [103], the eddy dissipation model [104], and the conserved scalar approach based on the mixture fraction [105].

Whilst these models have been validated rigorously against experimental data, validation of these combustion models in narrow cavity fire scenarios remains limited. In this chapter, validation of the model's capability to simulate fire in a narrow cavity will be performed over various cavity widths, and the model's limitations will be discussed in the following section.

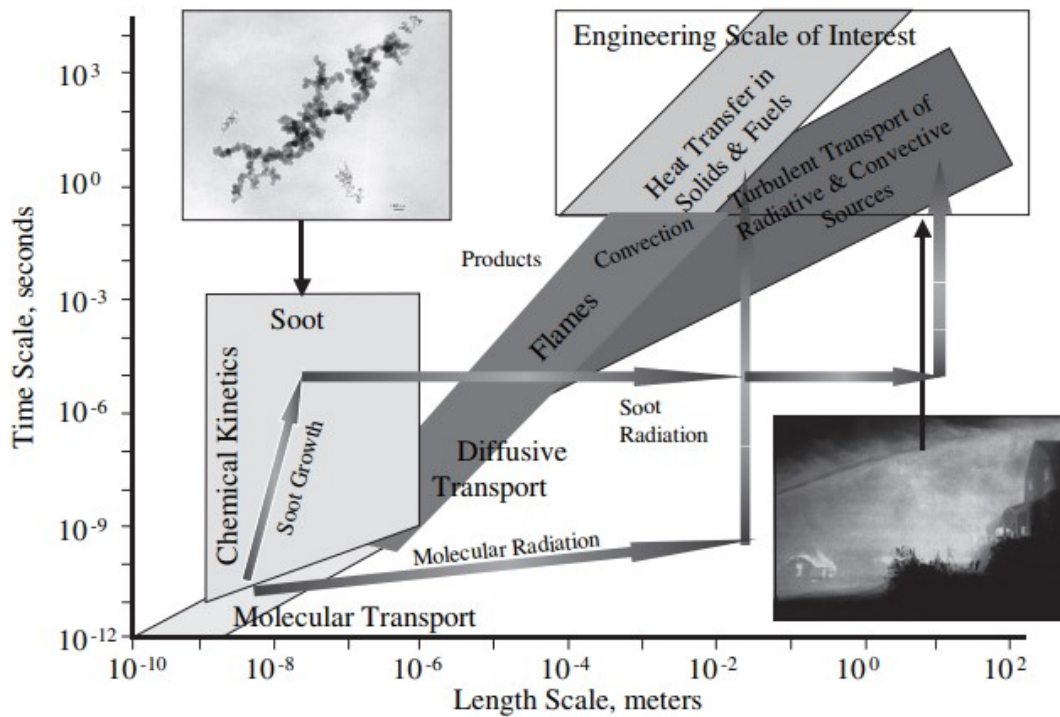


Figure 4.1 The time scales and length scale needed to resolve the required combustion phenomenon. As the engineering scale is of interest, there is no need for the model to resolve the chemical kinetics where a tremendous requirement is needed for both the time scale and length scale. (Source: [102])

4.2 Experimental Setup for Validation

Similar to Chapter 3, the experimental setup of Scenario 4 will only be briefly discussed, and the readers are referred to the original research by Livkiss et al. [28] for a more detailed description of the setup. The experimental setup consists of two parallel non-combustible vertical walls with a height of 1.8 m and a width of 0.8 m with the sides open to

induce flow spanwise. A propane gas burner with an 8 x 391 mm burner opening was placed at the centre of the cavity next to one of the non-combustible vertical walls. This wall is hereby referred to as the "near wall", whereas the other is referred to as the "far wall". The cavity width and burner heat release rate (HRR) tested in this experiment vary from 20 mm to 100 mm and 6.5 kW to 15.8 kW, respectively. Measurements in this experiment consist of exit flow velocities at the top measured using bi-directional probes and heat flux on the near wall measured using a thin skin calorimeter (TSC). A simplified schematic of the fire is shown in Figure 4.2. For this study, the model is validated with a cavity width of 40 mm, 50 mm, 60 mm, and 100mm with HRR of 6.5 kW and 12.9 kW.

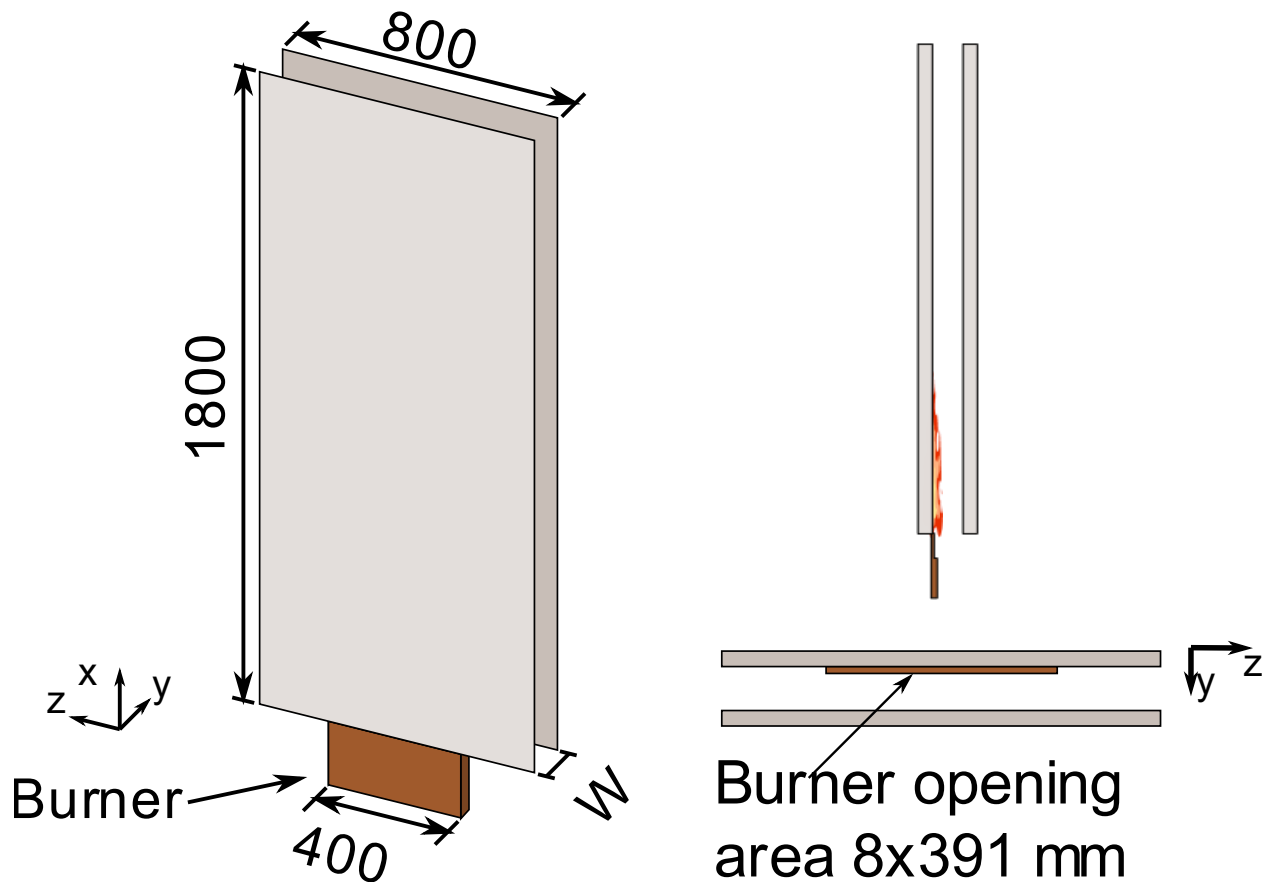


Figure 4.2 Simplified schematic of the experimental setup of Livkiss et al. used to validate the combustion model [28]. The model is validated with cavity widths of 40 mm, 50 mm, 60 mm and 100 mm.

Note that while the HRR is not as high compared to actual facade fire, this experimental setup was chosen to validate the model because three parameters of interest were measured for fire in a narrow cavity: flame height, heat flux and flow velocities, all of which

are essential in validating the robustness of the model. The validation of Scenario 4 represents the first step in developing a robust numerical methodology that accurately predicts fluid flow, heat transfer, buoyancy and combustion in a narrow cavity fire scenario.

4.3 Numerical Modelling

The numerical settings used in this study are similar to those described in Section 3.4, and readers are referred to that section for a detailed description. This section will describe only the new models introduced in Scenario 4.

Combustion

In FireFOAM, the energy released from combustion is introduced into the energy equation via the source term \dot{q}_c''' . The heat release rate per volume is obtained by summing the lumped species' mass production rates times their respective heat of formation as:

$$\dot{q}_{comb}''' = - \sum_{\alpha} m_{\alpha}''' \Delta h_{f,\alpha} \quad (4.1)$$

where m_{α}''' is the mass production per volume of the species, and $\Delta h_{f,\alpha}$ is the heat of formation of the respective species. However, while (4.1) provides the total heat released from the fuel involved in the combustion, the equation does not provide the reaction rate of the combustion. The combustion process often involves hundreds of intermediate reactions and species before becoming a final stable product. Therefore, it is no surprise that the combustion process is often severely simplified to just several or one critical reaction where the reaction rate is determined. As aforementioned, the rate of combustion is assumed to be controlled by a turbulent mixing timescale due to the fire length scale. Hence the combustion model chosen is infinitely fast.

The modified eddy dissipation combustion model (EDM) proposed by Ren et al. [93] is one of the most commonly used combustion models for FireFoam and is used in the present study. The modified EDM expressed the fuel mass reaction rate as follows:

$$\omega_F''' = \frac{\bar{\rho}}{\min\left(\frac{k_{sgs}}{C_{EDC}\varepsilon_{sgs}}, \frac{\Delta^2}{C_{Diff}\alpha_D}\right)} \min\left(\tilde{Y}_F, \frac{\tilde{Y}_{O_2}}{r}\right) \quad (4.2)$$

where $\bar{\rho}$ is the LES-filtered mass density, $\frac{k_{sgs}}{C_{EDC}\varepsilon_{sgs}}$ is the turbulent mixing timescale with model coefficient $C_{EDC} = 4$, $\frac{\Delta^2}{C_{Diff}\alpha}$ is the molecular diffusion timescale, model coefficient $C_{Diff} = 4$, α_D is the thermal diffusivity, \tilde{Y}_F is the fuel mass fraction, \tilde{Y}_{O_2} is the oxygen mass fraction, and r is the stoichiometric oxygen-to-fuel mass ratio. The combustion model coefficients are based on work done by Ren et al., where vertical wall fire is simulated [45].

The model assumes one-step complete combustion, infinitely fast, and considers irreversible chemical reactions. It assumes that in the turbulent region, the fuel-air mixing is controlled by turbulent mixing, while in the laminar region (i.e. viscous sublayer of the wall), it is controlled by molecular diffusion.

All combustions are assumed to be complete combustion described as: $C_3H_8 + 5O_2 + 18.8N_2 \rightarrow 3CO_2 + 4H_2O + 18.8N_2$. The heat of combustion of propane, ΔH_c , is 46.35 MJ kg^{-1} [106].

Radiation Heat Transfer

To calculate the radiative heat flux, the radiative transport equation (RTE) was used. The expression of the simplified RTE where scattering is not considered and the grey gas assumption is used as follows:

$$\frac{dI}{ds} = \kappa_p(I_b - I) \quad (4.3)$$

Where the I is the radiation intensity, s is the unit vector along a direction of propagation of radiation, κ_p is the Planck mean absorption coefficient and I_b is the black body radiation.

The Finite Volume Discrete Ordinates Model (fvDOM) is used in the present work to solve the RTE in FireFOAM. The method solves the radiation problem by treating the radiation intensity as a function of spatial location and angular direction and is integrated over a sphere, as shown below:

$$\nabla \cdot \mathbf{q}_R = \kappa_p \left(4\pi I_b - \int_{4\pi} I d\Omega \right) = \kappa_p 4\sigma \tilde{T}^4 - \kappa_p \sum_{i=1}^n w_i I_i(\mathbf{r}, \mathbf{s}) \quad (4.4)$$

where $I_i(\mathbf{r}, \mathbf{s})$ is the radiation intensity at a given location indicated by position vector \mathbf{r} , and direction \mathbf{s} , and w_i is the associated weights for basic discrete ordinates approximation for one octant.

The radiation emission is modelled via the radiative fraction approach to avoid the uncertainty involved in modelling the turbulent radiation interaction (TRI), soot modelling and reducing the dependency of grid size to model radiation accurately due to filtered temperature, \tilde{T}^4 . The radiative fraction approach assumes that a portion of the HRR of fuel combustion is converted into thermal radiation, as shown below

$$\nabla \cdot \mathbf{q}_R'' = \chi q_{comb}''' \quad (4.5)$$

Where q_R'' is the radiation heat flux, χ is the radiative fraction constant. The radiative fraction χ is 0.27, which is within the range found experimentally [107]. Sensitivity analysis performed using a radiative fraction of 0.27 and 0.35 was found to have a negligible difference in the current study. When comparing the total heat transfer on the near wall and heat flux to the near wall, the difference was found to be not more than 3 % and 6 % respectively, as shown in Table 4.1 Sensitivity analysis on the effect of radiant fraction. When comparing the heat flux on the near wall, wall, Finally, the number of solid angles used for the simulations is 112. Simulation results show that using a lower solid angle may result in an inaccurate prediction of wall heat flux due to the "ray effect", as shown in Figure 4.3.

Table 4.1 Sensitivity analysis on the effect of radiant fraction

Radiant Fraction	Heat Flux at 0.05 m[kW m ⁻²]	Total heat transfer [kW]
0.27	48.75	5.13
0.30	47.43	4.96
0.33	45.63	4.97
0.35	46.23	5.11

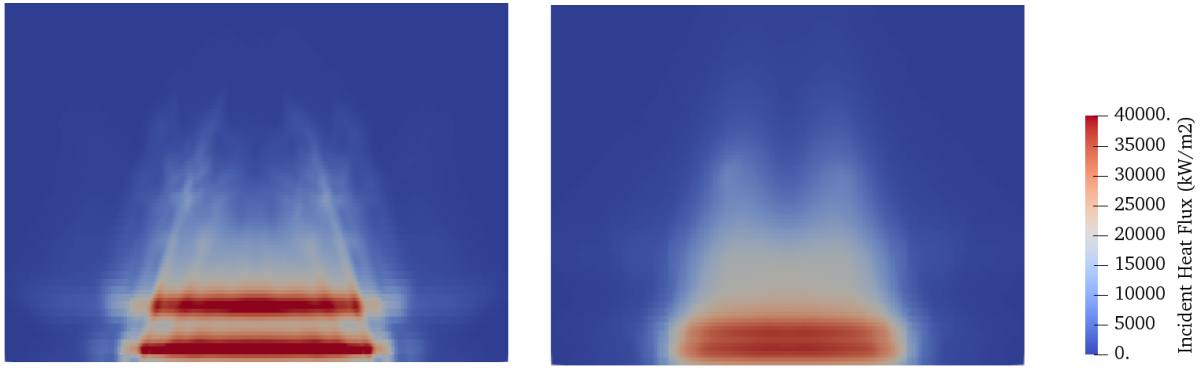


Figure 4.3 Ray effect on the far wall when 32 solid angles are used (left) and 112 solid angles are used (right)

In this study, the total incident heat flux on the wall is evaluated as:

$$q''_{total} = q''_c + \alpha q''_{in} \quad (4.6)$$

Where α is the absorptivity coefficient of the material, modelled as 1 due to soot deposit on the wall and q''_{in} is the incident radiation heat flux and q''_c is the convective heat flux.

Solid-Gas phase coupling

The convective heat transfer is calculated similarly to those shown in Chapter 3. However, in this chapter, radiative heat transfer and solid phase meshes are introduced to model the temperature behaviour of the non-combustible panel. The following equation describes the temperature change in the solid phase to couple the temperature between the solid and gas phases.

$$k_s \frac{dT_s}{dx} = q_c'' + q_r'' \quad (4.7)$$

Where k_s is the thermal conductivity of the solid material, $\frac{dT_s}{dx}$ is the solid thermal gradient, k_f is the thermal conductivity of the fluid, q_c'' is the convective heat flux and q_r'' is the radiative heat flux.

The temperature calculation at the solid-gas interface is performed by first solving the convective heat flux and radiative heat flux at the gas phase, and the information is then transferred to the solid phase. The total heat flux, along with the initial temperature field in the solid phase, is then used to solve with Eq. (4.7) to obtain the temperature of the solid phase interface. Finally, the temperature at the solid phase interface is passed to the gas phase interface at the next time step.

4.4 Computational Domain and Boundary Conditions

The numerical domain of Scenario 4, as shown in Figure 4.5, is 1200 x Y x 2100 mm³, where Y is 240, 250, 260, and 300 for cavity widths W = 40, 50, 60, 80 and 100 mm, respectively. Note that there is no 80 mm width experiment, and the simulation of this case is just for analysis purposes. Grid sensitivity analysis was performed on grid sizes of $\Delta y = 5.0$ (Coarse), 2.5 (Medium), and 1.25 mm (Fine) with a total cell number of 185,420, 850,216 and 2,942,916, respectively. The results show that the difference between the wall heat flux at the lower region for Coarse and Fine mesh is around 44%, whereas Medium and Fine mesh is only 12%, as shown in Figure 4.4. Hence, the Medium mesh size of $\Delta y = 2.5$ mm was chosen in this study to reduce the computational time required for the Fine mesh.

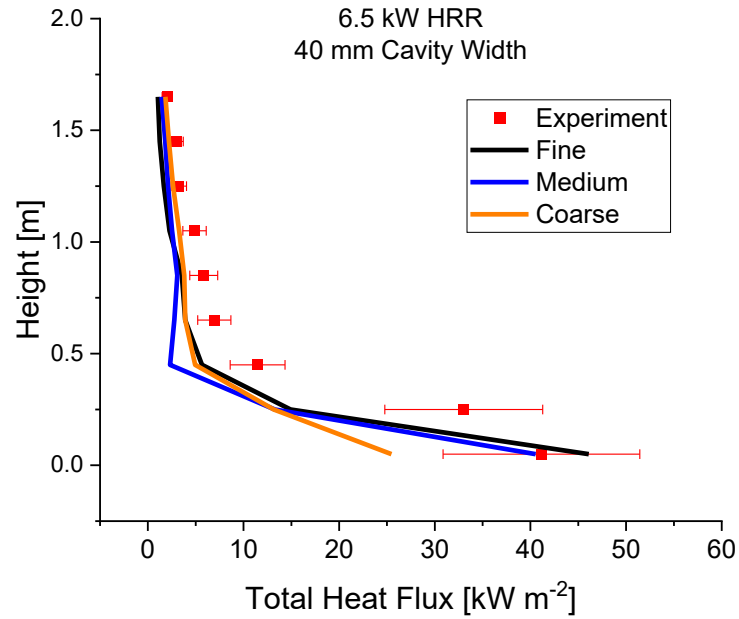


Figure 4.4 Comparison of incident heat flux between the three different mesh sizes. Results show that Coarse mesh underpredicts lower region significantly. Medium and Fine mesh was able to resolve the predicted heat flux more at this region.

For the panel, 50 cells are generated across its thickness (0.1 mm cell thickness), where the interface between the solid and gas cell is mapped onto each other. Note that a high number of solid-phase cells is needed to ensure numerical stability at the interface between the solid and gas phases. The final numerical cell settings are shown in the table below:

Table 4.2 The total numerical cell for gas and solid phases at different cavity widths.

Cavity Width	Gas Phase cells	Solid Phase cells
40 mm	862,900	5,760,000
50 mm	1,010,500	5,760,000
60 mm	1,116,340	5,760,000
80 mm	1,382,464	5,760,000
100 mm	1,664,950	5,760,000

The thermal properties of the panel are as defined in Livkiss et al. [28] with the temperature boundary conditions expressed as follows:

$$k_s \frac{dT_s}{dx} = k_f \frac{dT_f}{dx} + \alpha q_{in} - \varepsilon q_{em} \quad (4.8)$$

Where k_s is the thermal conductivity of the solid, $\frac{dT_s}{dx}$ is the thermal gradient in the solid, α and ε are the absorptivity and emissivity coefficients, both taken as one due to the reported soot, and q_{em} is the emitted radiation heat flux.

As for the side outlet, an open boundary condition is prescribed where the outflow velocity is set to zero gradients, and the inflow velocity is calculated using the pressure difference between the ambient pressure and pressure at the interface. For the top outlet, both outflow and inflow velocity is set to zero gradient to ensure numerical stability. Finally, the HRR of the burner is adjusted by setting the mass flow rate of the propane. In this simulation, a mass flow rate of 0.14 g s^{-1} and 0.027 g s^{-1} are used to simulate a HRR of 6.5 kW and 12.9 kW, respectively.

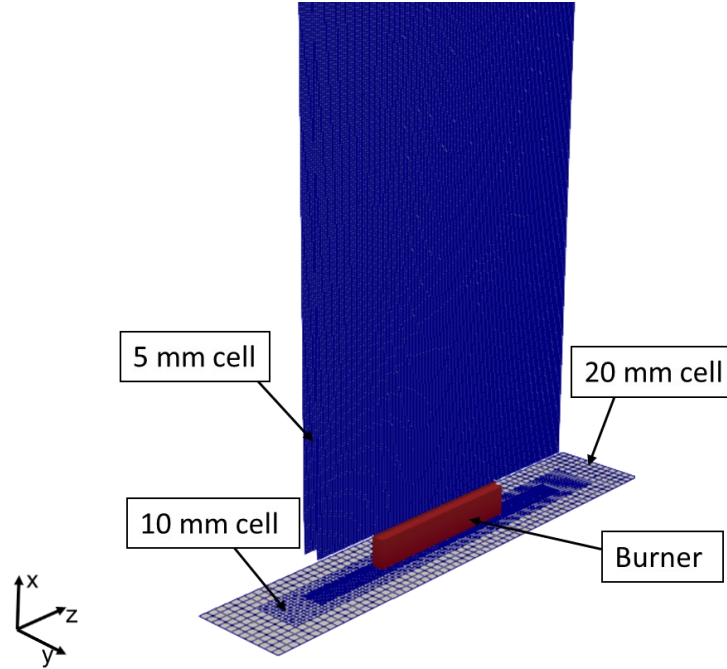


Figure 4.5 Computational Domain of Scenario 4. The size and location of the mesh refinement are as shown with further refinement applied near the panel where cell size was halved in the normal direction.

4.5 Results

Flame Height

The flame height obtained from the simulations was compared to the experimental and simulation result by Livkiss et al. [28, 49], where flame height was defined using visual analysis and cumulative HRR. Flame height was first compared with three criteria used in past literature: stoichiometric mixture fraction, 99% cumulative HRR and temperature difference of 550K with the surrounding air temperature, ΔT [108]. The median flame height between the 30th – 40th seconds was compared, as shown in Figure 4.6. The comparison showed minimal difference in flame height measured using stoichiometric mixture fraction and 99% cumulative HRR criteria. In contrast, flame height predicted using ΔT criteria is generally higher. However, using a temperature difference of 550 K for ΔT criteria is arbitrary, and it may not be a suitable indicator of flame height. The flame height criterion chosen in this work is the stoichiometric mixture fraction criteria, and it is compared to Livkiss's, as shown in Figure 4.7.

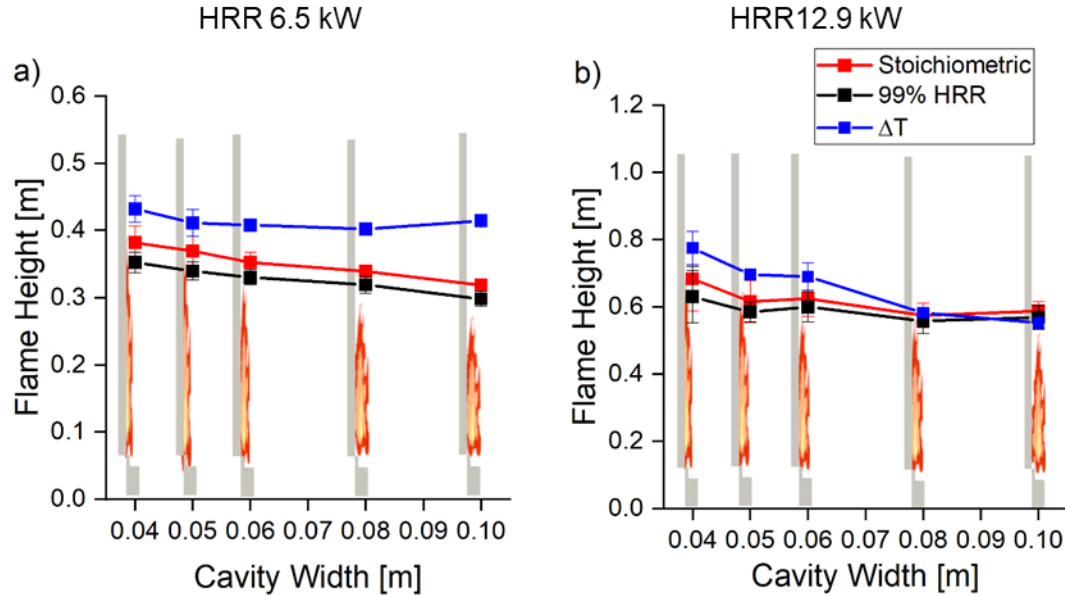


Figure 4.6 Comparison of flame height using three criteria: Stoichiometric Mixture Fraction, 99% cumulative HRR and $\Delta T = 550$ K. The comparison showed $\Delta T = 550$ K tends generally predict a higher flame height, while stoichiometric mixture fraction and 99% cumulative HRR predict a similar flame height.

The results show that for both burner HRRs, the model tends to underpredict the flame height. Results show that flame heights predicted by the model were more accurate for lower burner HRR, where underpredictions are around 4% - 15% of the experimental flame height, as shown in Figure 4.7 and Table 4.3. In comparison, at higher burner HRR, the flame heights were underpredicted by about 10% - 30%, with the 40 mm case underpredicted by 30%. The present result is similar to the simulation by Livkiss, where flame heights of cavity width of 40 mm were simulated and underpredicted. One potential reason for the underprediction is the infinitely fast combustion model that may have resulted in an underprediction of flame height in a well-ventilated condition. This is due to fuel reacting with oxygen immediately at contact, which results in most combustions occurring in the first grid cell next to the burner [109]. The predicted flame height, whilst underpredicted for a narrower cavity, was observed to improve the cavity width became wider.

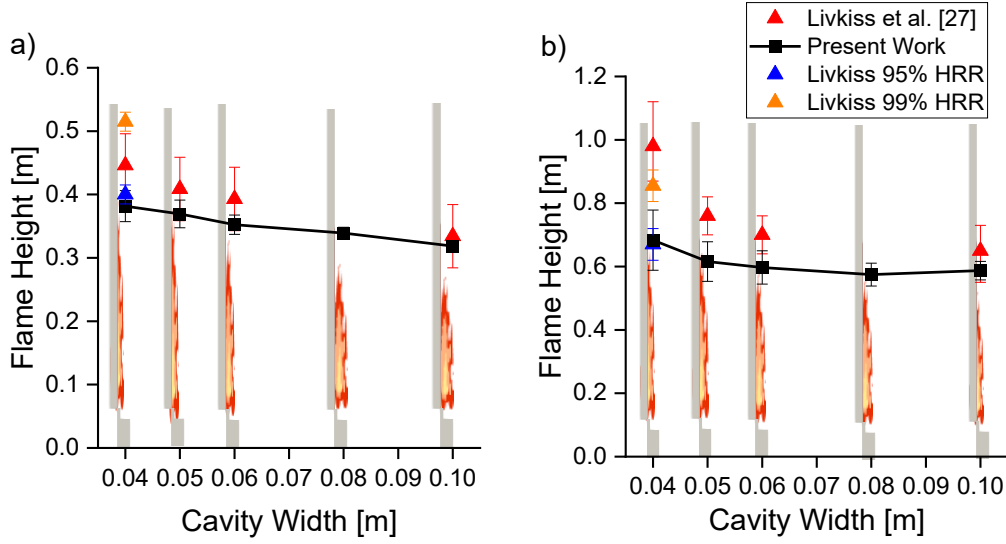


Figure 4.7 Comparison of Livkiss's experiments and prediction for the flame height where burner HRR is a) 6.5 kW and b) 12.9 kW. The model consistently underpredicts the flame height by an average of 14.9%, but the reduction of flame height with increasing cavity width is predicted well.

However, while flame heights were underpredicted in both HRRs, the model captured the general trend of flame height reducing with an increasing cavity width. Figure 4.8 shows the predicted flame height when compared to both Livkiss et al. and Karlsson et al. experimental measurements [20, 28]. The results show that the model could potentially be extrapolated to study different facade configurations.

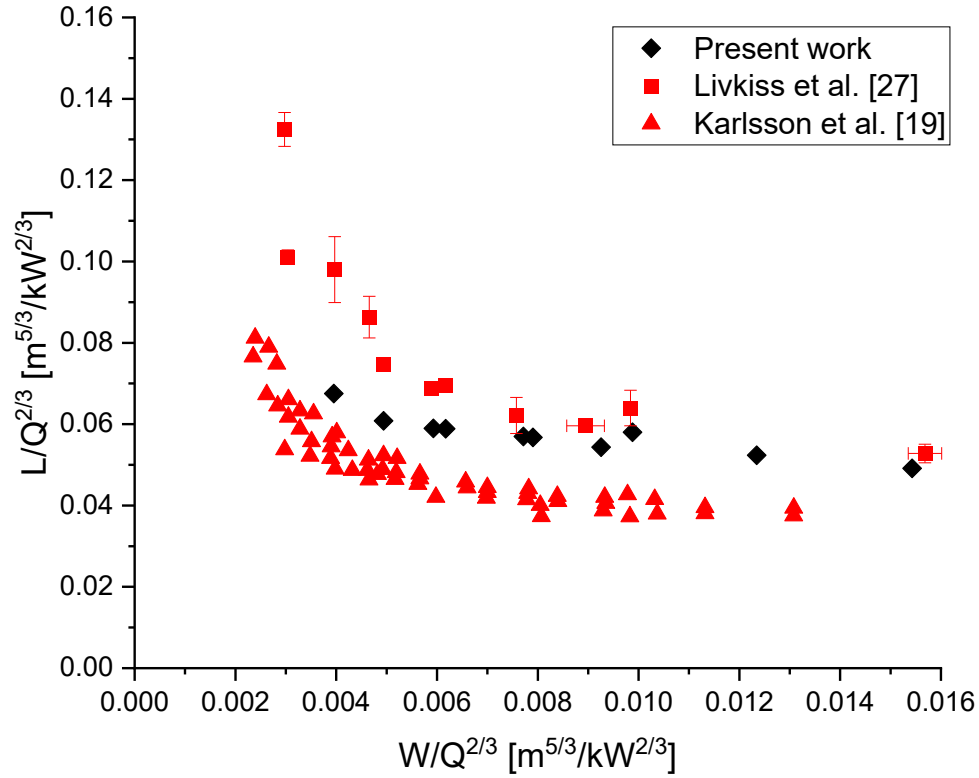


Figure 4.8 Comparison of flame height with both Livkiss et al. and Karlsson et al. experimental measurements [8, 16]. The model prediction is within the measurement of both data sets, suggesting that the model may be suitable for predicting flame height for different cavity configurations.

Flame Shape

One of the advantages of CFD simulation of fire in a narrow cavity is the ability to investigate the shape of the flame which is difficult in the experiment as the panel obstructs the camera. The current model predicts the flame to split into two peaks at a cavity width lower than 60 mm for HRR of 6.5 kW and a cavity with lower than 80 mm for HRR of 12.9 kW, as shown in Figure 4.9.

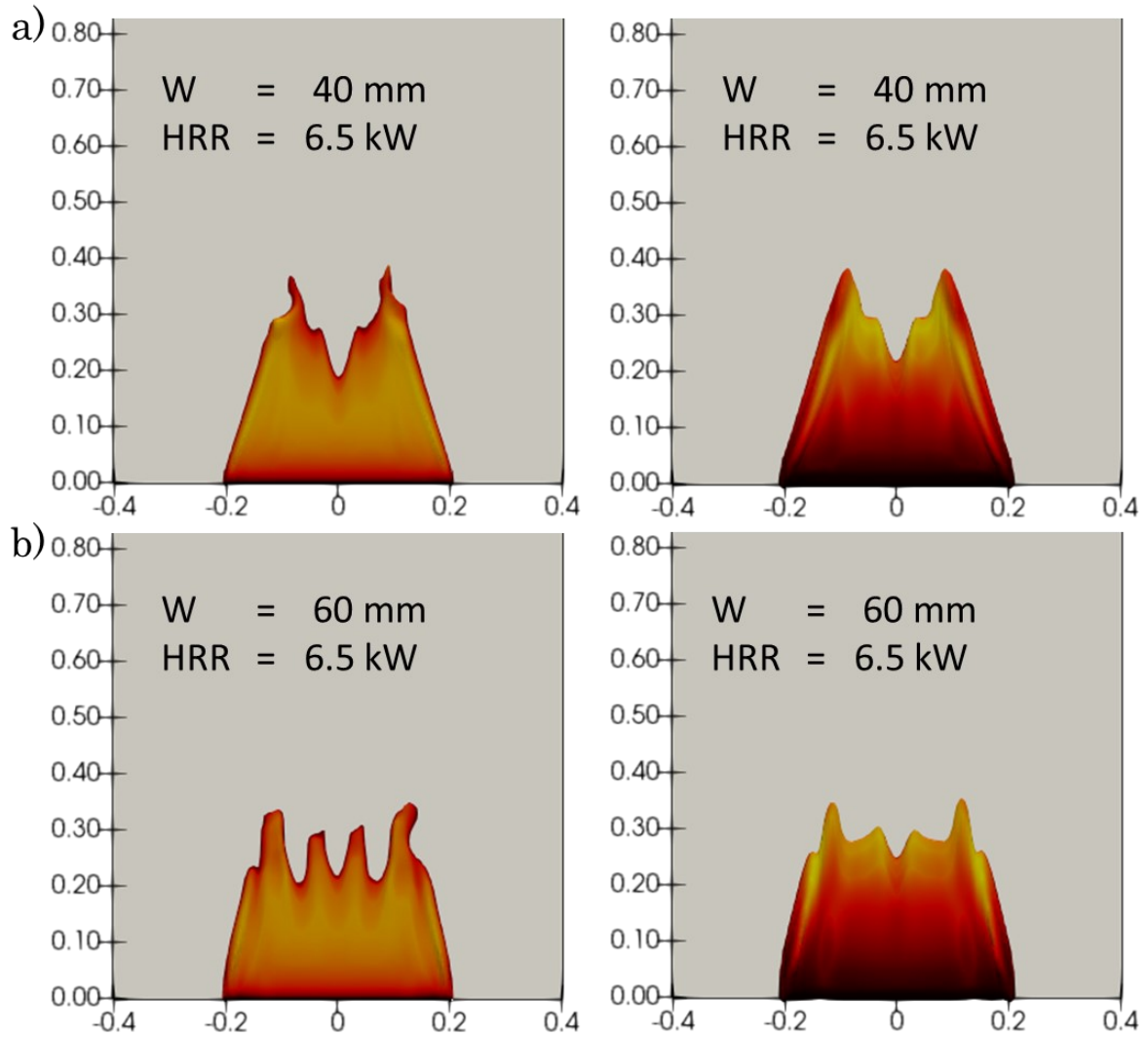


Figure 4.9 Instantaneous at $t = 40$ s (left) and average (right) flame shape for HRR of 6.5 kW for a cavity width of a) 40 mm and b) 60 mm. Simulation shows that the predicted flame shape is different as cavity width changes.

One possible explanation for the flame splitting was air entrainment from the side that forces air circulation at the centre, where fuel is forced towards the side, as shown in Figure 4.10. It is unsure whether this occurs in the experiments; however, as the mesh size is reduced, the flame was found to split at a higher point. The simulation result suggests that accurate prediction of laminar to turbulent transition is likely to affect the shape of the flame at a narrow cavity width. This is because the rate of fuel combustion is determined by the turbulent mixing of the air and fuel, which in turn determined where and how fuel is combusted.

One potential effect of the accurate prediction of flame shape is its effect on the heat flux prediction on the wall, which will be discussed in the following section.

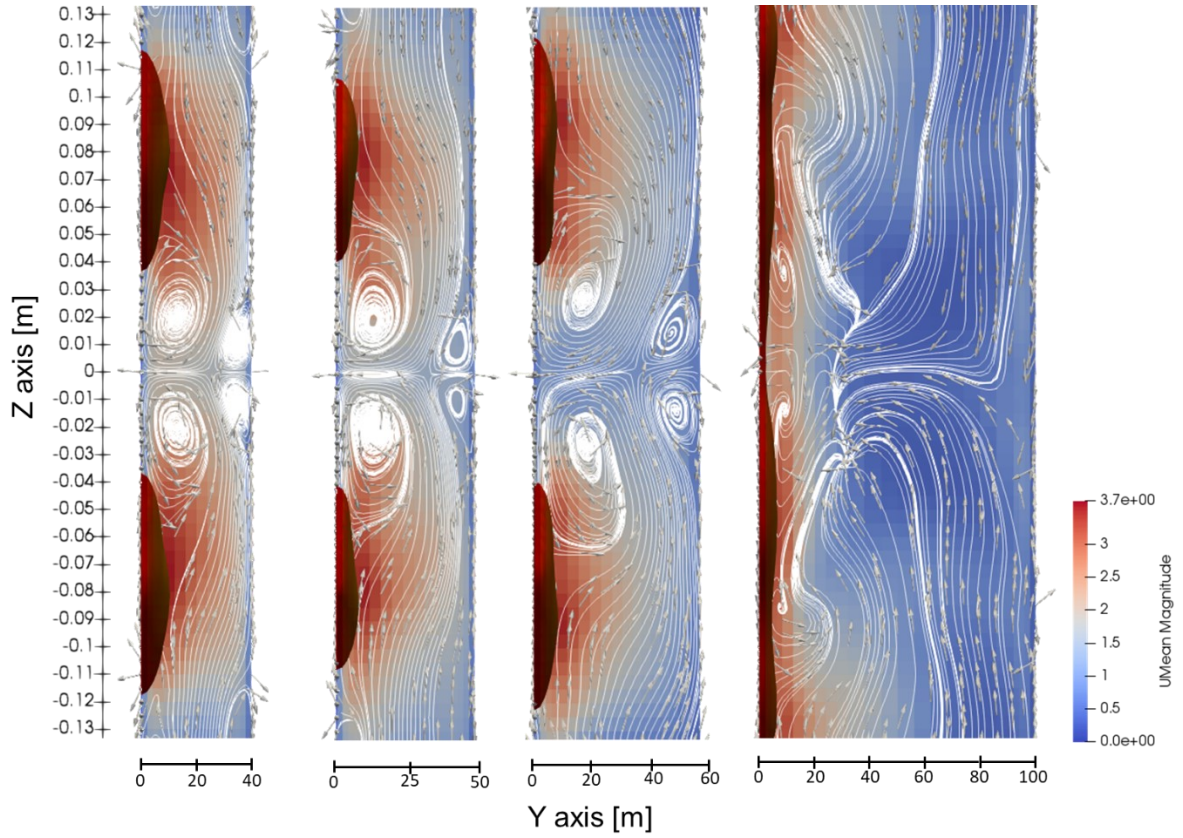


Figure 4.10 Streamline of average air entrainment from the sides for burner HRR of 12.9 kW for 40 mm and 100 mm cavity width at the height of 0.4 m above the burner. The air entrainment creates a circulation at the centre that moves the fuel away from the centre. This resulted in the flame being observed as two peaks.

Upward exit velocity

Accurate prediction of upward velocity is essential as they may affect fire dynamics and convective heat transfer over the facade panel. Additionally, accurate prediction of the upward velocity by a model indicates that the model is robust and able to simulate fluid flow despite the addition of combustion. The upward exit velocity in the experiment is measured at 1800 mm above the burner. The predicted upward exit velocities for both burner HRRs were averaged over 10 seconds. The model predicted the general trend of the velocity profile, as shown in Figure 4.11. Note that the experimental result is not

symmetrical because the placement of the gas burner may not be at the centre resulting in an asymmetrical velocity profile, as reported by Livkiss et al. [28].

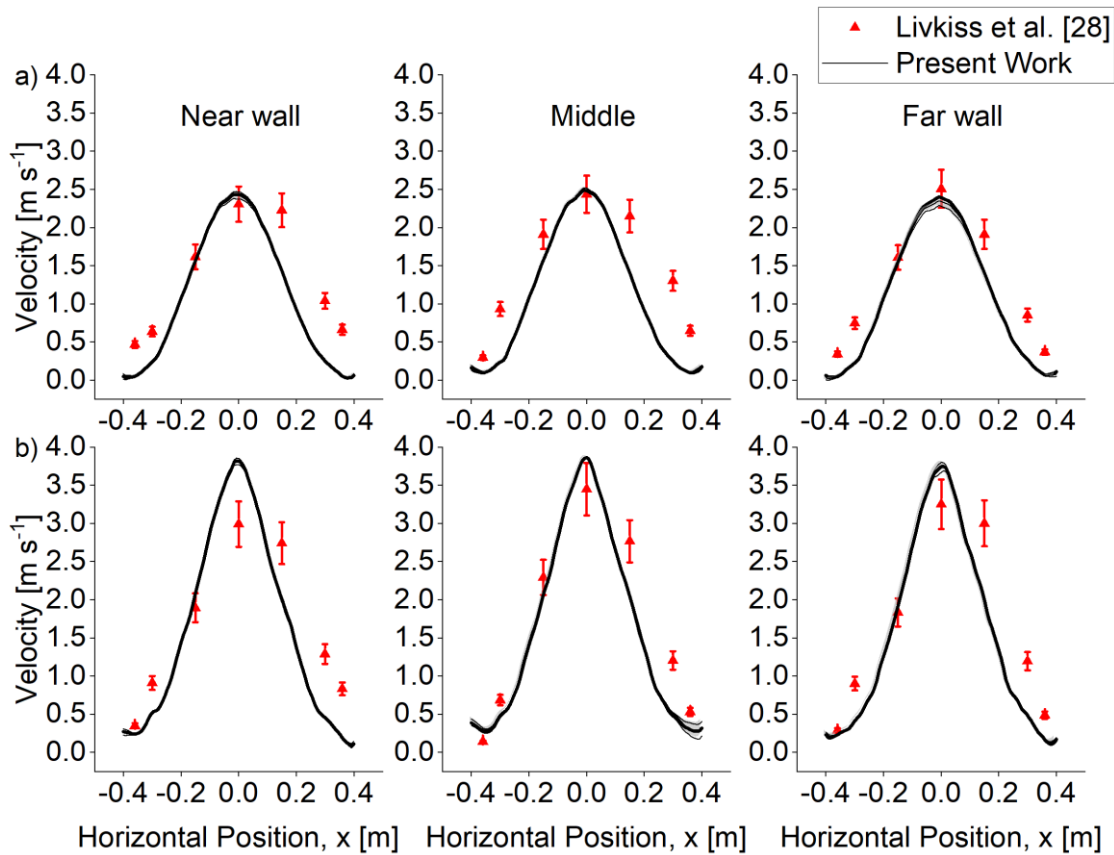


Figure 4.11 Comparison of Scenario 4 result and experimental upward exit velocity data at various locations at the cavity for a cavity width of 40 mm with Burner HRR of a) 6.5 kW and b) 12.9 kW. Although underpredicted, the simulation results capture the general trend of the experimental data.

The model could predict the peak velocity with reasonable accuracy and was found to have an error of around $4\% \pm 10\%$ for HRR 6.5 kW, while for HRR 12.9 kW, the error was found to be between $10\% - 20\% \pm 10\%$. However, the velocity prediction at the side was found to be underpredicted with an average error of 51%, as shown in Table 4.3. These errors were likely due to bi-directional probes not being modelled, causing discrepancies as they may influence the airflow out of the cavity. Given the uncertainty in the measurements and the general trends captured by the model, the model's capability to predict velocity in a facade cavity fire was satisfactory and could be extrapolated to study different scenarios.

Incident Heatflux to the near wall

The comparison of total heat flux along the centreline of the near wall for both 6.5 kW and 12.9 kW HRR with varying cavity widths is shown in Figure 4.12 and Figure 4.13. The heat flux presented in these figures is defined similarly to Livkiss's definition, where it is the sum of convective heat transfer and incident radiation heat flux. The simulation results show a good prediction for HRR 6.5 kW HRR with an average error of $37\% \pm 25\%$. In contrast, for HRR 12.9 kW, the predicted heat flux is less accurate, with an average error of $45\% \pm 25\%$ and a maximum error of $90\% \pm 25\%$. It is worth noting that the predicted heat flux at the 0.05 m height is all overestimated. This is because the chosen combustion model, an infinitely fast chemistry model resulted in most of the fuel combusting at the first grid. Combined with the radiation model used, the radiative heat flux at the lower region is generally overpredicted.

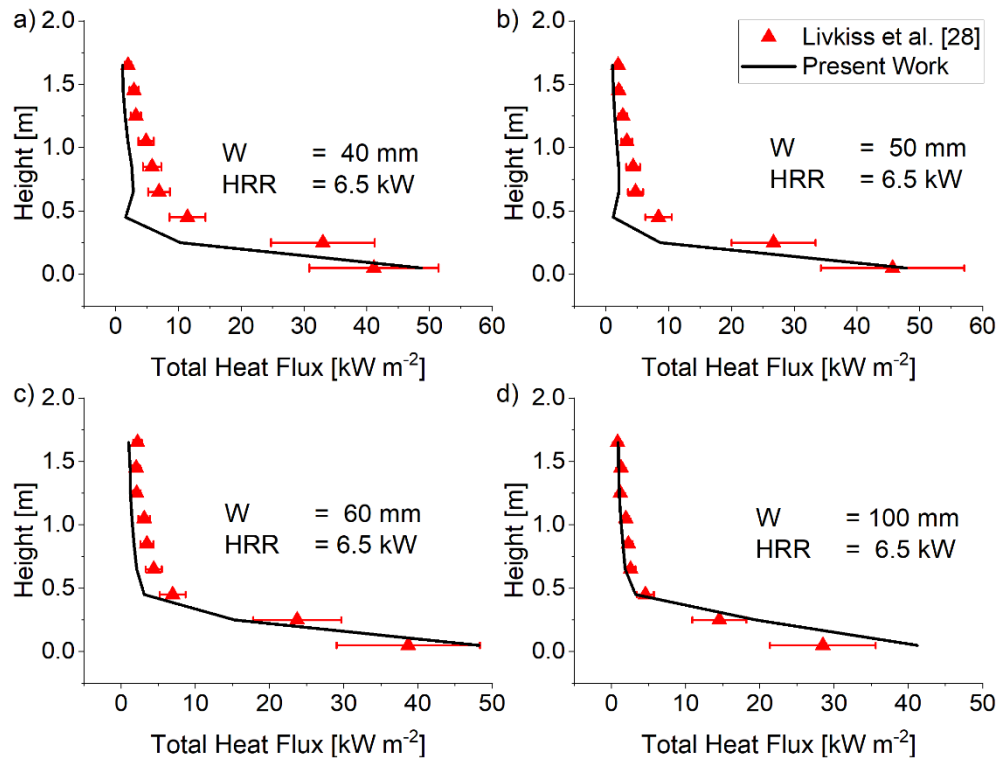


Figure 4.12 Comparison of experimental total heat flux to Scenario 4 prediction of HRR = 6.5 kW for a cavity width of a) 40 mm b) 50 mm c) 60 mm and d) 100 mm. A good match to experimental data was found qualitatively and quantitatively for varying cavity widths.

For cases of burner HRR of 12.9 kW, the simulation could not capture the increasing heat flux from 0.05m to 0.25m. This is because the flame lift-off observed in the experiment for burner HRR of 12.9 kW could not be replicated in the model due to the infinitely fast chemistry combustion model used, which assumes the rate of combustion is governed solely by turbulent or laminar mixing timescale.

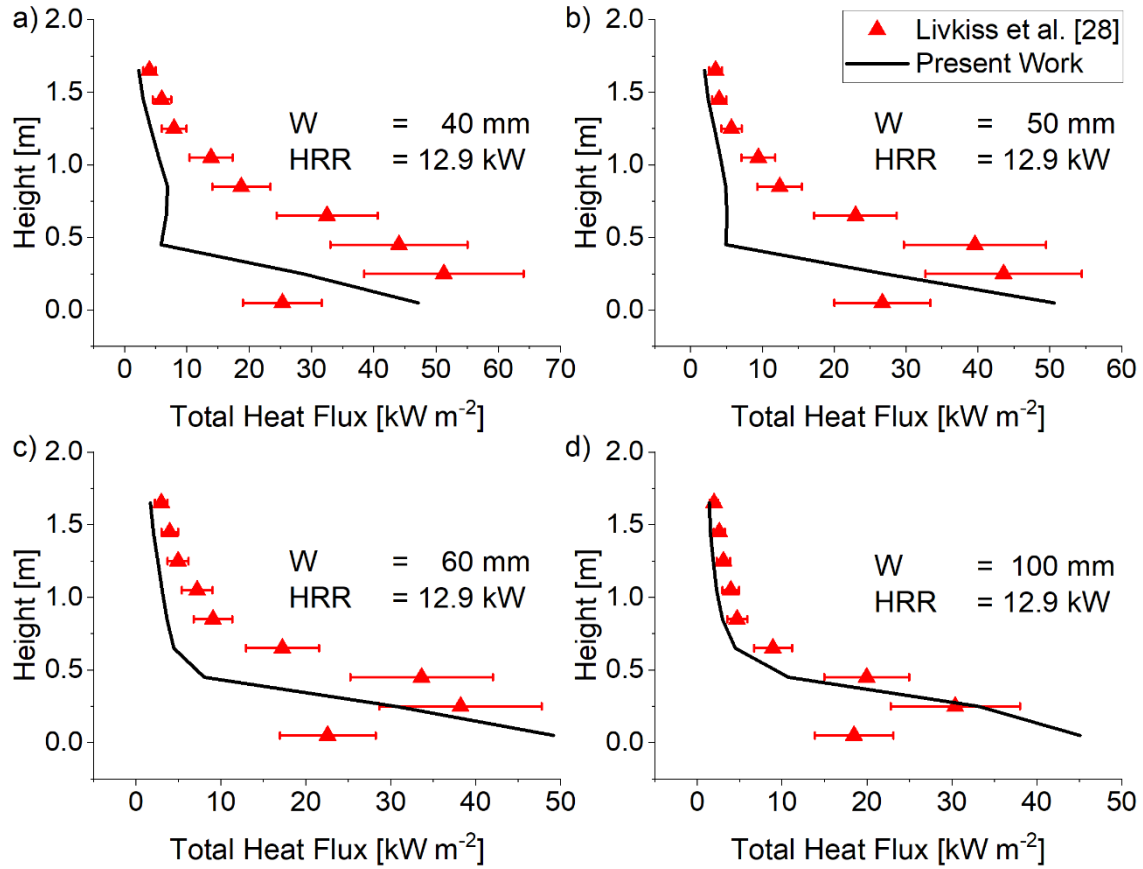


Figure 4.13 Comparison of experimental total heat flux to Scenario 4 prediction of HRR = 12.9 kW for a cavity width of a) 40 mm b) 50 mm c) 60 mm and d) 100 mm. The prediction was found to match the experimental data less at lower elevations.

The error could also be attributed to the model's ability to predict laminar-turbulence transition and convective heat flux in the laminar accurately. Improvement to the accuracy of laminar-turbulence transition and convective heat flux could be made using a finer grid. The analysis found that when using Iso-contour of $Q=1000 \text{ s}^{-1}$ [45] to visualise the inception of turbulence spot for a cavity width of 0.4 m, the turbulence transition was found to occur around $z = 0.5 \text{ m}$ for a grid size of $\Delta y = 2 \text{ mm}$ at the centre of the cavity, as shown in Figure

4.14. When a finer mesh size of $\Delta y = 1$ mm is used, the transition occurs at $z = 0.2$ m, resulting in an increased convective heat flux prediction of the convective heat flux at $0.2 \text{ m} < z < 0.5 \text{ m}$ by up to 60%.

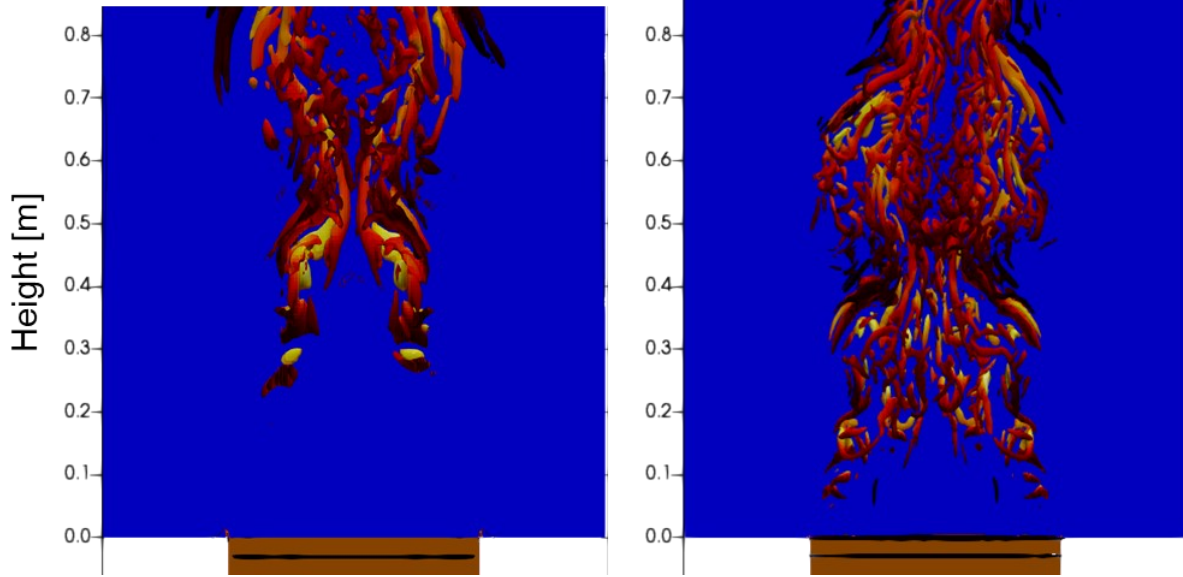


Figure 4.14 Vortical structure of the flame using Iso-contour of Q , $Q=1000 \text{ s}^{-1}$ - based on Ren et al. [45]. (Left) The iso-contour of Q using the Medium mesh shows turbulence inception occurs around 0.45 m. (Right) The iso-contour of Q using the Fine mesh shows turbulence inception occurs around 0.20 m.

Figure 4.15 shows the comparison of the present work with Livkiss's FDS model [49], which calculates convective heat flux using the default FDS wall function. The result shows that the predicted convective heat flux is similar in the turbulent region but differs in the laminar region. The inaccuracy in the predicted convective heat flux at the laminar region was also previously observed by Ren et al. [45].

An accurate prediction of the laminar-turbulent transition point and laminar convective heat flux can be achieved by having a DNS-like grid, however, not pursued in the current setup due to the required computational resources. It is important to note that an accurate prediction of the laminar region may have affected the prediction of vertical fire spread on the facade. However, since the model's objective is to study a cavity's effect on the fire dynamic within the facade, a DNS-like grid was not used. The scenario used to study this will be similar to the facade fire test, where a gas burner is constantly present underneath

the cavity. As such, the size of the laminar region usually is small, and the current model can still be useful in studying scenarios where the fire is predominantly turbulent.

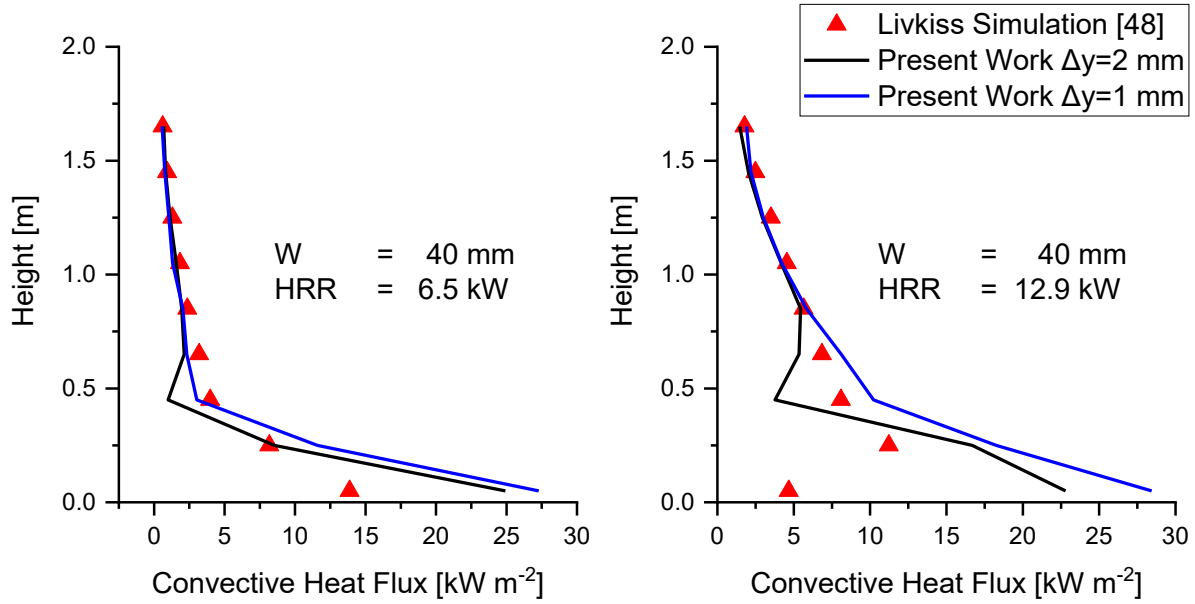


Figure 4.15 Comparison of Convective Heat Flux predicted by different mesh sizes in Scenario 4 and simulation by Livkiss. Results show that a finer grid predicts the laminar convective heat transfer better.

As aforementioned, the accurate prediction of the flame shape may affect the radiation heat flux on the panel. This is because the incident heat transfer is strongly dependent on the flame, which affects both convective and radiation heat transfer next to the wall. As shown in Figure 4.16, the incident heat flux at the centre is higher at lower elevations. As elevation increases, incident heat flux at the centre becomes lower than at the sides due to reduced radiation heat flux as the flame splits away from the. As elevation increases, the centre's heat flux becomes higher again as the radiative heat flux becomes less dominant away from the flame, and air entrainment from the side forces hot air towards the centre. This may explain the underprediction of the flame at the centre compared to the experiment. However, it is essential to note that the shape of the flame is not recorded in the experiment, and further study on the flame shape in a cavity is required.

Lastly, when examining the effect of cavity width, the incident heat flux tends to reduce with cavity width, except for the incident heat flux at the centre of the panel. The simulation results show that radiation and convective heat flux reduce slightly as cavity

width increases. This reduction is likely due to reduced re-radiation from the far wall and reduced air temperature due to more air entrainment into the cavity.

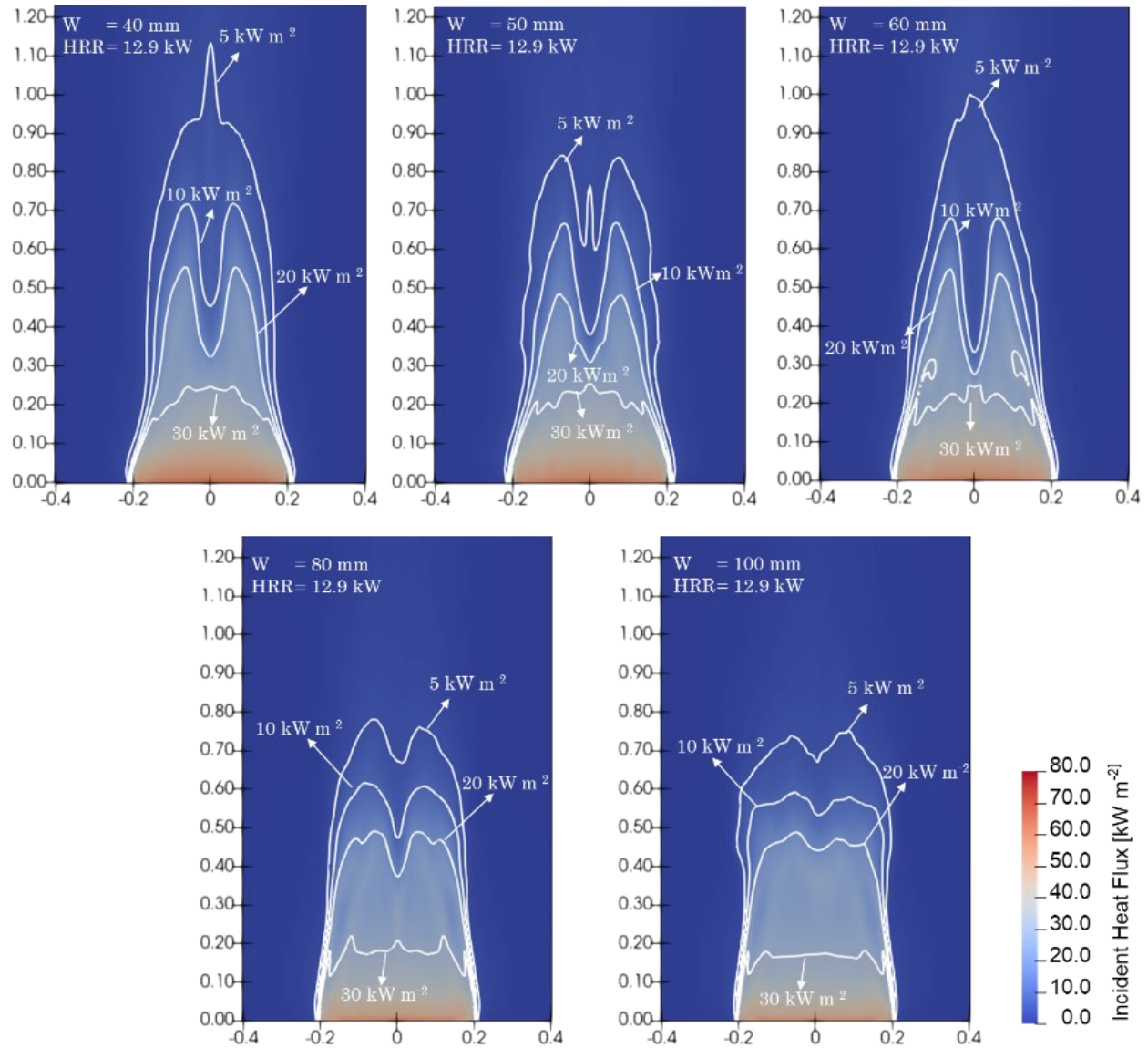


Figure 4.16 Incident heat flux for burner HRR of 12.9 kW at cavity widths of 40 mm, 50 mm, 60 mm, 80 mm and 100 mm. The results show that the height of the incident heat flux contour reduces with cavity width.

Table 4.3 Mean Relative error and bounded relative error for Scenario 4. Good accuracy was measured for flame height and velocity. However, relative errors for heat flux measurements are high.

Cavity width, mm	Flame Height				Velocity				Heat flux			
	6.5 kW		12.9 kW		6.5kW		12.92kW		6.5kW		12.9kW	
	RE^M	RE^b	RE^M	RE^b	RE^M	RE^b	RE^M	RE^b	RE^M	RE^b	RE^M	RE^b
40	14.4	14.3	30.3	29.4	51.2	43.5	39.0	35.1	50.1	44.8	61.5	54.0
	$\pm 11\%$	$\pm 11\%$	$\pm 12\%$	$\pm 12\%$	$\pm 10\%$	$\pm 10\%$	$\pm 10\%$	$\pm 10\%$	$\pm 25\%$	$\pm 25\%$	$\pm 25\%$	$\pm 25\%$
50	9.6	9.6	19.0	18.8	N/A	N/A	N/A	N/A	48.9	44.2	55.5	49.3
	$\pm 12\%$	$\pm 12\%$	$\pm 8\%$	$\pm 8\%$					$\pm 25\%$	$\pm 25\%$	$\pm 25\%$	$\pm 25\%$
60	10.38	10.3%	14.7	14.6	N/A	N/A	N/A	N/A	41.9	38.5	52.7	46.4
	$\pm 13\%$	$\pm 13\%$	$\pm 9\%$	$\pm 9\%$					$\pm 25\%$	$\pm 25\%$	$\pm 25\%$	$\pm 25\%$
80	N/A	N/A	N/A	N/A	N/A	N/A	N/A	N/A	N/A	N/A	N/A	N/A
100	4.7%	4.7%	9.7	9.6	N/A	N/A	N/A	N/A	23.3	22.6	35.7	31.6
	$\pm 15\%$	$\pm 15\%$	$\pm 15\%$	$\pm 15\%$					$\pm 25\%$	$\pm 25\%$	$\pm 25\%$	$\pm 25\%$

4.6 Conclusion

Simulation results from Scenario 4 show that the model successfully captures the general trend of the upward exit velocity and the decreasing flame height with increasing cavity width. The results show that the predicted error for maximum upward velocity for burner HRR of 6.5 kW has an average error of 4.7%, while for burner HRR of 12.9 kW has an average error of 18.1%. However, when comparing the velocity profile, the error becomes more significant, with an average error of 43.5% and 35.1% for HRR of 6.5 kW and 12.9 kW, respectively. These increased errors are likely due to a lack of probes modelling, which affects the predicted flow velocity. As for flame heights, the model was shown to underpredict the flame height consistently with an average error of 14.0%. Another observation from the simulation found that the flame tends to split into two peaks at narrow cavity width. As a result of the split, the radiative heat flux is reduced at the centre of the panel. However, it is unsure if the flame splits at the centre of the panel as the cavity width narrows in the experiment, and further investigation is required to understand if the flame shape is captured accurately.

The simulation results also showed that the model accurately predicts the trend of increasing incident heat flux with decreasing cavity width. This is due to re-radiation from the far wall and increased convective heat due to higher air temperature in the cavity. However, the main challenge in Scenario 4 was the accurate prediction of the incident heat flux due to the HRR from the burner. The results show that the incident heat flux at the near-wall predicted by the model is accurate for burner HRR of 6.5 kW with an average error of $37\% \pm 25\%$. However, for 12.9 kW, the predicted heat flux matches the experimental value less accurately, qualitatively and quantitatively, with a maximum error of up to 90% and an average error of $45\% \pm 25\%$. This is likely due to the inability of the model to simulate flame lift-off. Furthermore, without using a fine mesh which drastically increases the required computational resources, the prediction of convective heat transfer in the lower laminar region results in an average error of 40 %. However, it is worth noting that flame lift-off is an artefact of experiments and is unlikely to occur in real facade fire, and the lower laminar flame region of wall fire is generally small compared to the turbulent flame region, some of which are known issues in the field. For the specific scenario at hand, narrow cavity fire, computational modelling is not abundant, and the current work intends to highlight the complexity of the multiphysics process of narrow cavity fire.

The results show that the current model can predict the general trend of the cavity fire with varying widths. While the model has predicted the heat flux at the laminar region and flame height less accurately, which could affect the flame spread prediction, the model's objective is not to predict flame spread within the facade cavity. The research aims to develop a model capable of studying the fire dynamics within a cavity in a facade fire test configuration. Therefore, while the model requires further development and research, the model is suitable to be extrapolated to study the effect of facade cavity in scenarios where most of the pyrolysis zone is in the turbulent flame zone and the flame is in a well-ventilated condition.

Chapter 5

Effect of cavity barriers inside the Narrow Cavity of a Facade

Summary⁴

Facade configuration often has a significant impact on the airflow within the cavity. This may indirectly affect the heat flux on the facade insulation and cladding, resulting in a more flammable facade system. In this chapter, the model is extrapolated to study the impact of a facade cavity with closed sides to simulate a restricted airflow condition and the effect of having a poorly installed cavity barrier where it is partially closed. Analysis showed that flame height increases by up to 10% when the sides are closed due to increased inlet upward velocity. The results also show an increase in incident heat flux by up to 12 kW m^{-2} or approximately 100% at the lower region of the near wall. For cases where the cavity barrier is partially closed, the simulation suggests that flame heights are generally reduced regardless of the gap between the cavity barrier and the near wall. However, the results show a non-linear relationship between the cavity barrier gap, flame height and incident heat flux. The simulation result shows that despite certain limitations of the model, which were discussed, the results show that facade configuration significantly affects the potential flammability of the facade system.

⁴ This chapter is based on a paper in progress: B. Khoo, W. Jahn, P. Kotsovinos, G. Rein, Effect Of Cavity Barriers inside the Narrow cavity of a Facade.

5.1 Introduction

In the previous chapters, I have performed validations for fluid flow, heat transfer, buoyancy and combustion in a narrow cavity fire scenario. I have shown that the current model can predict the aforementioned physical phenomena with good credibility. In this chapter, I intend to use the current model to study the effect of different facade configurations on fire dynamics. Furthermore, this chapter also intends to understand the limitations of the current model.

As discussed in Chapter 1, facade configuration significantly affects how fire behaves in the cavity. For example, Foley et al. showed that airflow into the cavity significantly affects fire dynamics and heat transfer to the panel [25]. Various studies have also shown that different cavity widths with different facade configurations behave differently due to how air is entrained into the cavity [17–19]. Hence, it is essential to study how different configurations affect facade fire safety. Unfortunately, detailed studies on the effect of cavity width and different facade configurations are sparse due to the high experimental cost. Using CFD to extrapolate different facade configurations may provide some insight to complement experimental studies.

Traditionally, extrapolation is performed using reduced-scale experiments to understand how fires would behave at a larger scale. This is because reduced-scale experiments are often cheaper and require less time to set up the experiment, making it more economical to study fire behaviours. Several modelling techniques were developed to allow a reduced-scale experiment's results to infer large-scale fire behaviours [110]. Unfortunately, preserving multiple physical phenomena at different scales is often tricky as physical phenomena scale differently with increasing fire size, making valid extrapolation difficult.

Using CFD, there is no need to reduce the simulation scale to extrapolate the data, as maintaining large-scale simulations does not increase the cost drastically as experiments would. However, to ensure the CFD results are reliable, practitioners must first validate the numerical methodology with experimental data. This is often done by increasing the model complexity incrementally, generally by introducing the relevant physical phenomena one at a time to the model to limit compensation effects. Once all physical phenomena are

validated, extrapolation can then be performed to study various scenarios to complement experimental studies.

It is important to note that any validated CFD model extrapolated to study different scenarios may introduce errors as it lies outside the validated parameters. However, the potential error introduced by the extrapolation should not deter its use because a robustly validated model would need to explore different scenarios outside its validated parameters to be useful for practitioners.

This chapter intends to extrapolate the validated model to study two different configurations currently scarce in the literature for a narrow cavity fire. First, to study the effect of closing the side of the cavity using a vertical cavity barrier to understand how it affects flame dynamics. Second, how a partially closed horizontal cavity barrier could affect flame dynamics in the cavity. The study also intends to explore any potential error that may be introduced from extrapolating the model.

5.2 Methodology and Numerical Method

As aforementioned, two different cases were studied in this chapter. The first configuration studies how closing the cavity using two vertical cavity barriers on the sides alters the fire dynamic in the cavity. The same non-combustible material for the panel is used to close the cavity's side, as shown in Figure 5.1. The simulations will study five cavity widths of $W = 40, 50, 60, 80,$ and 100 mm, each with two different burner HRRs of 6.5 kW and 12.9 kW. The fire dynamics observed are then compared to the base case results, where the sides are open.

The second configuration studies the effect of a failed cavity barrier, where it is only partially closed, on the fire dynamic in the cavity. A non-combustible barrier is installed at 0.360 m to 0.445 m above the burner for three different cavity widths of $40, 60,$ and 100 mm. Three different cavity barrier gaps are chosen for each cavity width. For example, for the 40 mm cavity width, a gap of $4, 10,$ and 20 mm are chosen; for the 60 mm cavity width, a gap of $4, 6$ and 30 mm are chosen; for the 100 mm cavity width, a gap of $4, 10$ and 50 mm are chosen. Similarly, for each case, two different burner HRRs of 6.5 kW and 12.9 kW are used. The results obtained from the simulation were compared to the base case.

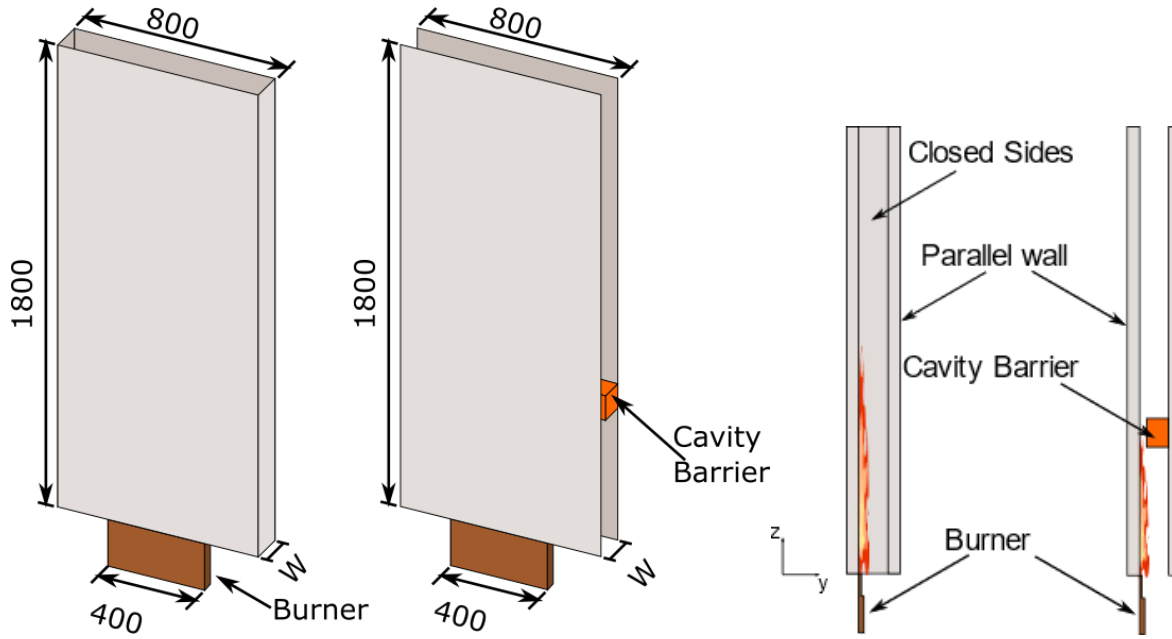


Figure 5.1 The numerical setup for the cavity with a closed side and the cavity barrier case. For cavities with closed sides, cavity widths of 40, 50, 60, 80, and 100 mm are studied. As for the cavity barrier case, a cavity width of 40, 60 and 100 mm was studied with three different gaps between the panel and the cavity barrier.

The numerical settings used are the same as those described in Section 3.4 and Section 4.3, and readers are referred to those sections for a detailed description.

5.3 Computational Domain and Boundary Conditions

The computational domain of the extrapolated cases is similar to those performed in Chapter 4. The only difference in the computational domain is the presence of both closed sides and the cavity barrier. The grid setup and numerical cell are similar to those described in Chapter 4 for the corresponding cavity width, where the total gas-phase numerical cell range between 860,000 and 1,600,000 and the total solid-phase cells is approximately 7,000,000. In this chapter, the boundary condition and materials used are the same as those described in Chapter 4, and the burner HRR investigated are 6.5 kW and 12.9 kW. Table 5.1 summarises all the cases investigated in this chapter for both closed sides cavity cases and cavity barrier cases.

Table 5.1 Description of the cases investigated in the CFD analysis.

Cases	Cavity Width, W [mm]	Side Sealed?	Gap between barrier [mm]	Burner HRR [kW]
C01	40	Yes	N/A	6.5
C02	40	Yes	N/A	12.9
C03	50	Yes	N/A	6.5
C04	50	Yes	N/A	12.9
C05	60	Yes	N/A	6.5
C06	60	Yes	N/A	12.9
C07	80	Yes	N/A	6.5
C08	80	Yes	N/A	12.9
C09	100	Yes	N/A	6.5
C10	100	Yes	N/A	12.9
B01	40	No	4	6.5
B02	40	No	10	6.5
B03	40	No	20	6.5
B04	40	No	4	12.9
B05	40	No	10	12.9
B06	40	No	20	12.9
B07	60	No	4	6.5
B08	60	No	6	6.5
B09	60	No	30	6.5
B10	60	No	4	12.9
B11	60	No	6	12.9
B12	60	No	30	12.9
B13	100	No	4	6.5
B14	100	No	10	6.5
B15	100	No	50	6.5

Cases	Cavity Width, W [mm]	Side Sealed?	Gap between barrier [mm]	Burner HRR [kW]
B16	100	No	4	12.9
B17	100	No	10	12.9
B18	100	No	50	12.9

5.4 Results

The discussion of results is separated into two sections, simulation with closed sides and simulation with cavity barriers. The effect of closed sides or cavity barriers will be analysed in each section, and the impact of varying cavity widths is also discussed.

Closed Side

Flame Height and Flame Shape

Results show that the predicted flame height for cavities with closed sides is 1% - 10% higher than cavities with open sides, as shown in Figure 5.2. The increase in flame height is expected as the air entrainment into the cavity increases when the sides are closed, resulting in a taller flame. For example, when comparing cases for a cavity width of 40 mm at a HRR of 12.9 kW, the maximum inlet velocity at the centre of the cavity is two times higher for closed sides than for open sides.

However, Case C05, C07 and C10 are an exception to the trend, where the average flame height for cavities with closed sides is slightly lower than the open side but with a higher measured maximum flame height. This is because the flame predicted by the model was not symmetrical, as shown in Figure 5.3. The reason for the flame to be asymmetrical is likely due to the small computational domain. As shown in Figure 5.4, when the sides are open, the air entrainment from the side forces the flame towards the centre, making the flame symmetrical. However, when the sides are closed, flame symmetry becomes strongly dependent on the flow at the inlet and outlet of the cavity. As a result, a much larger - computational domain is likely required, especially near the outlet, to ensure flame symmetry in the cavity. Achieving this requires significant computational resources and will therefore be investigated in future work. However, since the flames are only minimally

off-centre, the simulation results are still used to understand the potential effect of a cavity with closed sides.

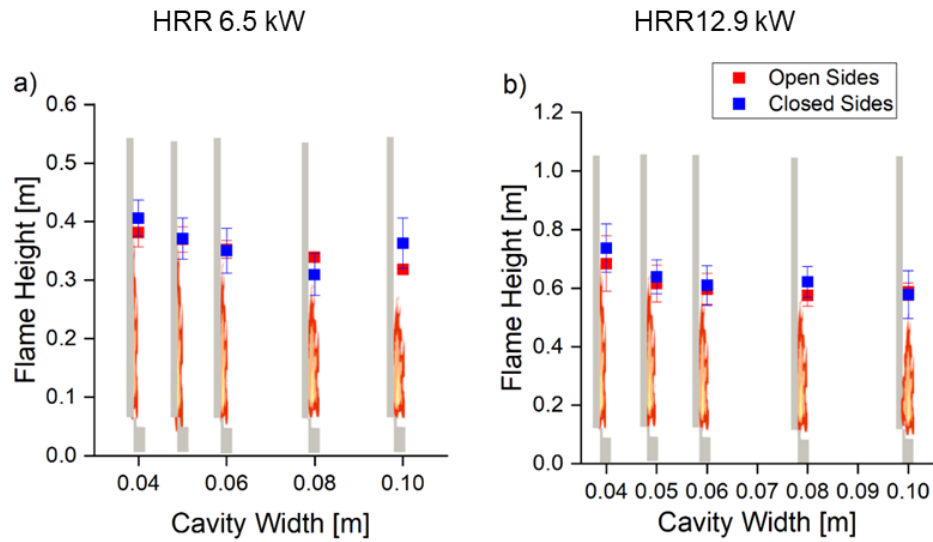


Figure 5.2 Flame height for closed sides is generally higher than for open sides. One reason for this increase is due to increased air entrainment velocity.

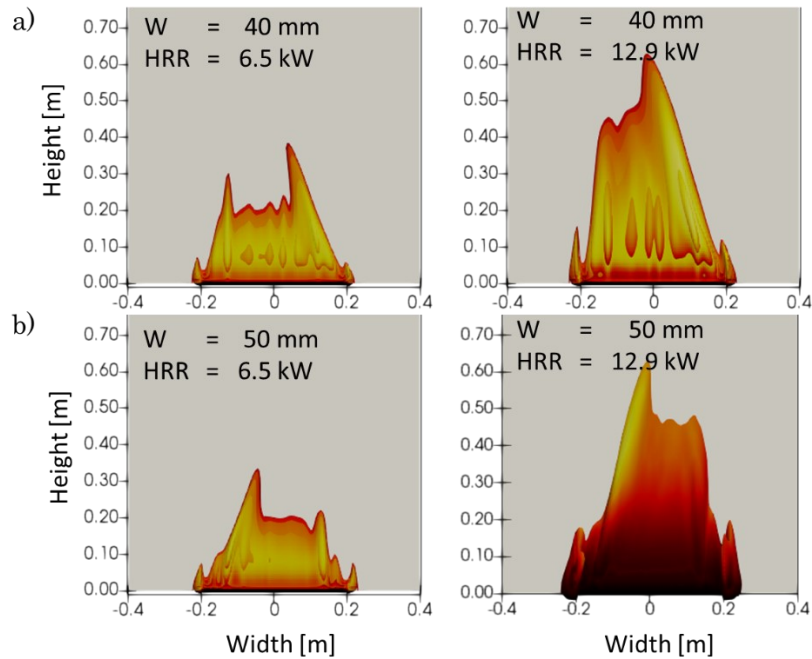


Figure 5.3 Continuous flame shape using stoichiometric mixture fraction for a closed side with a cavity width of a) 40 mm and b) 50 mm for HRR 6.5 kW (Left) and 12.9 kW (Right). The simulation results show that when the sides are closed flame is asymmetrical.

Lastly, regarding the shape of the flame, flame splitting is not observed in all cavity widths and burner HRR. This is because the closed sides prevent air entrainment from the sides, which could create circulation at the centre that forces the fuel away from the centre, creating flame peaks.

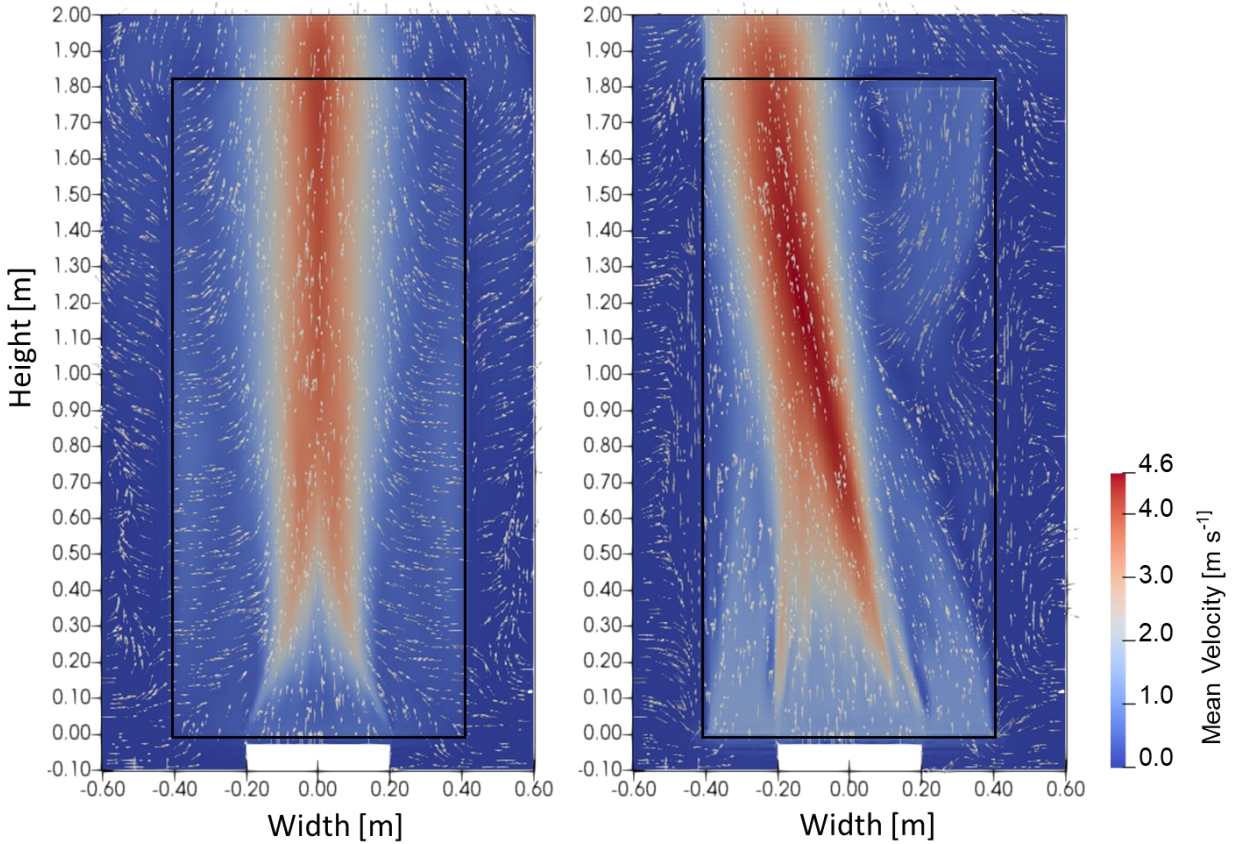


Figure 5.4 Time-average airflow in open-sided (left) and closed-sided (right) scenarios. Flames are symmetrical in an open-sided cavity, but not when the sides are closed.

Heat Flux

The comparison of incident heat flux between open and closed sides shows that the predicted incident heat flux on the near wall for both HRR of 6.5 kW and 12.9 kW are slightly higher for cases where cavity width is below 60 mm, as shown in Figure 5.5.

For burner HRR of 6.5 kW, the heat flux difference between the open and closed sides is insignificant. While for cavities under 60 mm, all simulation shows an increase in incident heat flux of around 5 kWm^{-2} , especially from 0.25 m above the burner. This increase is

likely due to the difference in flame shape, where the flame did not split at the centre. As a result, the radiative heat flux and convective heat flux are greater at the panel centre. However, as the continuous flame height for HRR of 6.5 kW is generally below 0.20 m, the difference in incident heat flux between open and closed sides is limited.

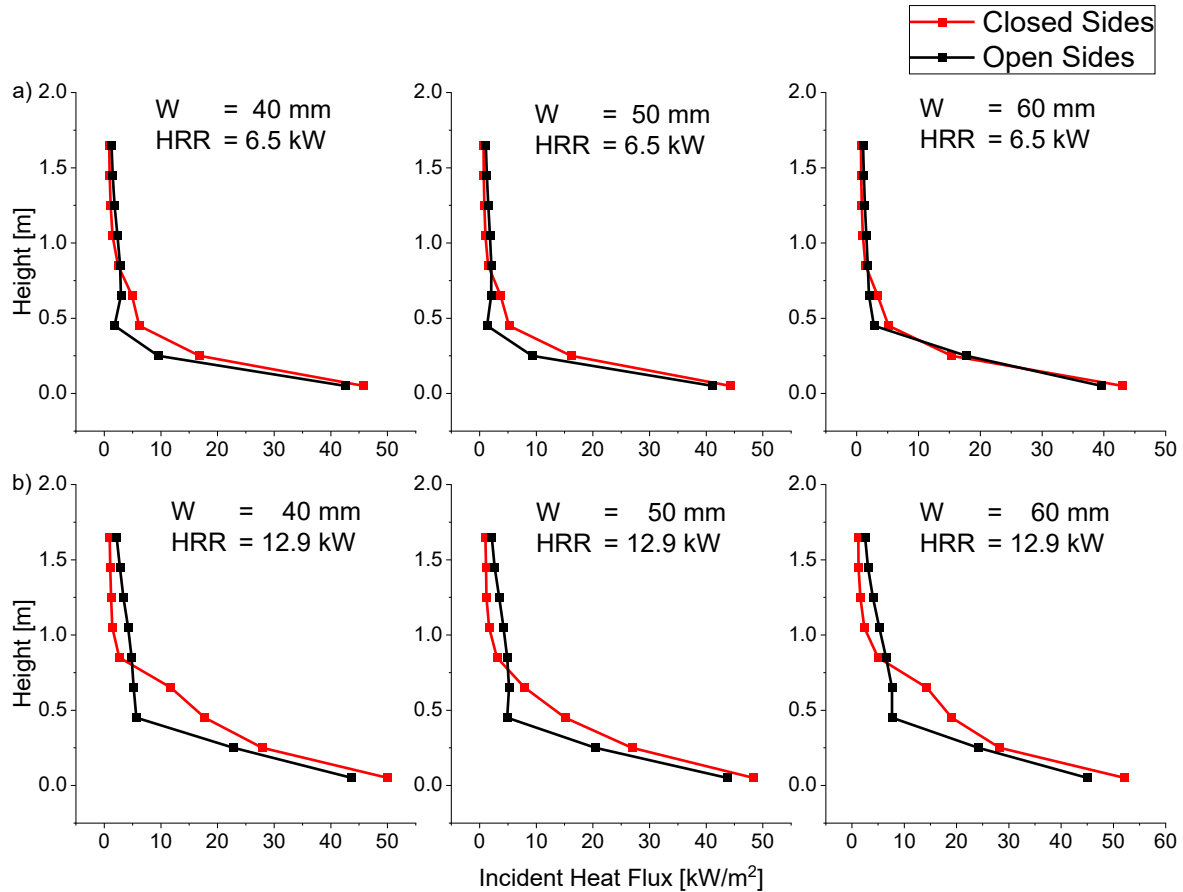


Figure 5.5 a) 6.5 kW HRR, b) 12.9 kW HRR, at cavity width smaller than 60 mm, the incident heat flux was observed to have increased

As for the HRR 12.9 kW case, the results show a more significant difference between open and closed sides for cavity widths of below 60 mm. Similar to the HRR 6.5 kW case, incident heat flux increases from 0.25 m above the burner. However, the difference between the two HRRs is that the incident heat flux increase for HRR 12.9 kW is much higher than HRR 6.5 kW, especially at a higher height, with an increase of between 5 kW m^{-2} – 12 kW m^{-2} . This increase is due to the increased HRR that resulted in a higher continuous flame height of around 0.45 m, increasing radiative and convective heat transfer.

However, for a cavity width of 80 mm and 100 mm, both 6.5 kW and 12.9 kW HRR predicted the closed side incident heat flux at the centre line to be similar to those with open sides. As shown in Figure 5.6, the difference between the predicted incident heat flux for both 80 mm and 100 mm cavity width for both open and closed sides is generally within 3 kW m^{-2} . The indifference is likely because at 80 mm and 100 mm cavity widths, the flames in the open cavity widths are no longer split, resulting in a minimal difference in heat transfer at the centre. However, it is important to note that while the incident heat flux at the centre line is similar, the shape of the heat flux contour is different, as shown in the next section.

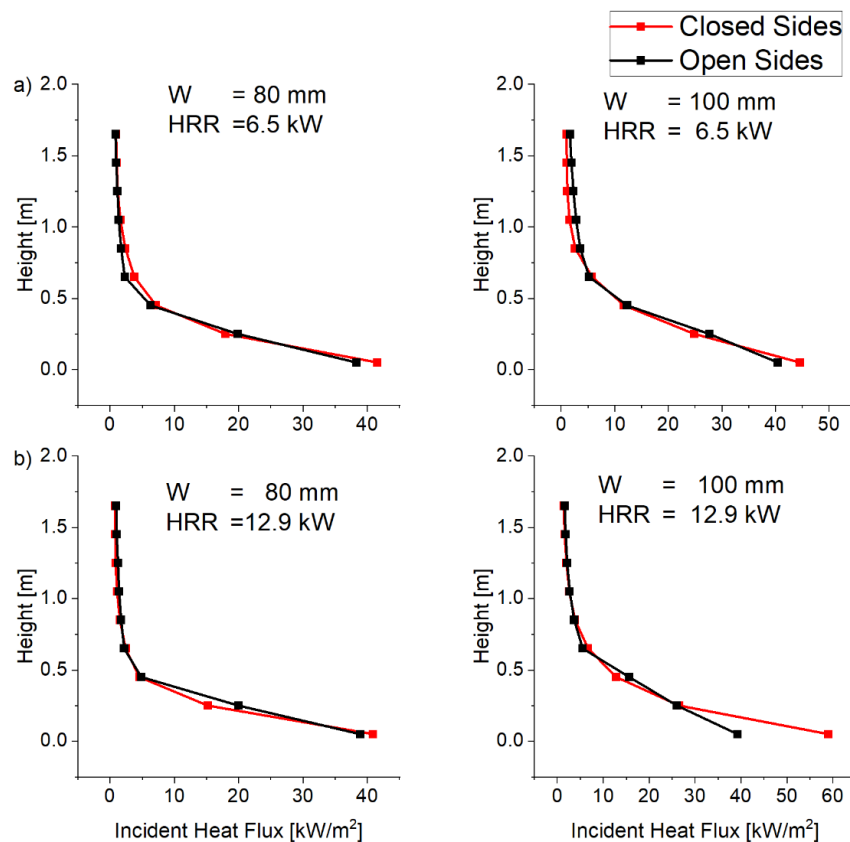


Figure 5.6 a) 6.5 kW HRR, b) 12.9 kW HRR, at a wider cavity width, the increase in the incident heat flux was insignificant. This is likely due to the reduced chimney effect.

To demonstrate how closing the cavity sides affect incident heat flux on the near wall, the contour of the incident heat flux for the cavity width of 40 mm and 100 mm is produced for both burner HRR 6.5 and 12.9 kW, as shown in Figure 5.7 and Figure 5.8. As mentioned

previously, the incident heat flux predicted for cavities with a closed side is not symmetrical due to the size of the computational domain. However, as the tilt is not severe, it is believed that the simulation results could still be used to understand the effect of closed cavity sides.

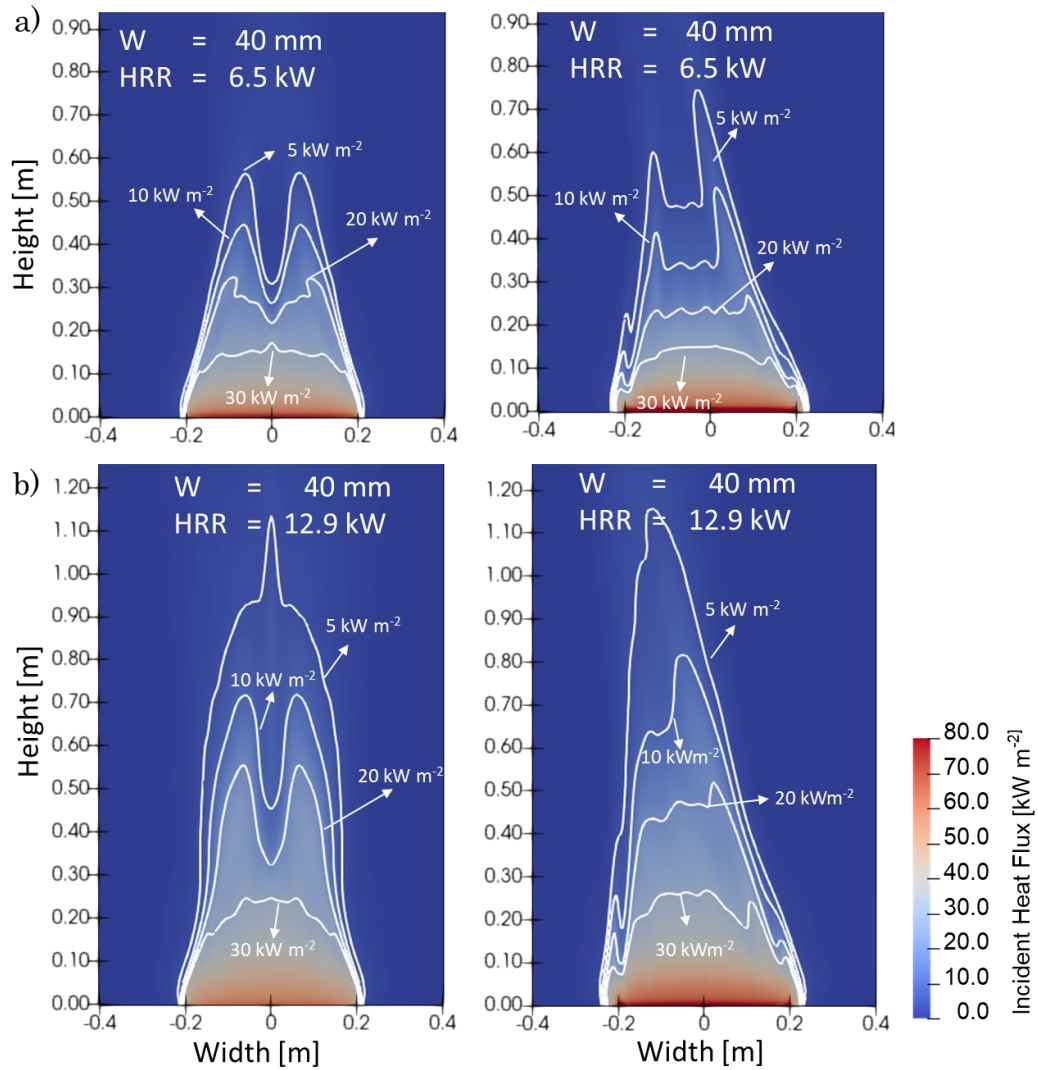


Figure 5.7 Incident heat flux contour for 40 mm cavity width at a)HRR 6.5 kW and b) HRR 12.9 kW. The left image represents a cavity with open sides, while the right image represents a cavity with closed sides.

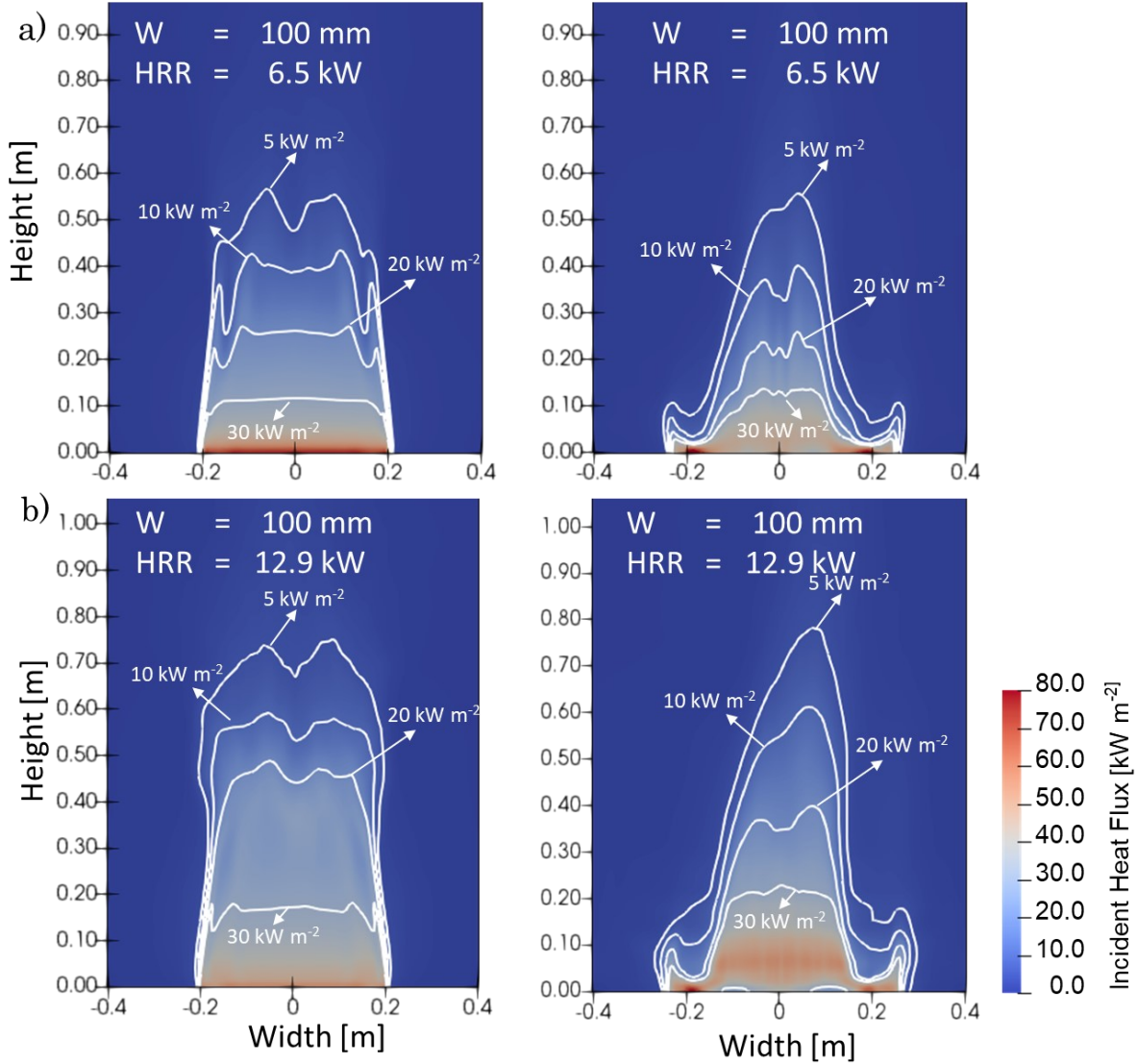


Figure 5.8 Incident heat flux contour for 100 mm cavity width at a)HRR 6.5 kW and b) HRR 12.9 kW. The left image represents a cavity with open sides, while the right image represents a cavity with closed sides.

For a cavity width of 40 mm, the simulation results show that the incident heat flux is slightly wider for the closed cavity case for both burner HRRs, as shown in Figure 5.7. This is due to no air entrainment from the sides that would ‘push’ the flame towards the centre resulting in the fuel flow spanwise. As a result, the contour height of incident heat flux above 20 kW m^{-2} for the closed side cavity case is around 10% - 30% lower than the open side cavity case as they are more spread towards the side. However, as there is no flow circulation at the centre of the cavity, there is no drop in incident heat flux at the centre,

unlike in cases with open sides. For incident heat flux below 10 kW m^{-2} , it was found that the contour heights are generally higher for the closed flame scenarios. This is likely because convective heat transfer is more dominant at these heights due to the lack of continuous flame, and the higher upward velocity achieved by closing the cavity sides increases the convective heat transfer.

For a cavity width of 100 mm, as both open and closed cavity sides do not exhibit split flames, both simulations do not show a drop in incident heat flux at the centre of the near wall, as shown in Figure 5.8. Similar observations were made for a cavity with a closed side where no air entrainment from the side resulted in a wider flame. However, one key difference between the 40 mm and 100 mm cavity widths for both open and closed cavity sides is that the heights of the incident heat flux contour are similar for open and closed cavity sides. One plausible explanation for this is that the increased cavity width has reduced the chimney effect, so the contour height difference is minimal. However, it is important to note that the difference in air entrainment still affects the shape of the incident heat flux, as shown in Figure 5.8.

Cavity Barrier

Flame Height

The simulations found that installing a failed cavity barrier reduces flame height by up to 20% regardless of the gap between the cavity barrier and burner HRR, even for cases where flame height is lower than the cavity barrier position, as shown in Figure 5.9. Case B17 is the only exception where the flame height is higher than the base case.

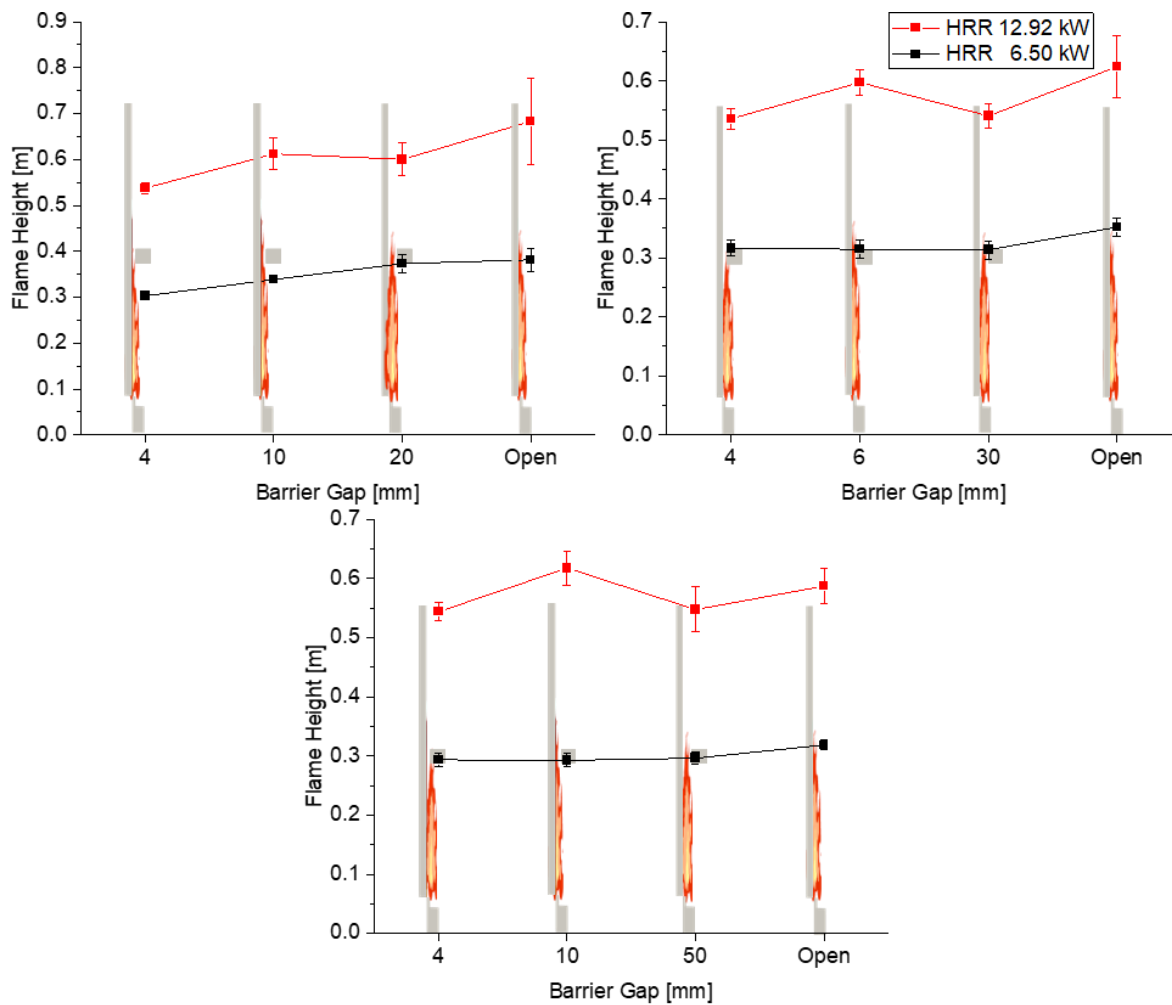


Figure 5.9 Cavity width of (clockwise from top left) 40mm, 60mm and 100mm. Flame height was observed to reduce with the presence of a cavity barrier generally

A cross-section view of the cavity is produced to understand how the cavity barrier reduces the flame height for flames below the barrier. Figure 5.10 demonstrates that a

cavity barrier affects the airflow within the cavity. This created air circulation near the barrier, affecting fuel flow and flame height. The effect of this air circulation near the barrier is more noticeable in a narrower cavity where flame heights are more suppressed. For example, for HRR of 6.5 kW, at a 40 mm cavity width, the flame height is reduced by a maximum of 20%, while for a 100 mm cavity, it is reduced by only 7%. This is likely due to two reasons: 1) the flame is closer to the cavity barrier and therefore affected more by this flow, and 2) presence of a cavity barrier in a narrower cavity affects the flow more than a wider cavity.

For cases where flames would have been higher than the cavity barrier, the results found that the predicted flame heights would first increase as the gap increased before reducing again. It is believed that three factors affect flame height in these cases: 1) flow being choked due to the small gap, 2) chimney effect due to the gap between the barrier and the near wall, and 3) the aforementioned air circulation introduced by the cavity barrier. At a 4 mm gap, although the chimney effect is at its greatest, the gap is too small, resulting in the flow being choked. Therefore, the predicted flame height is predicted to be at its lowest. As this gap increases, the chimney effect becomes smaller, but the gap becomes wide enough for the fuel to pass through, resulting in a taller flame height. As this gap continues to increase, the chimney effects become smaller, and hence the flame height continues to decrease. The flame would finally increase again as the effect of the cavity barrier on the air circulation becomes less significant.

It is important to note that the lower predicted flame height due to the failed barrier does not suggest that a partially blocked cavity is fire safe. The partially closed cavity barrier may increase heat transfer to the panel below the barrier without preventing flame spread. In the next section, the effect of the cavity barrier on incident heat flux will be studied.

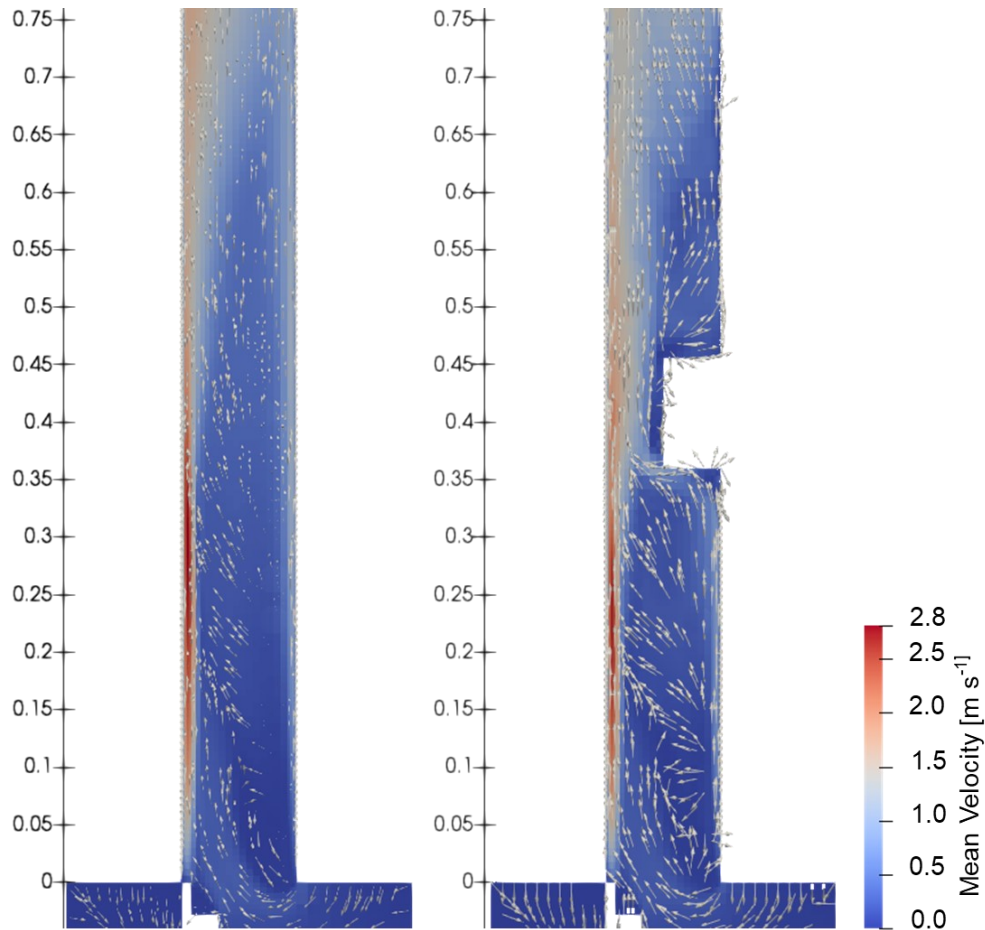


Figure 5.10 Airflow within the cavity is choked due to the presence of the cavity barrier. Flow circulation is observed near the cavity barrier, which affects the flame height even if it is below the barrier.

Heat flux

For heat flux prediction, the simulation found that the cavity barrier increases the heat flux on the panel below the cavity barrier while reducing the heat flux above the cavity barrier for all cases, as shown in Figure 5.11. The increased incident heat flux below the cavity barrier was due to more fuel being combusted under the barrier. The simulation results show that when the gaps are small enough to choke the flow, the incident heat flux above the cavity barrier is consistently the lowest. This is expected as fuel flowing above the barrier is severely restricted. Conversely, as the cavity gap increases, the incident heat flux above the barrier increases as more fuel could combust above the barrier. Interestingly, the observed flame height in a partially closed cavity does not correspond to a higher incident heat flux above the cavity barrier.

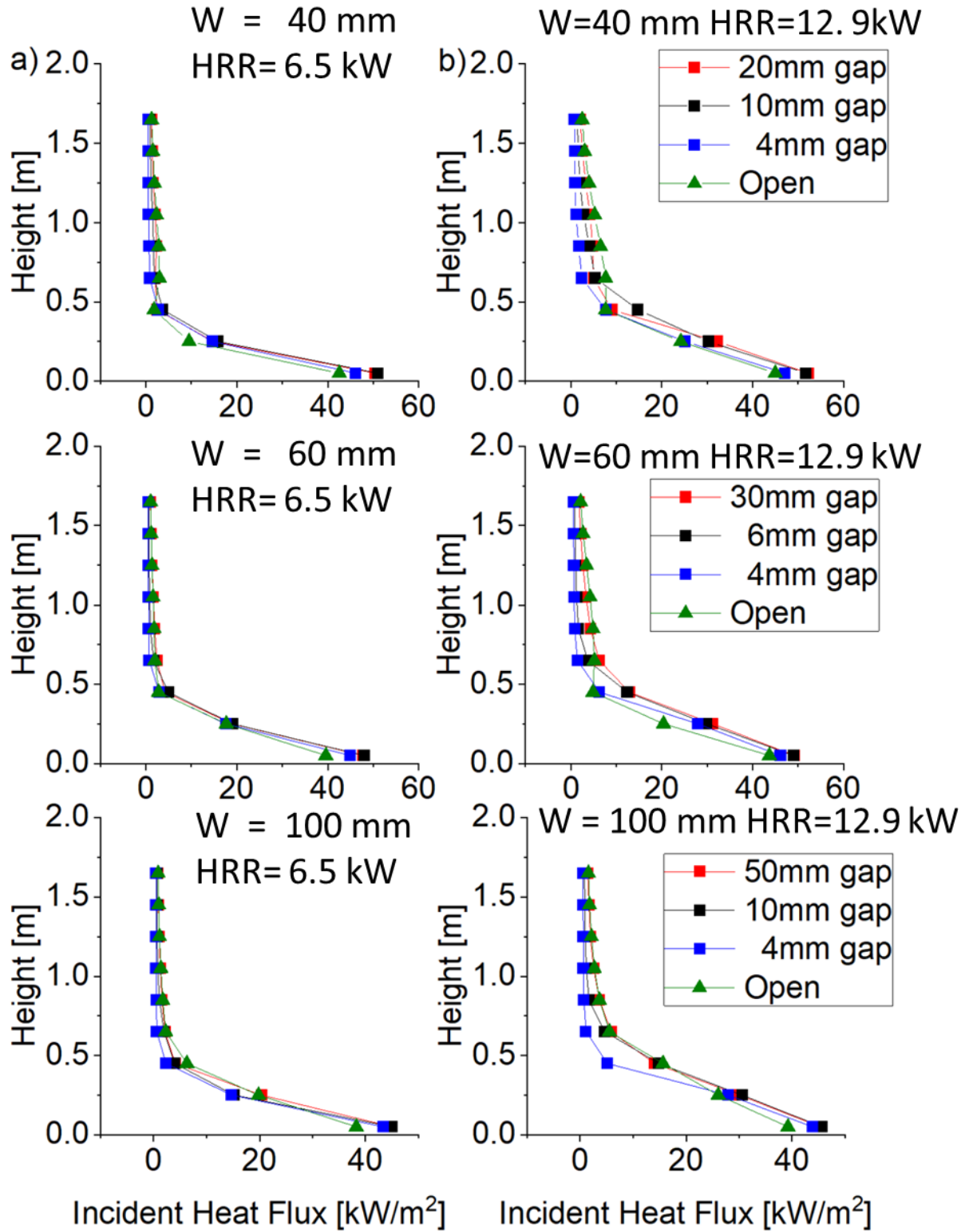


Figure 5.11 Incident Heat flux measured at the centre of the rear wall. From top to bottom, the cavity widths are 40, 60, and 100 mm. Column (a) represents HRR 6.5 kW, and column (b) represents HRR 12.9 kW.

Figure 5.12 shows the effect of the cavity barrier on the incident heat flux of the near wall for HRR 12.9 kW for a cavity width of 40 mm. The results show that the incident heat flux on the near wall is most severe at the 10 mm cavity barrier gap, where the height of the 30 kW m⁻² incident heat flux contour is higher compared to other cases. While the result found that the height of the 5 kW m⁻² incident heat flux contour is lower when the gap is wider, the simulation shows that higher incident heat flux is measured below the cavity barrier. The simulation also showed that the affected area is wider as the fuel that could not pass through the barrier gap spread spanwise.

The increase in incident heat flux due to the cavity barrier is likely due to two reasons: 1) the close distance between the cavity barrier to the near wall increases re-radiation as the gap reduces, 2) more fuel was combusted below the cavity barrier as the gap reduced, resulting in a higher incident heat flux. However, it is important to note that the relationship between the increased incident heat flux and the decrease in cavity gap is not linear. As the gap becomes small enough to choke the flow, the height where the incident heat flux is above 30 kW m⁻² becomes lower, as shown in Figure 5.12 (d). This has increased incident heat flux below the cavity barrier but significantly reduced the heat flux above the cavity barrier, where the maximum heat flux is below 10 kW m⁻².

Figure 5.13 investigates the effect of the cavity barrier for cases where the flame height is below the height of the cavity barrier. The simulation shows that the presence of a cavity barrier has little effect on where the incident heat flux is above 20 kW m⁻² on the near wall. This is expected as the flames were below the cavity barrier, resulting in a negligible re-radiation from the cavity barrier. However, because cavity barriers still affect the flow within the cavity, the convective heat flux on the near wall would still be affected. This is observed in Figure 5.13 (b) and (c), where the incident heat flux below 10 kW m⁻² changes drastically as the cavity gap reduces to below 10 mm.

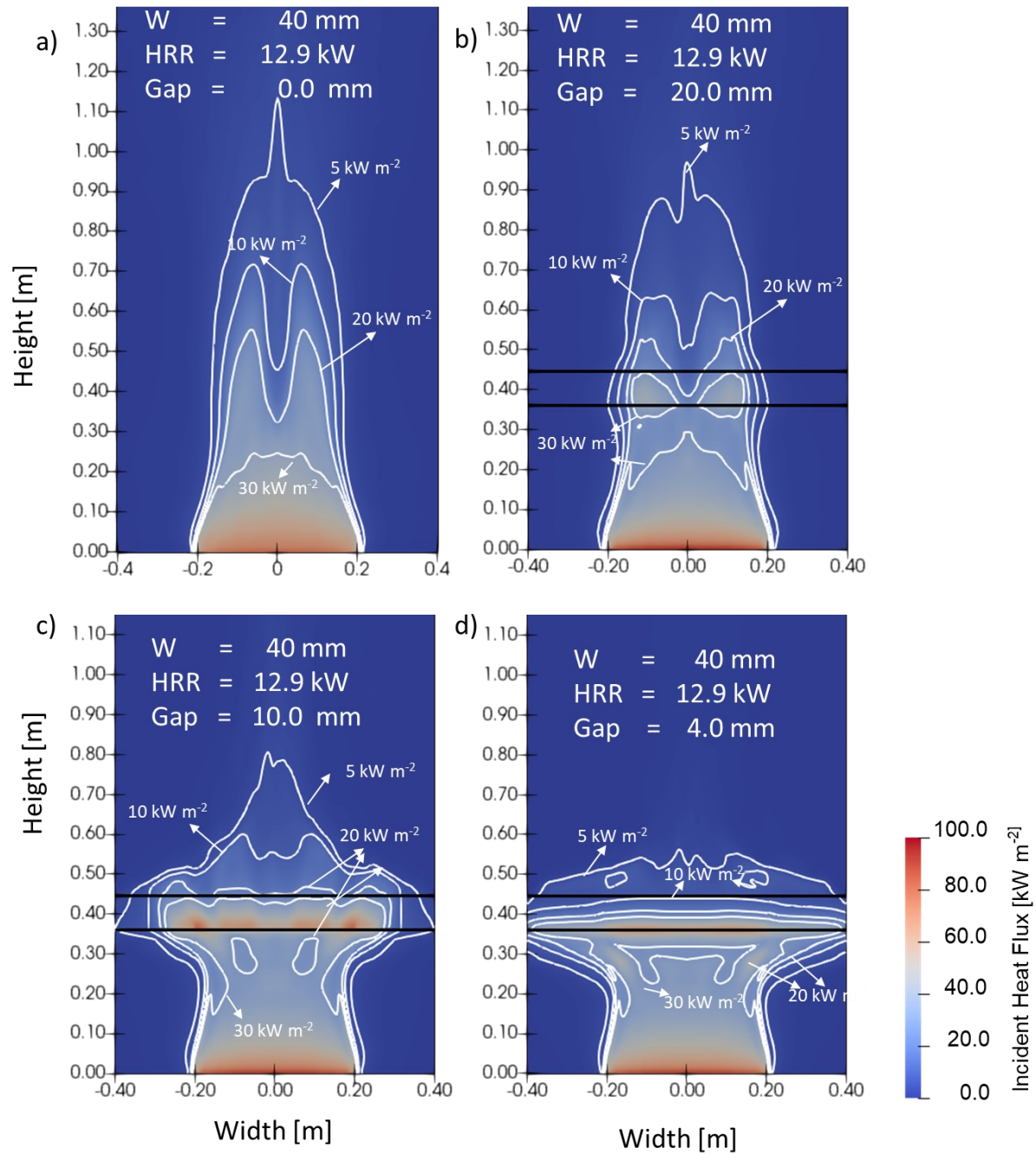


Figure 5.12 Incident heat flux contour for 40 mm cavity width with various cavity barrier gaps at HRR 12.9 kW, a) Open, b) 20 mm, c) 10 mm, d) 4mm. The two black lines across the near wall represent the location of the cavity barrier.

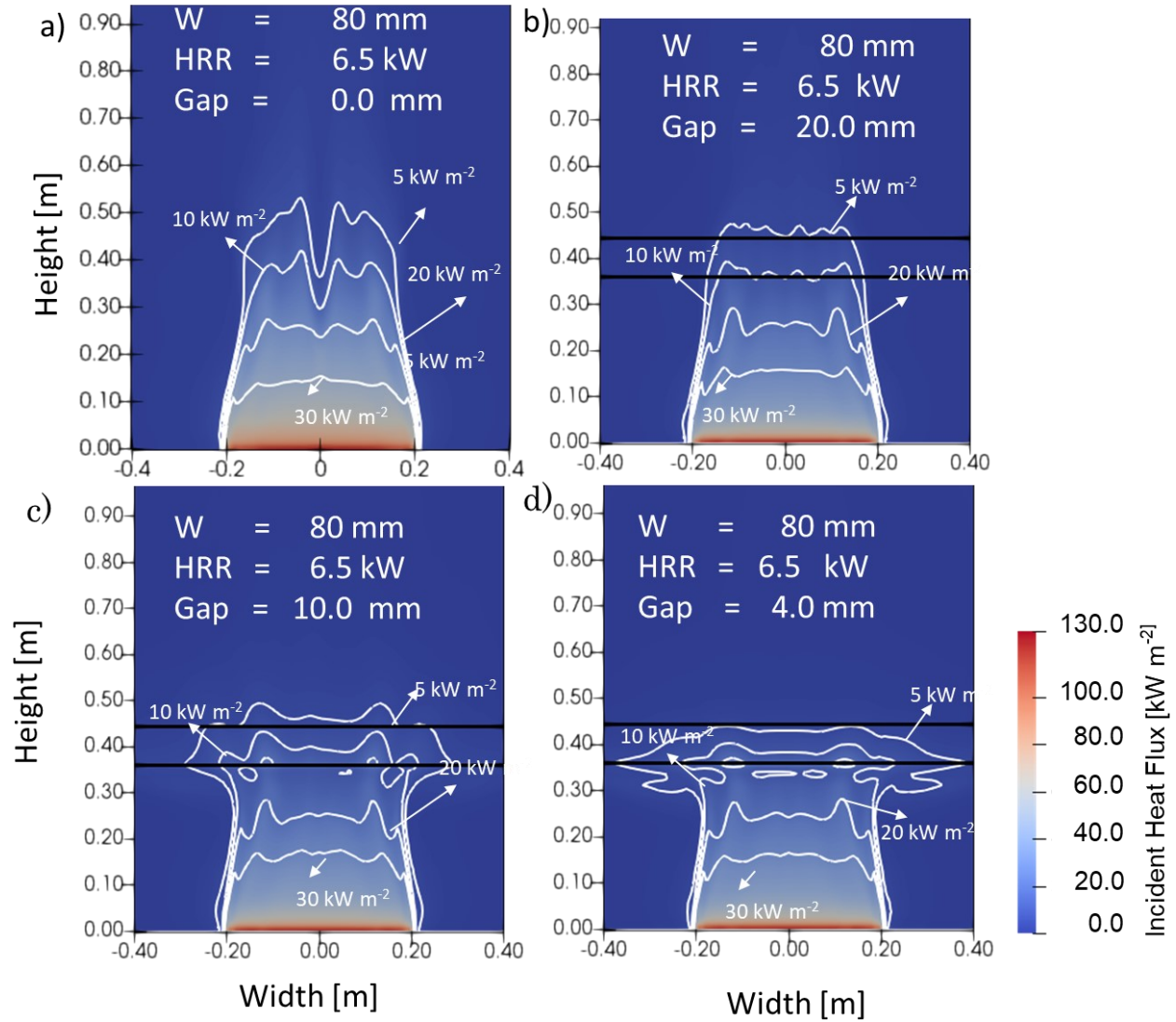


Figure 5.13 Incident heat flux contour for 60 mm cavity width with various cavity barrier gaps at HRR 6.5 kW, a) Open, b) 30 mm, c) 6 mm, d) 4mm. The two black lines across the near wall represent the location of the cavity barrier.

5.5 Conclusion

The validated model for fluid flow, heat transfer, buoyancy, and combustion was used to study two cases where the cavity gap is closed and the effect of a partially open cavity barrier. For the closed sides cases, the model struggled to predict flame symmetry in the cavity due to the size of the computational domain. The reason for this was that the closed sides prevented air entrainment from the sides that would ‘push’ the flame into symmetry.

As a result, an accurate prediction at the cavity outlet is likely required to predict flame symmetry. However, the computational resources required for this is high, and since the asymmetry of the flame is minimal, the simulation result obtained for the closed side cases is still used to understand the general trend in the case of a closed side. It should be noted that future work on the required computational is required.

In general, flame heights within closed sides cases are predicted to be higher than those in the open-side cases by up to 10% due to an increase in upward inlet velocity. As for the predicted heat flux, the simulation found that the heat flux affects a wider area as no air is entrained from the side to force the flame towards the centre. The simulation also found that for cavity width below 60 mm, there is generally an increase in incident heat flux on the near wall below the height of 0.65 m. This increase in heat flux is due to the change in flame shape, where it is no longer split at the centre due to the altered airflow caused by closing the side. For cavity width above 80 mm, the simulation found little difference in the predicted incident heat flux at the centre. However, it is important to note that closing the side of the cavity still affects the contour shape of the incident heat flux as a result of different flame shapes within the cavity.

As for the effect of a partially closed cavity barrier, the simulation result shows that flame height was generally independent of the cavity barrier gap if the base flame height was below the cavity barrier. Results show that the flame height is affected by three factors, 1) increased chimney effect due to the gap, 2) flow being choked by the decreasing gap, and 3) altered airflow due to the cavity barrier. The simulation found that the changes in airflow due to the cavity barrier affect fuel flow and, therefore, the flame height. As the cavity gap reduces, the flame height was found to reduce until the chimney effect becomes significant, where flame height starts to increase. However, as the gap decreases, the flow is eventually choked, and the flame height reduces again. For the predicted incident heat flux, the results show that the cavity barrier significantly reduces incident heat flux above the cavity barrier as the cavity gap reduces. At the bottom of the cavity barrier, it was found that incident heat flux increased due to more fuel combusted under the cavity barrier. The simulation also found that the incident heat flux contour on the near wall is wider as the fuel spreads towards the side due to flow restriction caused by the cavity

barrier. The model found that the incident heat flux is most severe when the cavity barrier gap allows the greatest re-radiation without choking the airflow.

The simulation results show that simply changing the facade configuration has a huge impact on the potential flammability of the facade system. However, to understand the flammability of the facade system, one of the key materials, insulation, needs to be modelled. This will require pyrolysis modelling in a narrow cavity, which will be explored in the next chapter.

Chapter 6

Addition of Pyrolysis Model inside the Narrow Cavity of a Flammable Facade

Summary⁵

Combustible insulation in a narrow cavity of a facade could potentially increase the flammability of the overall facade system. Currently, understanding how combustible insulation affects the flammability of a facade is limited, and CFD fire modelling may be an excellent tool to help understand this effect. This chapter represents the first step towards including a pyrolysis model in the CFD model to study fire inside a narrow cavity of a combustible facade. The simulation result shows that pyrolysis kinetics may be an essential factor in the accurate prediction of HRR in the cavity, where different PIR formulations could result in a difference in prediction by around 30%. The simulation results also show that the current pyrolysis model cannot predict the fire dynamics within the cavity of a combustible facade system as it lacks the capability to predict char oxidation and cracking. This results in the pyrolysis rate bottlenecking after a threshold heat flux, regardless of the increased heat of combustion of the insulant. Simulation results also found that if the boundary layer between the gap at the cladding junction is not resolved, the temperature within the cavity at 0.5 m height would be underpredicted by 59.2%. The results also show that not modelling the gap would overpredict the temperature within the cavity by an average of 65.2% and 106.2% at 1.0 m and 1.5 m height, respectively. Lastly, parametric studies on cavity width found that HRR does not scale linearly with reduced cavity width. It is important to emphasise that the current pyrolysis model is not valid for combustible facades, and further development on the model is required to study the effect of the cavity width in a combustible facade.

⁵ This chapter is based on a paper in progress: B. Khoo, W. Jahn, P. Kotsovinos, G. Rein, Addition of Pyrolysis Model inside the Narrow Cavity of a Flammable Facade.

6.1 Introduction

In the previous chapters, I have shown that the model can simulate fire in a non-combustible facade with a narrow cavity with reasonable accuracy. I have also shown that by extrapolating the model, the model can help us study how the fire dynamic in a cavity changes with varying cavity widths and how the cavity barrier could affect fire dynamics. However, previous scenarios do not represent a building facade of a modern building, as modern facade systems often could have thermal insulations to ensure they adhere to energy efficiency standards. These insulations can be combustible and will pyrolyse under heat and contribute to a severe facade fire. Studies have shown that the main fire hazard for systems with combustible insulations is the onset of pyrolysis, where high production of pyrolyzate is shortly followed [16]. Therefore, accurate prediction of pyrolysis is essential for the model to study the effect of a cavity in a facade fire.

Fire performance of facade systems using combustible insulations such as PIR, EPS, and Phenolic is an active field of research [111–115]. However, these experiments are expensive, and CFD models can complement large-scale experimental studies to further our understanding of the flammability of facade systems. Currently, there are very limited CFD simulations of combustible facade systems to study the effect of cavity width in the literature. Existing simulations on cavity fire often do not model the pyrolysis and use a prescribed burning rate when it reaches the material ignition temperature. Although this allows the model to predict results to a reasonable degree of accuracy, it is limited to materials with poor fire performance [116]. Therefore, using these models to study combustible insulation with various fire performances is inappropriate.

This chapter explores the potential use of a simple one-step pyrolysis model to simulate PIR insulation degradation in a facade system. The pyrolysis kinetics used for PIR insulation will be obtained based on two different TGA data available in the literature to represent two PIR with different combustibility. Using these kinetics, the model will explore the effect of pyrolysis modelling on predicting the flammability of the facade system. The model will also be used to study the effect of different material heat of combustion, different cavity widths, and the importance of modelling gaps between the cladding panels to predict fire dynamics in a narrow facade cavity.

6.2 Experimental Setup

In this chapter, the experimental setup for Scenario 5 (combustion with pyrolysis) is based on the experimental work by Guillaume et al. Readers are referred to the paper for a detailed description of the setup [27]. The experimental setup is based on the standard ISO 13785-1, which represents an intermediate-scale facade mock-up with a back and side wall. The dimension of the mock-up is shown in Figure 6.1.

The surface temperature of the PIR is measured using thermocouples at the back wall at five different locations. These locations are named L1 to L5 and are placed between the cladding panels' gaps. Each thermocouple is spaced 500 mm apart except L5, which is only 400 mm above L4. On the side wall, the PIR surface temperature is captured at S1 to S5, where they are placed at the centre of the side wall cladding panel and at the same height as L1 to L5, respectively. Finally, the gas temperature in the cavity is measured using four thermocouples at LC1, LC2, SC1 and SC2, where LC1 and LC2 measure the gas temperature between the cladding panel gaps at the height of 1200 mm and 2300 mm, respectively, while SC1 and SC2 measure the gas temperature at the centre of the side wall at the same height as LC1 and LC2 respectively.

The experiment is performed with nine different configurations achieved by a combination of three different aluminium composite material (ACM) panels and three different insulants. The cavity width in all configurations is 50 mm except at the cavity barrier, which is 24 mm wide. The cavity barrier used in the experiment is an intumescent barrier which will expand to close the cavity gap when heated. In addition, an L-profile aluminium plate is present at the opening of the facade cavity to delay flame entry into the cavity at the beginning of the experiment. Lastly, a 100 kW propane burner is placed directly below the facade system.

This chapter used only one configuration to explore the capability of the CFD model. The configuration is based on an A2 limited combustibility ACM panel (ACM A2) and the PIR insulant.

6.2.1 Material Properties

The ACM A2 and PIR material properties are described in Table 6.1. The char density of PIR is estimated based on TGA results from [111, 114], which shows the char density to be around 24.4% to 25.6% of the PIR density, giving the char density a range of 8.78 to 9.20 kg m⁻³. An average char density of 8.99 kg m⁻³ is used in this study. Two different PIR (PIRa and PIRb) pyrolysis kinetics were used in the simulation to understand the effect of different PIR formulations on facade system flammability. The heat of combustion of the pyrolyzate released from the decomposition of the material is computed as:

$$\rho_v \cdot \Delta H_c = (\rho_v - \rho_{char}) \cdot \Delta H_{pyr} + \rho_{char} \cdot \Delta H_{char} \quad (9)$$

The first term on the left corresponds to PIR, with ΔH_c being to the heat of combustion of the PIR. On the right-hand side, the first term corresponds to pyrolyzate, with ΔH_{pyr} being the heat of combustion of the pyrolyzate, and the second term corresponds to the char, with ΔH_{char} being the heat of combustion of the char. (FireFoam default value of 32.8 x 10⁶ J kg⁻¹ is used).

Table 6.1 Material thermal properties and their corresponding pyrolysis kinetics.

Properties	ACM A2	PIRa ¹	PIRb ²	Cavity Barrier
Bulk Density, ρ_v [kg m ⁻³]	1360	36.0	36	360
Char Density, ρ_c [kg m ⁻³]	-	8.99	8.99	-
Absorbtivity/Emissivity, α/ϵ [-]	0.7	1	1	1
Specific heat capacity, c_p [J kg ⁻¹ K ⁻¹]	3000	1100	1100	1000
Thermal conductivity, k [W m ⁻¹ K ⁻¹]	0.64	0.048	0.048	0.038
Reaction order, n [-]	-	5	3.6	-
Pre-exponential Factor, A [s ⁻¹]	-	2.0 x 10 ⁸	8.0 x 10 ¹⁵	-
Activation Energy, E_a [J mol ⁻¹]	-	1.2 x 10 ⁵	2.0 x 10 ⁵	-
Heat of combustion of PIR, ΔH_c [J kg ⁻¹]	-	26.3 x 10 ⁶	26.3 x 10 ⁶	-

¹Pyrolysis kinetic is based on Marquis et al. [113]

²Pyrolysis kinetic is based on Hildago [117]

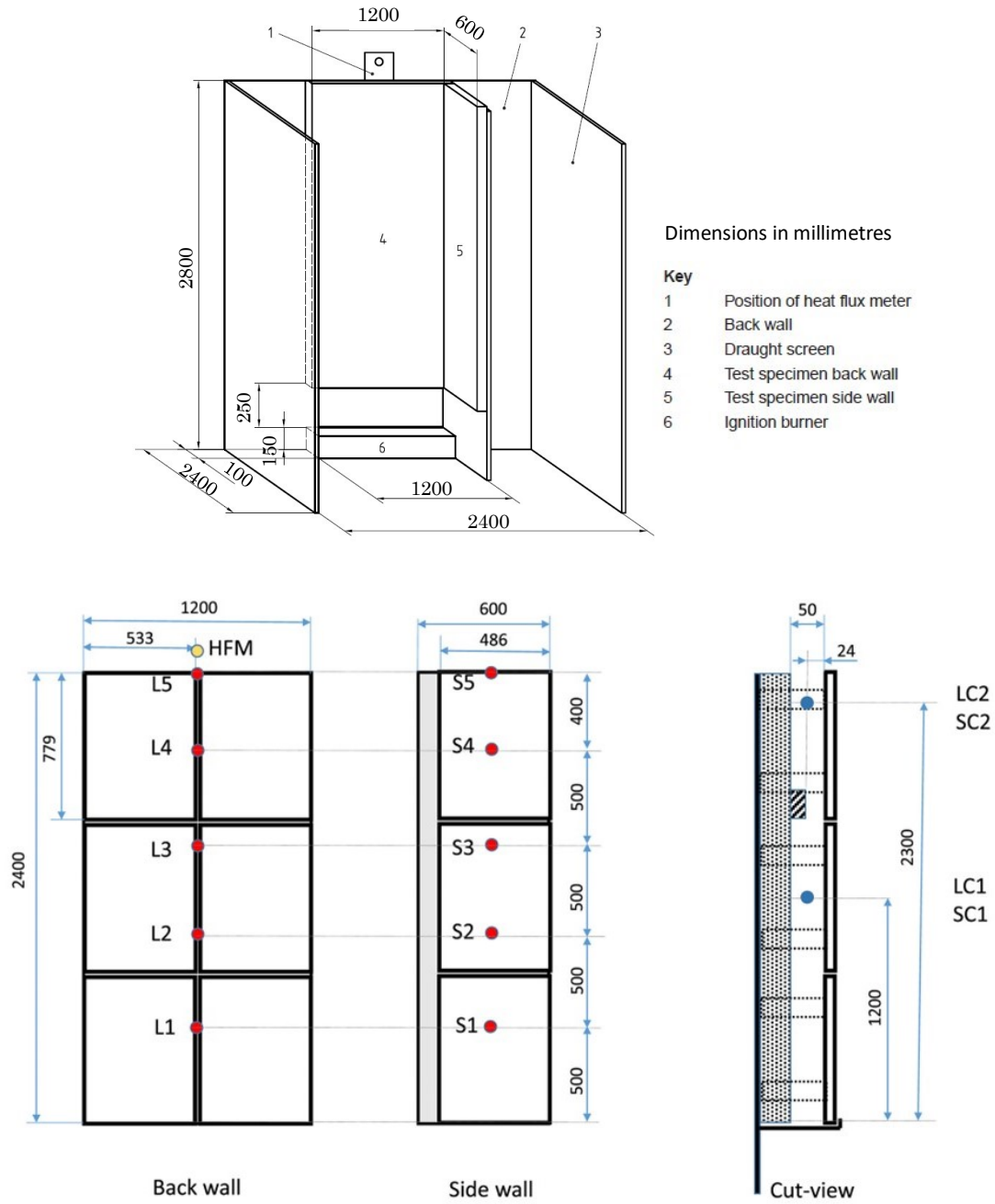


Figure 6.1 General test setup arrangement based on ISO 13785-1. The dimensions of the facade system are as prescribed in the standard. [118], while the location of the panels, cavity width and cavity barrier and sensors are as defined by Guillaume et al. [27]. L1-L5 and S1-S5 are thermocouples embedded in the PIR, while LC1-LC2 and SC1-SC2 are suspended at the centre of the cavity.

6.3 Numerical Methods

Similar to the previous chapters, the numerical settings used are similar to those defined in Chapter 3 and 4. Any additional settings and changes are described in this section.

Pyrolysis

The default pyrolysis model in FireFOAM, where a simple one-step decomposition of PIR is applied:



It is important to note that while the heat input for char oxidation is considered in the insulation combustion model, char removal in the solid phase due to oxidation is not considered and may be a source of error in the simulation. Further explanation of this error will be discussed in the next section.

The reaction rate of the PIR pyrolysis is estimated using an Arrhenius-like reaction as:

$$\dot{\omega}_i = Ae^{-\frac{E_a}{RT}} m_i^{n_i} \quad (6.11)$$

where $\dot{\omega}$ is the reaction rate, A is the pre-exponential factor, E_a is the activation energy, R is the universal gas constant, T is the temperature, m is the PIR mass fraction, and n is the order of reaction

All combustion in the gas phase is treated as complete combustion of propane gas, as described in Chapter 3. To achieve this, the conversion of the PIR pyrolyzate to its propane equivalent term is given by:

$$\dot{m}''_{PIR} = \dot{m}''_{pyr} \cdot \frac{\Delta H_{pyr}}{\Delta H_c} \quad (6.12)$$

where \dot{m}''_{PIR} is the pyrolyzate mass flux in terms of propane ($\text{kg m}^{-2} \text{s}^{-1}$) and \dot{m}''_{pyr} is pyrolyzate the mass flux rate ($\text{kg m}^{-2} \text{s}^{-1}$).

Radiation

The numerical settings for radiation are similar to those described in Chapter 4. However, as there are two different fuels involved in the simulation, i.e. pyrolyzate and propane, the radiative fraction, χ , is no longer constant. Accordingly, to compute the χ , a scaling expression is derived based on the radiant fraction of both propane and PIR as follows:

$$\chi = \frac{\dot{m}_{prop} \cdot \chi_{prop} + \dot{m}_{PIR} \cdot \chi_{pyr}}{\dot{m}_{prop} + \dot{m}_{PIR}} \quad (6.13)$$

where \dot{m}_{prop} is the mass flow rate of the propane from the burner, χ_{prop} is the radiant fraction of the propane set to 0.3, χ_{pyr} is the radiant fraction of PIR set to 0.60, as described in the literature [35].

Sensitivity analysis for the effect of the radiant fraction is performed. This is studied by varying the propane radiant fraction by varying the fraction value between 0.27 to 0.40. The results show that the difference in heat flux prediction at the L1 is no more than 7 % while the difference in HRR prediction is no more than 5 %. Table 6.2 shows the predicted heat flux prediction at L1 and the prediction of the PIR HRR.

Table 6.2 Effect of the radiant fraction on heat flux and insulation HRR predictions.

Radiant Fraction	Heat Flux at L1 [kW m ⁻²]	Insulation HRR [kW]
0.27	8.270	5.77
0.30	8.444	5.69
0.33	8.187	5.55
0.34	8.366	5.60
0.40	8.826	5.47

Convection

The numerical settings for convection are similar to those described in Chapter 3, where convection is solved directly. However, an additional convective wall model is introduced due to potential underpredictions of convective heat flux on the PIR [12]. The reason for this is twofold: a fine mesh of the order of 1mm is required to predict the boundary layer and account for the 'blowing effect' where pyrolyzate mass flux from the insulation reduces the convective heat flux. The Simplified Stagnant Film Theory wall function (SSFT) developed by Wang et al. [97] was applied to avoid using fine mesh size, and it is expressed as shown below:

When $\dot{m}''_{pyr} < 10^{-4} \text{ kg m}^{-2} \text{ s}^{-1}$:

$$q''_c = \frac{\min(\max(0, q''_{conv}), q''_{conv,threshold})}{q''_{conv,threshold}} \cdot q''_{conv,flame} \quad (6.14)$$

When $\dot{m}''_{pyr} \geq 10^{-4} \text{ kg m}^{-2} \text{ s}^{-1}$:

$$q''_c = \frac{\dot{m}''/h_m}{\exp(\dot{m}''/h_m) - 1} \cdot q''_{conv,flame} \quad (6.15)$$

where q''_c is the computed convective heat flux on the PIR, q''_{conv} is the convective heat transfer directly solved by simulation, $q''_{conv,flame}$ is the maximum turbulent convective heat transfer, estimated at 20 kW m^{-2} by assuming the maximum temperature difference between the surface and gas phase, $q''_{conv,threshold}$ is a threshold parameter, and h_m is the mass transfer coefficient, set at 0.01 kg m^{-2} [119].

In Eq. (6.14), a scaling function between the maximum turbulent convective heat flux and the directly solved convective heat transfer is used to calculate the computed convective heat flux on the PIR. In Eq. (6.15), the computed convective heat flux on the PIR considers the effect of the blowing effect when the mass flow rate from the PIR is more than $10^{-4} \text{ kg m}^{-2} \text{ s}^{-1}$.

One disadvantage of this convective wall function is that it does not consider the local properties of the flow. For example, the flame temperature that determined the convective

heat transfer is an a-priori-determined value, not calculated by the model. Therefore, simulations with and without wall functions are conducted to explore if the model is suitable.

6.4 Computational Domain and Simulation Setup

The numerical domain of Scenario 5, as shown in Figure 6.3, is 3800 x 1600 x 1800 mm³. The grid sensitivity analysis is performed with the mesh size of 25 mm (Coarse), 12.5 mm (Medium) and 6.25 mm (Fine), with a total cell number of 195,508, 711,616 and 1,250,816, respectively. For each mesh setting, the grid size near the PIR insulation and cladding is halved in the normal direction to improve convective heat transfer prediction. The grid sensitivity analysis shows that for gas temperature in the cavity, the differences between Fine and Medium mesh are minimal, with an average difference of 17%, while the difference between Fine and Coarse has an average difference of 40%, as shown in Figure 6.2. Figure 6.2 also shows that for the directly solved convective heat flux prediction, the Medium mesh underpredicts the heat flux by around 50% at the lower region and gradually converges with increasing height compared to the Fine mesh. The analysis shows that the 25 mm grid size is unsuitable as it significantly underpredicts the gas temperature and convective heat flux compared to the Fine mesh. While the Coarse mesh's convective heat flux at 0.5 m height is similar to the Fine mesh, the lack of resolution likely resulted in the fortuitous prediction. The grid sensitivity analysis shows that convective heat transfer prediction is highly sensitive to grid size. However, as Fine mesh size requires significantly more computational resources to simulate each case, the Medium mesh was chosen. A convective wall function was used, as described in Section 6.3, to ensure that the underprediction of convective heat flux is not the sole reason for any underprediction of insulation HRR.

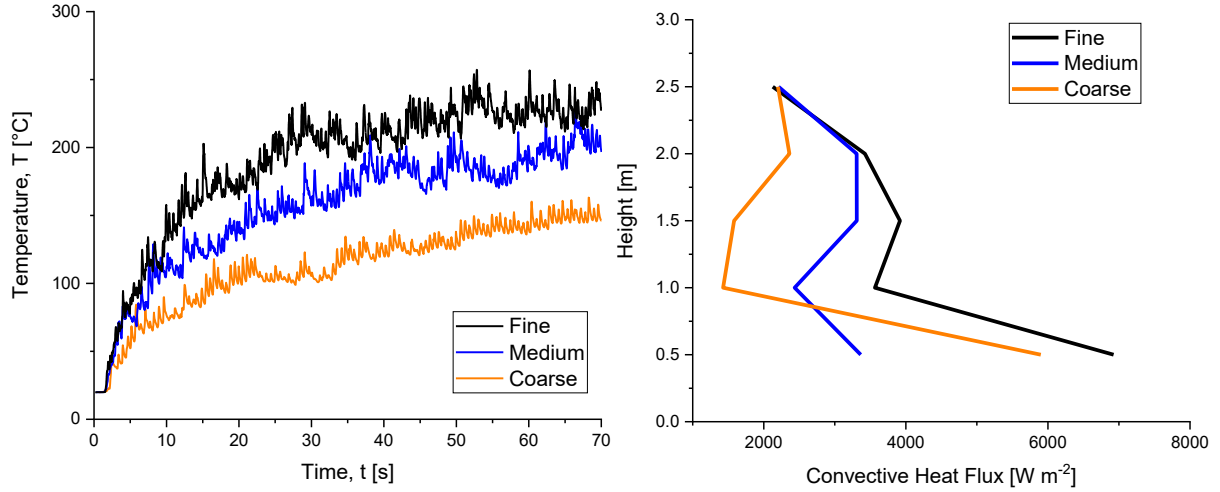


Figure 6.2 (Left) PIR temperature at the centre of the long wall at height 1.0 m. (Right) convective heat flux along the centre of the long wall. Results show that mesh sizes influence the result significantly at a lower height.

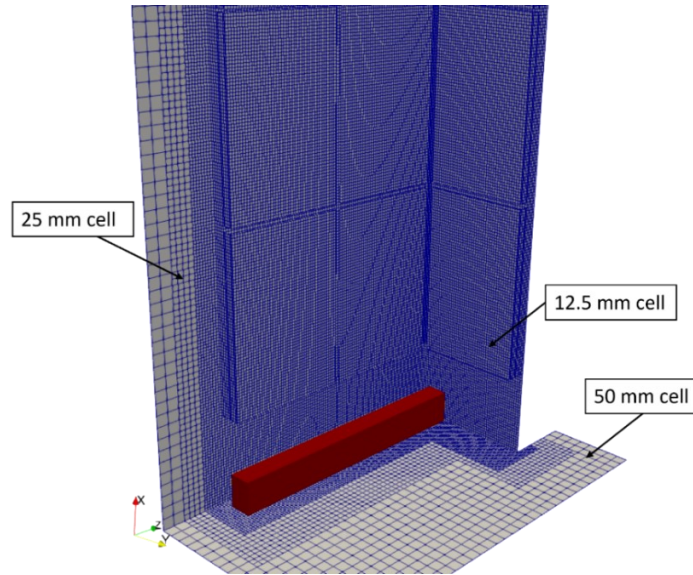


Figure 6.3 Computational Domain of Scenario 5 with Medium grid size (12.5 mm). The size and location of mesh refinement are as shown with further refinement at the PIR insulation and cladding, where the mesh size is halved to 6.25 mm.

For the solid phase, PIR and ACM A2 are modelled with 250 cells and 5 cells across their thickness (0.2mm and 0.8mm cell thickness), respectively. The total numerical cells are approximately 710,000 for the gas phase, 6,500,000 for PIR and 130,000 for A2 ACM panels.

To explore the effect of a gap at the junction between the cladding, two numerical cells are used to represent the gap. It is important to note that two numerical cells are not sufficient to replicate the boundary layer between the gap. However, due to the large computational resources required to resolve the flow at these gaps, some models use only one grid cell to represent the gap. Part of this chapter attempts to investigate insufficient resolution at these gaps would affect the model's prediction.

The boundary conditions applied are similar to those described in Chapter 4, except for the burner HRR, which is set to 2.16 g s^{-1} to simulate a HRR of 100 kW. For all simulations performed, the L-profile aluminium at the opening of the cavity is not modelled as FireFOAM was not capable of simulating the destruction of the L-profile aluminium.

In this chapter, a total of 18 simulations are performed to explore the model's capability in predicting the fire dynamics of a combustible facade system, the effects of unresolved flow between the cladding panel, and the effect of cavity width and insulant heat of combustion. The summary of all simulations performed is shown in Table 6.3. Note that for simulations investigating the effect of cavity width on the fire dynamics, the cavity barriers are not modelled to exclude the effect of cavity barriers.

Table 6.3 Summary of the cases investigated with their respective settings.

Cases	Cavity Width, W [mm]	Junction Gap	Pyrolysis Kinetic based on [PIRa/PIRb]	Convective Wall Function	The Heat of Combustion, ΔH_c, [J kg⁻¹] x 10⁶	Cavity Barrier
1	50.0	No	PIRa	Yes	26.3	Yes
2	50.0	No	PIRa	No	26.3	Yes
3	50.0	No	PIRb	Yes	26.3	Yes
4	50.0	No	PIRb	No	26.3	Yes
5	50.0	Yes	PIRb	No	26.3	Yes
6	50.0	No	PIRb	Yes	36.3	Yes
7	50.0	No	PIRb	Yes	46.3	Yes
8	50.0	No	PIRb	Yes	56.3	Yes
9	50.0	No	PIRb	Yes	26.3	No
10	62.5	No	PIRb	Yes	26.3	No
11	75.0	No	PIRb	Yes	26.3	No
12	87.5	No	PIRb	Yes	26.3	No
13	100	No	PIRb	Yes	26.3	No
14	50.0	No	PIRb	Yes	36.3	No
15	62.5	No	PIRb	Yes	36.3	No
16	75.0	No	PIRb	Yes	36.3	No
17	87.5	No	PIRb	Yes	36.3	No
18	100	No	PIRb	Yes	36.3	No

6.5 Results

Of the 18 simulations, the differences caused by pyrolysis kinetics and the capability of the current pyrolysis model are explored in Cases 1-4. These cases do not model the gap between the panels to avoid any uncertainty caused by the unresolved flow within the panel gap. The importance of simulating the gaps between the panels is investigated in Cases 4 and 5, while the effect of different insulant heat of combustion is explored in Cases 3, 6-8. Finally, Case 9-18 explores the effect of different cavity widths with two different insulant heats of combustions.

Pyrolysis Kinetics

As aforementioned, two different kinetics were investigated due to various formulations available for PIR. The chosen kinetics represents the difference between a non-fire retardant PIRa [114] and a fire retardant PIRb [117], and the parameters are shown in Table 6.1. The pyrolysis kinetics are estimated by inverse modelling TGA tests conducted in a nitrogen atmosphere. The estimated kinetics compared to the experimental result are shown in Figure 6.4.

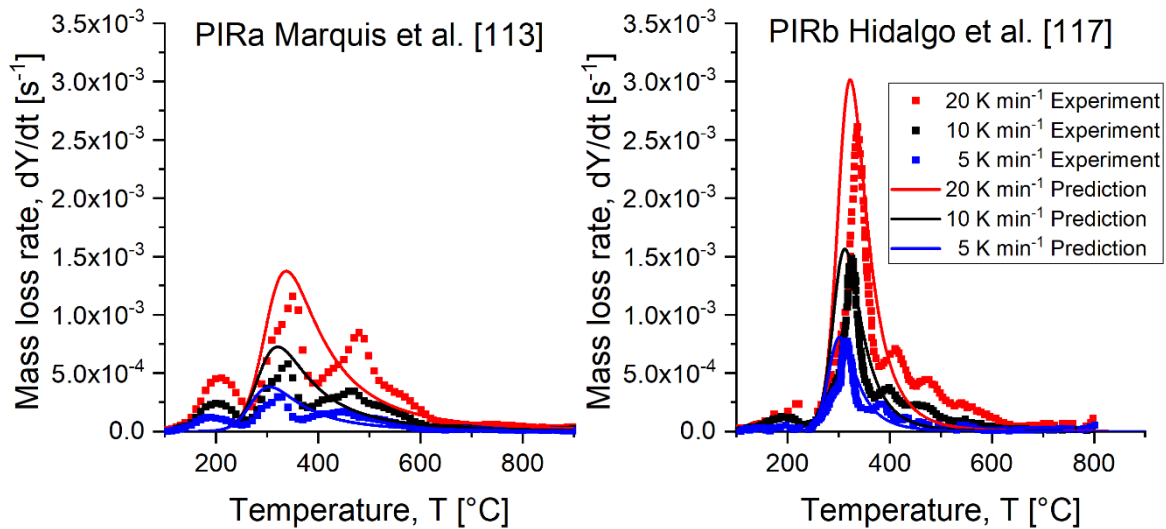


Figure 6.4 The estimated pyrolysis kinetic of PIR in a nitrogen atmosphere obtained via inverse modelling. Note that mass loss rates between the two PIRs are drastically different due to fire retardants in PIRa.

These predicted kinetics are then used to model the combustion of the insulant in Scenario 5, where each insulant is simulated with and without the convective wall function to ensure the underprediction of convective heat transfer does not result in an underprediction of insulant combustion.

Figure 6.5a shows that the PIR temperature prediction at L1 is accurate but not at L2 and L3, regardless of whether the convective wall function is used. This is due to the lack of cavity gap prediction, which will be discussed in the next section. Between Cases 1 to 4, the results show that the predicted PIR temperature between PIRa and PIRb shows minimal differences for cases with or without convective wall function.

For the air temperature in the cavity, the result shows that the differences between PIRa and PIRb are insignificant when the convective wall function is not used, as shown in Figure 6.5b. However, when the convective wall function is used, the predicted air temperature is about 200 °C higher at LC1 for PIRb. This is likely due to higher predicted convective heat flux by the wall function that reaches the critical heat flux, a heat flux where an ignited combustible material can self-sustain. As PIRb is less fire retardant, the critical heat flux is lower; hence, it releases combustible gas more readily. For temperatures above 2.0 m, it is important to note that while convective wall function partially resulted in the air temperature overprediction, FireFOAM lacked the functionality to model the closing of the cavity gap by an intumescent cavity barrier may contribute to the error due to hot air passing through the barrier.

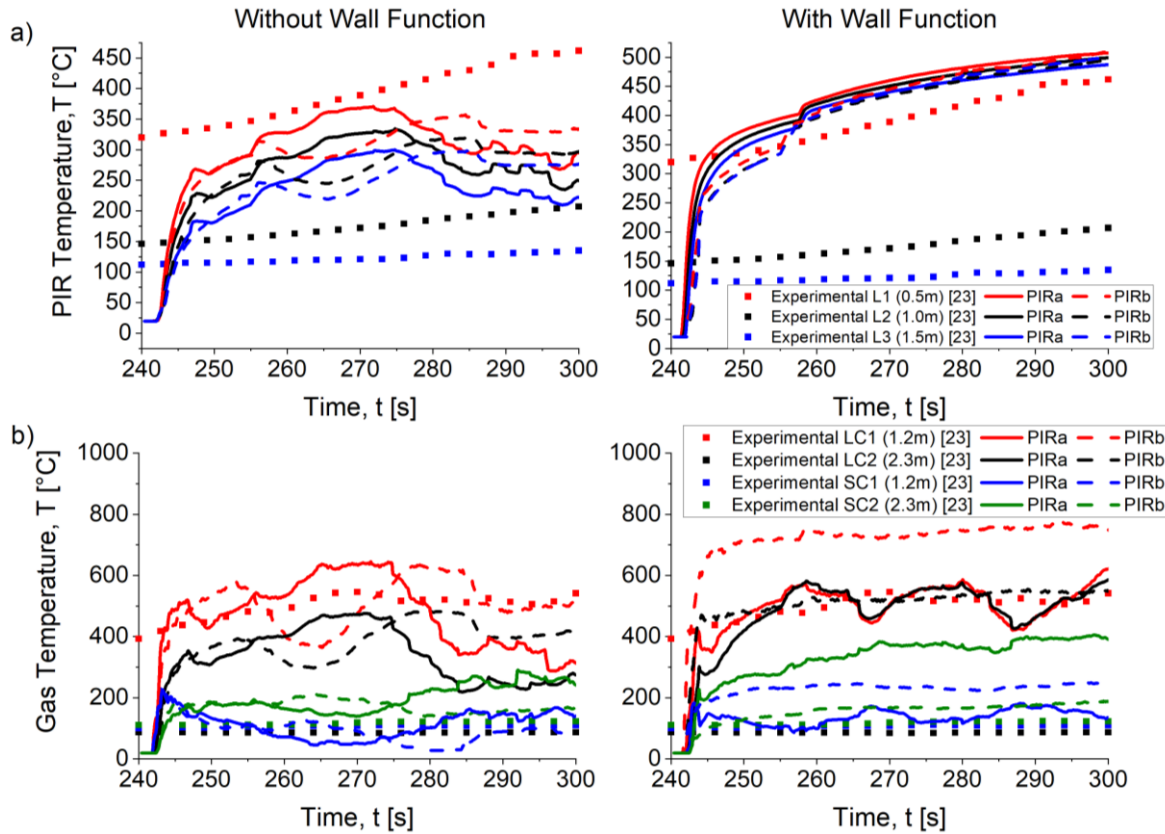


Figure 6.5 Comparison of Temperature Prediction by different pyrolysis Kinetics. a) The PIR temperature at L1, L2 and L3 b) The predicted air temperature in the cavity. Plots on the left do not use the convective wall function, while plots on the right use the convective wall function.

When analysing the HRR released by the insulant, as shown in Figure 6.6, the HRR predictions show that the pyrolysis kinetic has a significant effect when the convective wall function is used. The difference between the predicted HRR by PIRa and PIRb is approximately 33%, with PIRb being more combustible than PIRa. The results show that at the first cell of the PIR foam, the maximum char conversion of PIRa is only around 60%, while for PIRb, the conversion is 99%. The reason for this difference is mainly due to the fire retardant in PIRa that requires a higher heat flux to pyrolyse completely.

However, both pyrolysis kinetics underpredict the experiment measurement by approximately 67-83%. It was observed that the predicted HRR increases rapidly, then decreases and plateaus. The simulation results show that for PIRb, only around 1mm depth of the PIR is fully charred, and only a further 0.5mm depth of the PIR is involved in the pyrolysis process. Most of the 50mm thick insulation is not involved in the combustion

process due to the material's low thermal conductivity. It is hypothesised that char oxidation and cracking are essential in accelerating the degradation of the PIR as it would expose more virgin material to the flame. However, as char cracking and char oxidation remain an active field of research and FireFOAM does not have a model to predict both, the predicted HRR of the PIR cannot be predicted accurately. The development of a more accurate char model, whilst significant for the accurate prediction of PIR degradation, is not within the scope of this study, and therefore the kinetic of PIRb will be used for the rest of the simulations with an acknowledgement of the model's limitation.

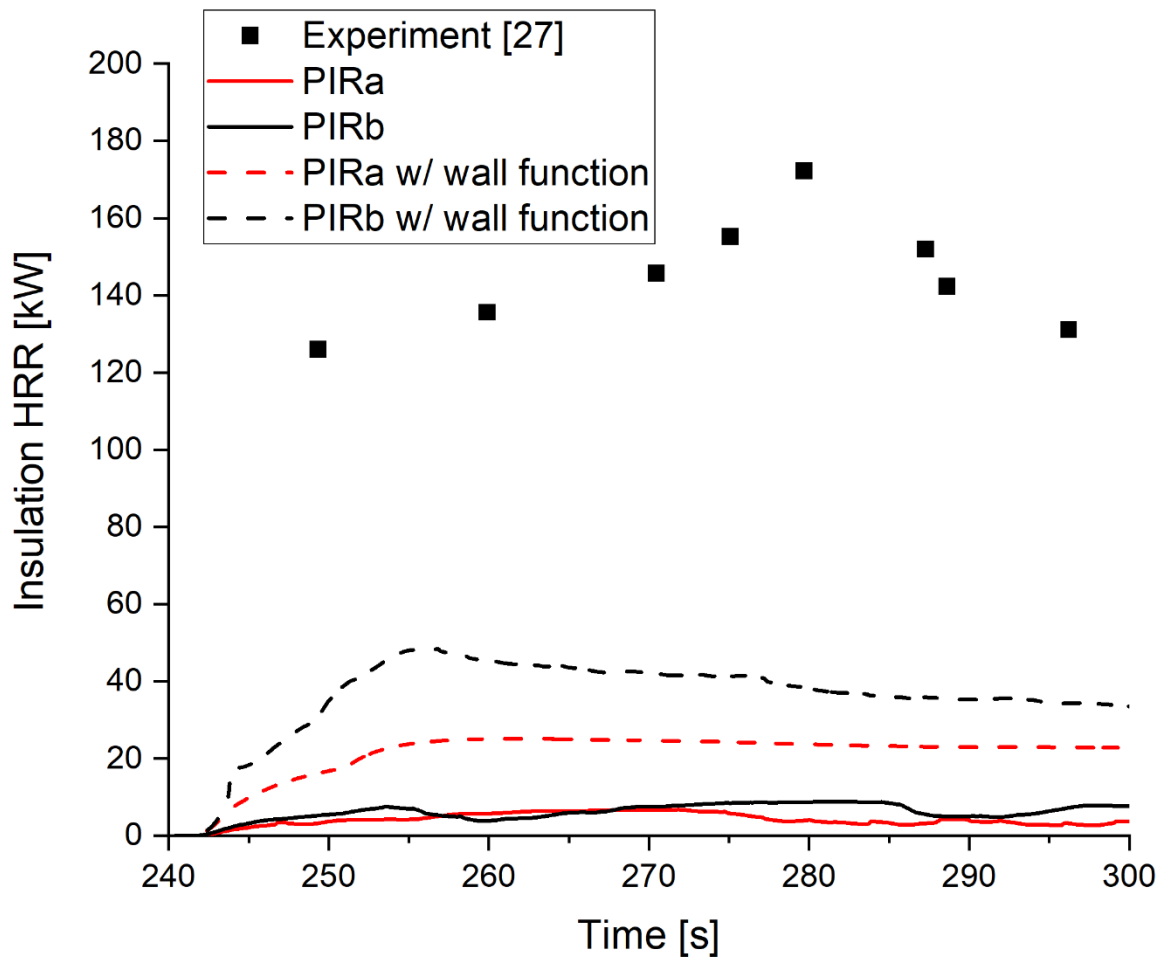


Figure 6.6 The predicted HRR in Case 1-4 compared to the experimental results. The pyrolysis kinetics has a huge influence on the overall PIR HRR, although results are still greatly underpredicted compared to experimental results.

Cladding Junction Gap

The simulation results for Case 4-5 represent two scenarios when the gap between the claddings was simulated and not simulated. In this scenario, the convective wall function was not implemented, as exploring the local prediction within the cavity is of interest. Figure 6.7 shows the prediction of PIR temperature and air temperature within the cavity for simulation with and without the gap at the cladding junctions. Results show that for Case 5, when the gap between the cladding is modelled, the PIR temperature at L1 is significantly underpredicted, with an average error of 59.2%. In comparison, L2 and L3 are predicted with an average error of 5.4% and 56.8%, respectively. For the air temperature prediction within the cavity, an average error of 36.3% and 3.2% is observed for LC1 and SC1, respectively. In contrast, LC2 and SC2 are overpredicted by an average error of 280.6% and 84.8%, respectively, due to the model's inability to simulate the intumescent cavity barrier.

When the gap between the panels is not modelled, the PIR temperature at L1 is better predicted than in Case 5, with an average error of 17.6%. However, at L2 and L3, the temperatures are overpredicted by an average error of 65.2% and 106.2%. As for the air temperature within the cavity, LC1 and SC1 are predicted with an error of 7.5% and 3.2%, respectively. However, similar to Case 5, the air temperature at LC2 and SC2 overpredict by an average error of 280.6% and 84.75%, respectively. This is likely due to the cavity barrier not shutting.

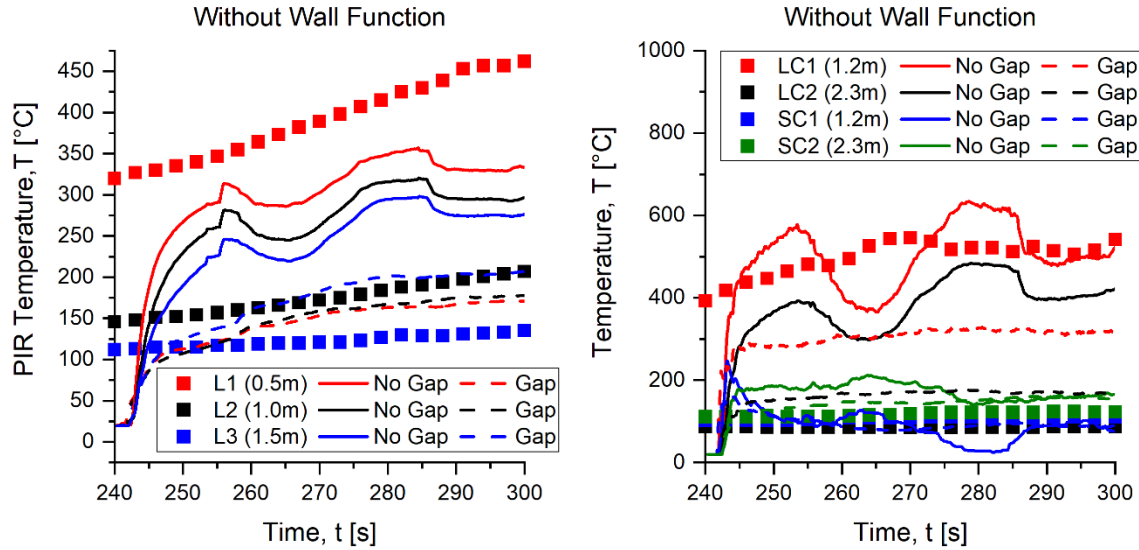


Figure 6.7 The results show the predicted temperature with and without the gaps between the cladding modelled. Simulation results show significant differences between the two, especially for prediction at the back wall.

One potential error for the underprediction of temperature at L1 when the gap is modelled is that air flow entering the cavity through the gaps at the cladding junction was not well resolved due to only two grid cells being used. As shown in Figure 6.8, the simulation shows that when the gap is modelled, the flame splits at the centre resulting in a lower PIR temperature prediction. This is because two grid cells are insufficient to resolve the boundary layers at the gap, and the poorly resolved flow may affect the flame behaviour. Similarly, when the gaps are not modelled, the airflow into the cavity via the gaps is not modelled, resulting in a more accurate PIR temperature at the L1. However, as the gaps between the claddings are not modelled, the air temperature and the flame structure within the cavity are not affected by air coming through the cladding gaps, resulting in an overprediction of PIR and air temperature at higher elevations.

The simulation results show that accurate modelling of the gap at the cladding junction is crucial in accurately predicting the flame shape and temperature in the cavity. However, as a huge amount of resources is required to predict the flow through the gap accurately, further studies are performed without a gap at the cladding junction to avoid errors associated with poor flow prediction.

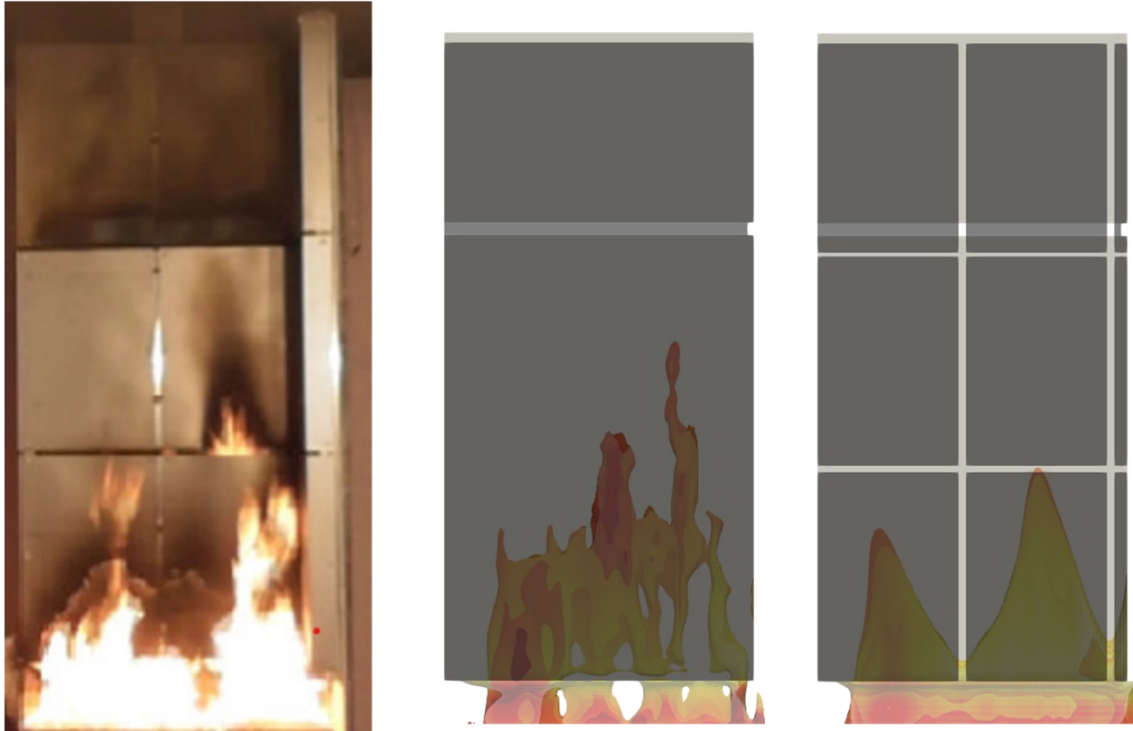


Figure 6.8 Flame shape in the cavity observed in the experiment, simulation without cladding junction gap, and simulation with cladding junction gap. Simulation shows that when the gap is present, the flame is split at the centre, potentially due to poorly resolved flow through the gap

Parametric studies

In the previous section, the simulated cases show that the current model is not sufficient to predict the facade flammability in its current state. In this section, the model intends to explore the sensitivity of different parameters of the facade flammability with the current model. While it is clear that the results obtained in this section do not represent real-world results, these results nevertheless may offer some insight into the effect of different parameters.

Insulant Heat of Combustion

Case 3 and Case 6-8 represent a parametric study on the effect of the heat of combustion of the insulations on a flammable facade system, ΔH_c . As shown in Figure 6.9, the simulation results show that the HRR increases linearly with ΔH_c . This suggests that the pyrolyzate released from the PIR does not increase with increasing ΔH_c . Analysis shows

that for all cases, the total pyrolyzate released from ΔH_c PIR foam is around $1.20 \text{ g s}^{-1} \pm 0.05\text{g}$

Figure 6.10 shows the predicted incident heat flux on the PIR foam over various ΔH_c . The results show that when ΔH_c increases, the incident heat flux on the PIR foam increases, as shown with the increasing contour area for 40 kW m^{-2} , 50 kW m^{-2} , and 60 kW m^{-2} . However, the increase in heat flux has not translated into an increase in pyrolyzate production. Instead, analysis shows that pyrolysis has been bottlenecked by the conduction heat transfer across the PIR as the char layer grows. As the temperature at the surface of the PIR foam would be relatively constant ΔH_c , the conduction heat transfer would remain similar for all cases. As a result, only a fraction of the energy would be used to pyrolyse the PIR foam. This further suggests that char oxidation and cracking may play an important role in the pyrolysis model as it would increase the surface area of virgin material to heat transfer. Therefore, it is hypothesised that char oxidation and cracking may need to be implemented in the pyrolysis model to predict the facade system's flammability accurately.

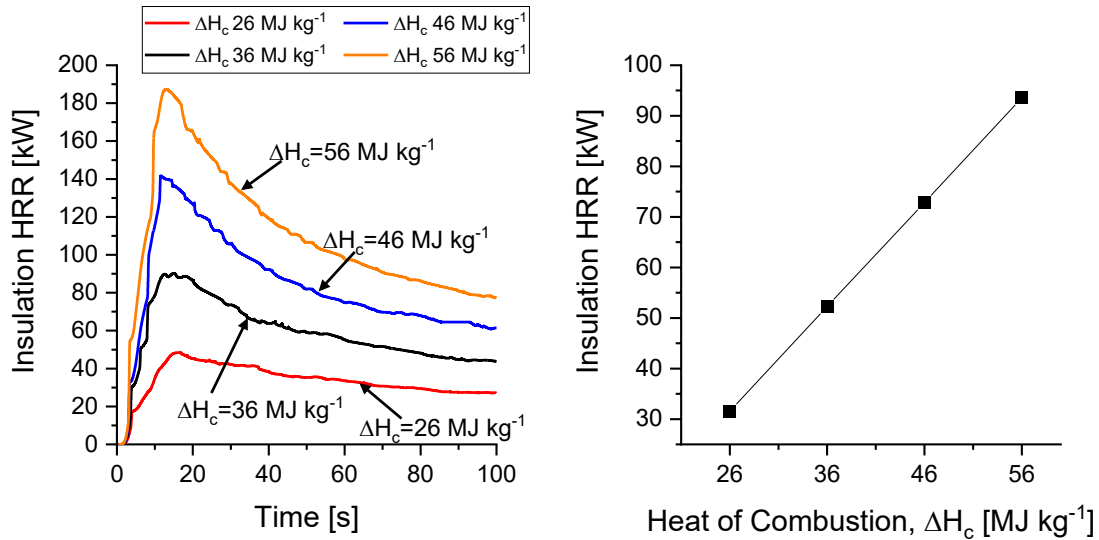


Figure 6.9 The PIR HRR over 100s and the average HRR with various ΔH_c . The simulation results suggest that ΔH_c does not increase the pyrolysis rate of the panel, as seen in the linear increase of HRR with increasing ΔH_c in the current simulation settings.

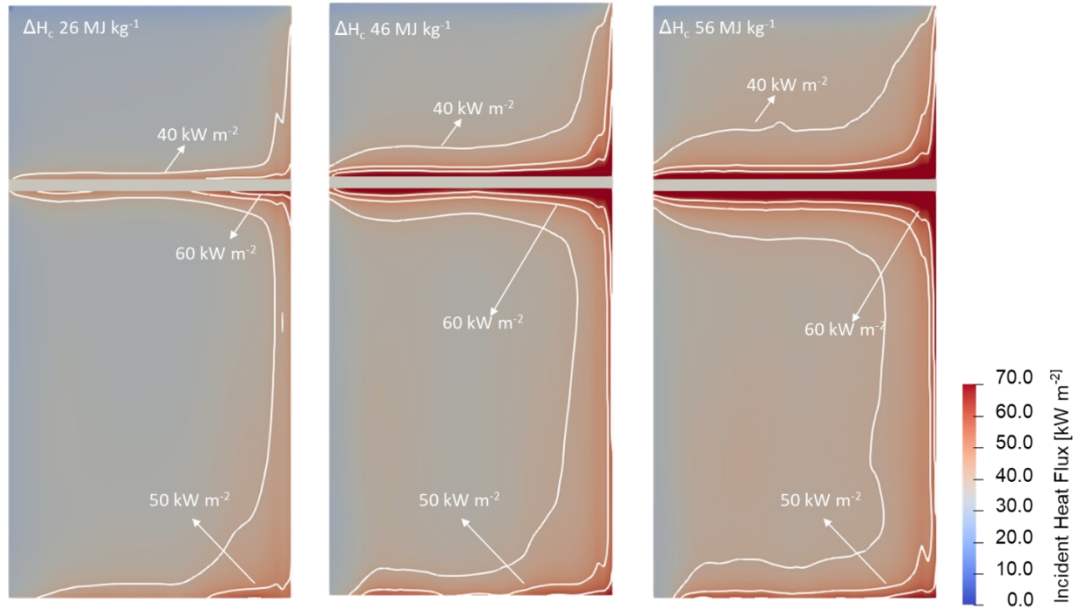


Figure 6.10 Predicted incident heat flux for $\Delta H_c = 26 \text{ MJ kg}^{-1}$, 46 MJ kg^{-1} and 56 MJ kg^{-1} . Results show that with increasing ΔH_c , the incident heat flux on the PIR foam increases.

Cavity width

Case 9 to 18 represent scenarios where parametric studies on the cavity width of a flammable facade system are studied. Figure 6.11 shows that the HRR within the cavity might not exhibit a linear relationship. At a $\Delta H_c = 26 \text{ MJ kg}^{-1}$, the effect of cavity width is less pronounced with a slight decrease from 50 mm to 75 mm and increases from 75 mm to 100 mm. However, given the chaotic nature of the fire, these slight increases may be a numerical noise. However, for ΔH_c more than 36 MJ kg^{-1} , the HRR reduces by around 5% from 50 mm cavity width to 62.5 mm. The HRR of the simulation then slowly increases with cavity width until the recorded HRR of 45 kW at 100 mm. However, it is essential to note that the lack of char oxidation and cracking may have reduced the flammability of the facade system with narrower cavity width. This is because the effect of increased re-radiation at a narrower cavity may not be evident due to the pyrolysis rate being bottlenecked by the lack of char oxidation and cracking.

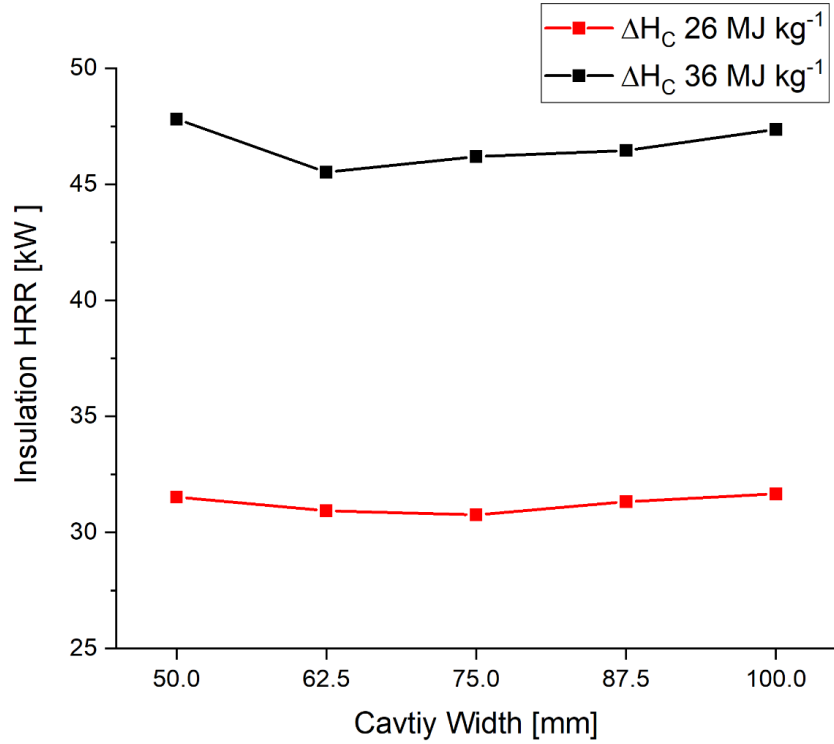


Figure 6.11 HRR contributed by the insulation with increasing cavity width. Simulation results suggest that at $\Delta H_c = 26 \text{ MJ kg}^{-1}$, cavity width has little effect on the over HRR. However, for $\Delta H_c = 36 \text{ MJ kg}^{-1}$, the effect of the cavity is slightly more pronounced, with a 5% HRR drop from a cavity width of 50 mm to 62.5 mm.

Figure 6.12 shows that at lower heights, the predicted heat flux increases with cavity width, while heat flux at a higher region decreases with cavity width. One potential reason for this increase is due to the reduced chimney effect, where more fuel was burnt at the lower region of the cavity, resulting in increased predicted heat flux and vice versa.

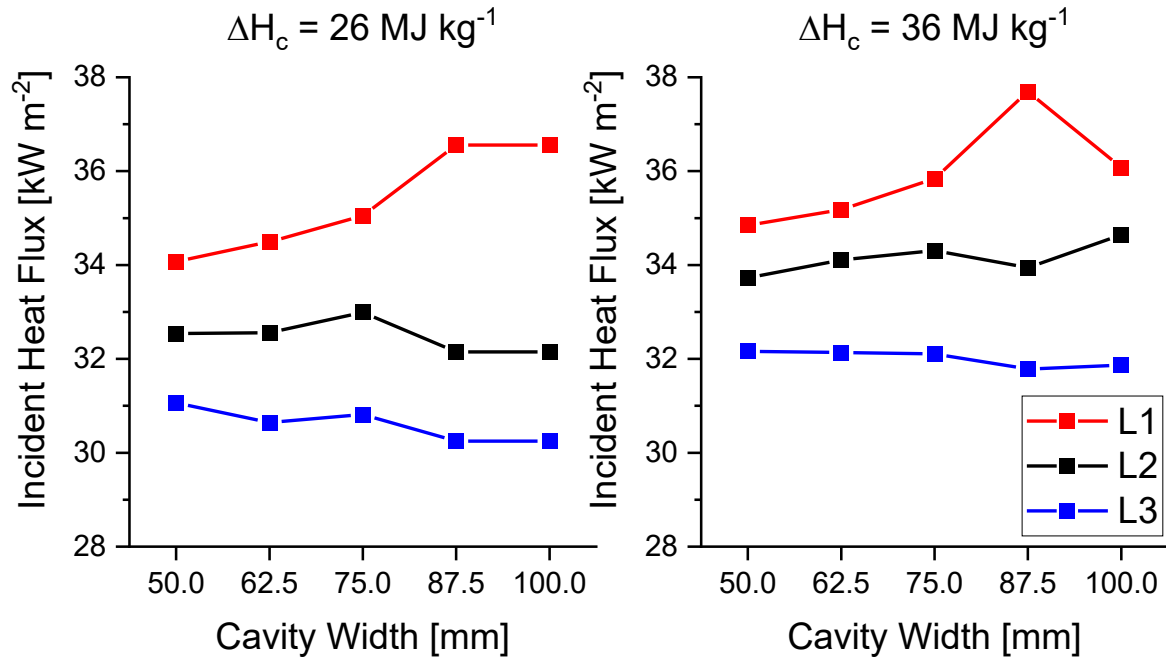


Figure 6.12 Predicted Incident Heat flux on the PIR foam at L1, L2 and L3. The simulation results show that while the predicted heat flux at L1 increases with cavity width, L2 and L3 do not decrease with cavity width.

6.6 Conclusion

In this chapter, the pyrolysis model was implemented into the CFD model to study how combustible insulation affects the flammability of the facade system. In this study, 18 simulations were performed to explore the ability of the current model to predict pyrolysis kinetics, cladding junction gap, insulant heat of combustion and cavity width on the flammability of the facade system.

The results found that pyrolysis kinetics plays a vital role in accurately predicting the facade system flammability. The reason for this is twofold, common insulant foam with the same trade name may contain formulations that contain fire retardant. This will drastically reduce its insulant reactivity and reduce the facade system's flammability. The simulation result found that using the fire retardant PIR and a non-fire retardant PIR may result in a 30% difference in HRR. The results also suggest that the current pyrolysis model cannot predict facade system flammability as it could not predict char oxidation and char cracking. This resulted in a reduced pyrolysis rate as less surface area is exposed to heating, reducing the predicted flammability drastically. The results also found that regardless of

the heat flux on the insulant, the amount of pyrolyzate released is relatively constant after a threshold heat flux.

Accurate prediction of the cladding junction gap may be crucial in predicting an accurate facade fire. Simulation results show that two grid cell is insufficient to represent the gap between the cladding. This is because more cell is required to resolve the boundary layer at the gap at the cladding junction. Failure to resolve the boundary entering the cavity through these gaps would result in poorly predicted flame shape, resulting in significant PIR and air temperature underprediction at L1, with an average error of 59%. On the other hand, results have also shown that not modelling the gap at the cladding junction would result in overpredicting PIR and air temperature at a higher elevation by an average of 60%. This is because there is no air entrainment from the gaps to cool the temperature in the cavity.

Lastly, parametric studies on the cavity width have been performed to explore its effect on facade flammability. The simulation results showed that the overall HRR decreased and then increased slightly with increasing cavity width. However, further development on the pyrolysis model is required to be confident in the results, as the current model is not capable of simulating combustible facade systems.

Chapter 7

Conclusions

7.1 Detailed conclusions

This thesis is the first to develop a step-by-step Multiphysics simulation of fire inside a narrow cavity of a flammable facade. The thesis intends to use FireFOAM to enhance our understanding of how cavities affect fire dynamics in a narrow cavity.

Chapter 2 presented a study on the 1973 Summerland fire and how its facade played a role in the disaster. It explains how novel materials were introduced and used without fully understanding their material properties and effect on building fire safety. When a fire accident occurs, these novel materials burn rapidly and spread into the facade cavity. As the fire burns in the cavity, occupants were unaware of the fire due to the flame hidden behind the facade cavity, and staff were not trained to inform the public. As a result, the flame was allowed to re-radiate within the cavity until the fire became large enough to engulf the entire building, resulting in 50 death. There were many parallels between the Summerland fire and the recent 2017 Grenfell Fire, where both structures have flammable facade materials and cladding. It is clear that while human error played a significant part in these disasters, there is a lack of understanding of how a flammable facade system with a cavity could affect building fire safety. Understanding this would require many experimental studies, which could be expensive. Therefore, the research in this thesis tried to develop a CFD model to complement experimental studies to help further our understanding of fire in a narrow cavity.

Chapter 3 details the step-by-step development of the thermofluid simulation inside a narrow cavity. As fire inside a narrow cavity is a strongly coupled problem, the CFD model must be validated one physical phenomenon at a time in a narrow cavity fire scenario to reduce the compensation effect. This chapter shows that the WALE model is preferred for a narrow cavity fire scenario. Simulation results show that for heat transfer and fluid flow,

the model could predict accurately except near walls, where a slight error was observed. The simulation results also found that when buoyancy is included, while still reasonably accurate, the fluid flow is slightly overpredicted throughout the cavity. The results strengthen the hypothesis that the physical phenomena in a narrow cavity fire need to be validated one at a time to limit the degree of freedom and therefore reduce the compensation effect of the model. This is essential to reduce the modelling error that could be present in scenarios explored in chapters 4, 5 and 6 due to combustion and pyrolysis.

In Chapter 4, the combustion model was added to study the fire dynamic inside a narrow cavity of a facade. In this chapter, a cavity fire was simulated over five different cavity widths and two burner HRRs. The simulation results found that the model could predict the trend of decreasing flame height with increasing cavity width. It also predicted the incident heat flux near the wall with reasonable accuracy for lower HRR. However, one of the key issues identified in the model was that a large amount of computing power is needed to predict the laminar-turbulent transition and the convective heat flux accurately. One benefit of a CFD model demonstrated in this chapter was the ability of CFD to view the fire from an angle difficult in an experiment. When simulating a narrow cavity, the simulation observed that air entrainment from the sides creates a circulation at the centre that moves the fuel toward the side. This resulted in the flame appearing to split into two peaks which are challenging to observe in an experiment. While it is unsure if the flame does split in real life, the model has been shown to predict most parameters with reasonable accuracy. This work in this chapter enables the model to be extrapolated to study fire in how different cavity configurations affect fire dynamics in Chapter 5 and enables the pyrolysis model to be validated with more confidence in Chapter 6.

Chapter 5 examines the potential and limitations of the extrapolating model to study fire in a different facade configuration. To achieve this, the simulation setup in Chapter 4 is modified by having horizontal and vertical cavity barriers. The vertical barriers were installed on two sides of the panel to restrict air entrainment from the sides. The results show that by altering airflow into the cavity, the fire dynamic in the cavity changes. The model extrapolation also found that the failed cavity barrier may potentially increase the facade system's flammability due to the cavity barrier's proximity to the wall, which could increase the re-radiation drastically. However, the results should be taken carefully as the

model is used outside its validated range. This meant that some changes might be required to ensure model accuracy, such as requiring a larger numerical domain to ensure minimal boundary effect.

In Chapter 6, the last physical phenomenon was incorporated into the CFD model. The pyrolysis kinetics was first explored to understand how different PIR formulations could affect fire behaviour. The study then focused on the ability of the FireFOAM to predict the flammability of the facade system. This chapter presented the importance of pyrolysis kinetic in predicting the facade flammability due to possible fire retardant used in an insulation foam of the same trade name. The chapter also shows that the current pyrolysis model is not capable of predicting facade fire due to char oxidising and cracking is not considered. As the insulant and char thermal conductivity is very low, the pyrolysis rate of the insulant would eventually be governed by the slow conduction heat transfer. In reality, these chars would oxidise or crack, exposing more surface area to pyrolyse. The hypothesis is further strengthened when a parametric study on increasing heat of combustion does not increase the pyrolysis rate. Observing the Char layer shows that only 1 mm of the insulant was charred while the rest were untouched, suggesting that heat transfer across the insulant is the bottleneck. Finally, this chapter showed that the insulation HRR might not increase linearly with cavity width. The simulation results show that HRR may first decrease and then slowly increase with cavity widths. However, it is important to note that the result may be affected by the pyrolysis model used, where the pyrolysis rate may be affected due to the lack of char oxidation and cracking.

7.2 Suggestions for Future work

While CFD models currently show promising futures to be used to study facade system flammability, they are currently far from being suitable for predicting facade system flammability. To ensure the model can be used to study facade system flammability, a list of suggestion are made in this section. In Chapter 4, the radiation fraction used was based on combustion in an open-air condition. While sensitivity analysis shows that the radiation fraction has minimal effect on the results for a facade cavity fire, this is only valid for facade systems with no combustible insulation present. Therefore, further investigation into the effect of radiation fraction or model may be warranted.

Furthermore, as shown in Chapter 5, investigating different facade configurations may require different computational domain sizes to ensure accuracy. Therefore, a suitable criterion for the computational domain may need to be established to ensure extrapolation can be performed confidently.

Lastly, results in Chapter 6 show that the current CFD model cannot predict combustible facade systems. To improve the model, further work should include: 1) Developing a char oxidation and cracking model to improve insulation pyrolysis rate, 2) Developing a model through empirical results to reduce the effect on model accuracy caused by gaps between cladding panels, 3) Developing and validating the model with a more realistic facade system where moisture barrier and mechanical structure are present, and lastly 4) Develop a more advanced convective wall function to reduce the required mesh size without compromising local prediction.

7.3 Significance of findings

Taken as a whole, this thesis demonstrates how the CFD fire modelling could help to improve our understanding of fire in a narrow facade cavity. By validating the CFD model one step at a time, we can isolate the individual physical phenomenon and validate them for a narrow cavity fire scenario. Once all models are validated, it gives us confidence that they could be extrapolated or help us pinpoint the simplification made on the model affecting model accuracy. Currently, most CFD models for narrow cavity fire are validated with all physical phenomena at a time [48, 49, 120]. The present work highlighted that by increasing the complexity of the model by simulating more physical phenomena, the degree of freedom in the model also increases. This may result in difficulty in pinpointing the modelling errors, making the model unreliable when extrapolated to study the effect of facade configuration on facade fire. Validating each physical phenomenon in a narrow cavity scenario allows the degrees of freedom in the model to be limited, and therefore allows a better understanding of the model's limitations.

An example of this was the model showing that insulant char may play a huge role in predicting the flammability of the facade system, and the char oxidation and cracking model may be required. Using this information, a more complex pyrolysis model could be

introduced to improve the model accuracy and allow further studies of the effect of a cavity on the overall flammability of a facade system.

One potential use of the model when further developed to predict narrow cavity fire is to investigate how different materials in a facade cavity could affect the overall flammability of a facade system. In this thesis, I have only performed studies where the only combustible material is the insulation. However, in practice, several combustible materials may be present in a facade system. For example, cladding, insulations, moisture, and weather barriers are potentially combustible. A parametric study of the effect of each material using experimental studies may not be practical due to the high cost of each experiment. Figure 7.1 represented a potential HRR vs cavity width graph when different materials with various flammability were present in a narrow cavity of a facade. A facade system could potentially have a design where facade flammability is at its lowest at certain cavity width. CFD model would hopefully be the key to unlocking a fire-safe facade design in the future.

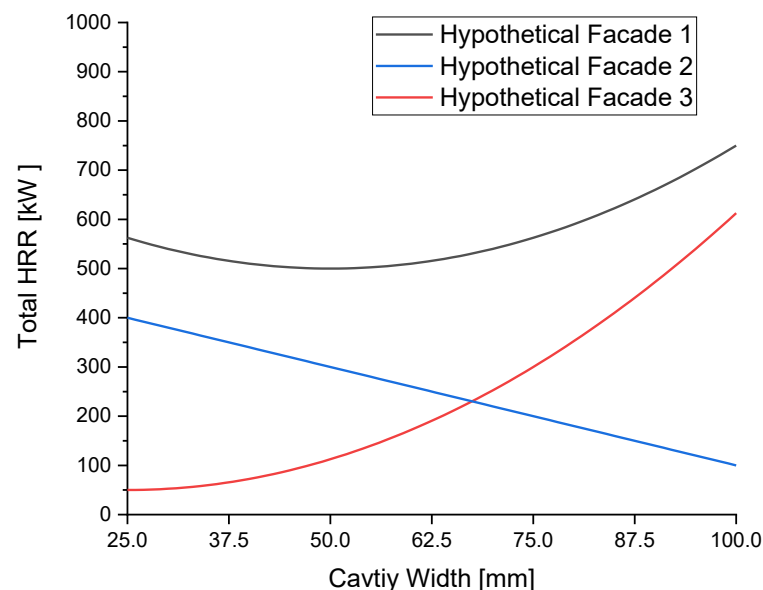


Figure 7.1 Hypothetical facade with different materials and facade configurations. At different cavity widths, these facade materials may perform differently due to different materials used in the construction.

REFERENCES

1. Herzog T, Krippner R, Lang W (2017) Facade Construction Manual, Second. DETAIL, Munich
2. O'Connor DJ (2016) The Building Envelope: Fire Spread, Construction Features and Loss Examples. In: SFPE Handbook of Fire Protection Engineering. Springer New York, New York, NY, pp 3242–3282
3. Colwell S, Baker T (2013) Fire Performance of External Thermal Insulation For Walls of Multistorey Buildings, Third Edit. IHS BRE Press, Watford
4. Bonner M, Rein G (2018) Flammability and Multi-objective Performance of Building Facades: Towards Optimum Design. *Int J High-Rise Build* 7:363–374
5. Bonner M, Wegrzynski W, Papis BK, Rein G (2020) KRESNIK : A top-down, statistical approach to understand the fire performance of building facades using standard test data. *Build Environ* 169:106540. <https://doi.org/10.1016/j.buildenv.2019.106540>
6. Oleszkiewicz I (1990) Fire exposure to exterior walls and flame spread on combustible cladding. *Fire Technol* 26:357–375. <https://doi.org/10.1007/BF01293079>
7. Hirschler MM (2021) Façade requirements in the 2021 edition of the US International Building Code. *Fire Mater* 45:586–597. <https://doi.org/10.1002/fam.2803>
8. (2018) CLADDING APPROVALS: A review and investigation of potential shortcomings of the BS8414 standard for the approval of cladding systems such as those commonly used on tall buildings
9. Hackitt J (2018) Independent Review of Building Regulations and Fire Safety: Final Report
10. (2018) Government Response to the Consultation on Amendments to Statutory

11. Boström L, Duny M, McNamee R (2016) Fire test of ventilated and unventilated wooden facades
12. Kim JS, de Ris J, Kroesser FW (1974) Laminar burning between parallel fuel surfaces. *Int J Heat Mass Transf* 17:439–451. [https://doi.org/10.1016/0017-9310\(74\)90015-5](https://doi.org/10.1016/0017-9310(74)90015-5)
13. Chow CL (2011) Numerical Studies On Smoke Spread In The Cavity Of A Double-Skin Facade. *J Civ Eng Manag* 17:371–392. <https://doi.org/10.3846/13923730.2011.595075>
14. Connolly RJ (1994) “Investigation of the behaviour of external cladding system in fire. Report on 10 full-scale fire test”, CI
15. Rasbash DJ (1991) Major fire disasters involving flashover. *Fire Saf J* 17:85–93. [https://doi.org/10.1016/0379-7112\(91\)90030-3](https://doi.org/10.1016/0379-7112(91)90030-3)
16. Hidalgo JP, Welch S, Torero JL (2015) Performance criteria for the fire safe use of thermal insulation in buildings. *Constr Build Mater* 100:285–297. <https://doi.org/10.1016/j.conbuildmat.2015.10.014>
17. Lie TT (1972) Contribution of insulation in cavity walls to propagation of fire. *Fire Study* 29:15
18. Choi KK, Taylor W (1984) Combustibility of Insulation in Cavity Walls. *J Fire Sci* 2:179–188. <https://doi.org/10.1177/073490418400200303>
19. Taylor W (1983) Fire spread in concealed foamed plastic insulation. *Fire Technol* 19:192–203. <https://doi.org/10.1007/BF02378699>
20. Karlsson B, Thomas PH, Holmstedt G (1995) Flame sizes in a small scale stack: pilot experiments.
21. Ingason H (1998) Modelling of a two-dimensional rack storage fire. *Fire Saf J* 30:47–69. [https://doi.org/10.1016/S0379-7112\(97\)00024-6](https://doi.org/10.1016/S0379-7112(97)00024-6)

22. De Ris JL, Orloff L (2005) Flame Heat Transfer Between Parallel Panels. *Fire Saf Sci* 8:999–1010. <https://doi.org/10.3801/IAFSS.FSS.8-999>
23. Tamani F, Moussa AN (1980) Experiments on the Turbulent Burning of Vertical Parallel Walls. *Combust Sci Technol* 23:143–151. <https://doi.org/10.1080/00102208008952405>
24. Most J, Bellin B, Joulain P, Sztal B (1989) Interaction Between Two Burning Vertical Walls. *Fire Saf Sci* 2:285–294. <https://doi.org/10.3801/IAFSS.FSS.2-285>
25. Foley M, Drysdale DD (1995) Heat transfer from flames between vertical parallel walls. *Fire Saf J* 24:53–73. [https://doi.org/10.1016/0379-7112\(94\)00033-C](https://doi.org/10.1016/0379-7112(94)00033-C)
26. Ren N, de Vries J, Zhou X, et al (2017) Large-scale fire suppression modeling of corrugated cardboard boxes on wood pallets in rack-storage configurations. *Fire Saf J* 91:695–704. <https://doi.org/10.1016/j.firesaf.2017.04.008>
27. Guillaume E, Fateh T, Schillinger R, et al (2018) Study of fire behaviour of facade mock-ups equipped with aluminium composite material-based claddings, using intermediate-scale test method. *Fire Mater* 1–17. <https://doi.org/10.1002/fam.2635>
28. Livkiss K, Svensson S, Husted B, van Hees P (2018) Flame Heights and Heat Transfer in Facade System Ventilation Cavities. *Fire Technol* 1–25. <https://doi.org/10.1007/s10694-018-0706-2>
29. Jamison KLT, Boardman DA (2016) A new fire performance test for cavity wall insulation. *MATEC Web Conf* 46:1–12. <https://doi.org/10.1051/mateconf/20164602004>
30. Quintiere JG (1989) Scaling applications in fire research. *Fire Saf J* 15:3–29. [https://doi.org/10.1016/0379-7112\(89\)90045-3](https://doi.org/10.1016/0379-7112(89)90045-3)
31. Saito K, Ito A, Nakamura Y, Kuwana K (2015) *Progress in Scale Modeling, Volume II*. Springer International Publishing, Cham
32. Quintiere JG (2020) Scaling realistic fire scenarios. *Prog Scale Model an Int J* 1:.

<https://doi.org/10.13023/psmij.2020.01>

33. McCaffrey BJ, Quintiere JG, Harkleroad MF (1981) Estimating room temperatures and the likelihood of flashover using fire test data correlations. *Fire Technol* 17:98–119. <https://doi.org/10.1007/BF02479583>
34. Quintiere JG (1989) Fundamentals of Enclosure Fire “Zone” Models. *J Fire Prot Eng* 1:99–119. <https://doi.org/10.1177/104239158900100302>
35. Hurley MJ, Gottuk D, Hall JR, et al (2016) *SFPE Handbook of Fire Protection Engineering*. Springer New York, New York, NY
36. McGrattan K (2005) Fire Modeling: Where Are We? Where Are We Going? *Fire Saf Sci* 8:53–68. <https://doi.org/10.3801/IAFSS.FSS.8-53>
37. Yan Z, Holmstedt G (1999) Three-dimensional computation of heat transfer from flames between vertical parallel walls. *Combust Flame* 117:574–588. [https://doi.org/10.1016/S0010-2180\(98\)00092-3](https://doi.org/10.1016/S0010-2180(98)00092-3)
38. Smagorinsky J (1963) General Circulation Experiments With The Primitive Equations. *Mon Weather Rev* 91:99–164. [https://doi.org/10.1175/1520-0493\(1963\)091<0099:GCEWTP>2.3.CO;2](https://doi.org/10.1175/1520-0493(1963)091<0099:GCEWTP>2.3.CO;2)
39. Lilly DK (1966) The Representation Of Small-Scale Turbulence In Numerical Simulation Experiments
40. Deardorff JW (1973) The Use of Subgrid Transport Equations in a Three-Dimensional Model of Atmospheric Turbulence. *J Fluids Eng* 95:429–438. <https://doi.org/10.1115/1.3447047>
41. Kraichnan RH (1976) Eddy Viscosity in Two and Three Dimensions. *J Atmos Sci* 33:1521–1536. [https://doi.org/10.1175/1520-0469\(1976\)033<1521:EVITAT>2.0.CO;2](https://doi.org/10.1175/1520-0469(1976)033<1521:EVITAT>2.0.CO;2)
42. Deardorff JW (1970) A numerical study of three-dimensional turbulent channel flow at large Reynolds numbers. *J Fluid Mech* 41:453–480. <https://doi.org/10.1017/S0022112070000691>

43. McGrattan KB, Rehm RG, Baum HR (1994) Fire-Driven Flows in Enclosures. *J Comput Phys* 110:285–291. <https://doi.org/10.1006/jcph.1994.1025>
44. Wang HY, Joulain P (2000) Numerical Study of the Turbulent Burning between Vertical Parallel Walls with a Fire-Induced Flow. *Combust Sci Technol* 154:119–161. <https://doi.org/10.1080/00102200008947274>
45. Ren N, Wang Y, Vilfayeau S, Trouvé A (2016) Large eddy simulation of turbulent vertical wall fires supplied with gaseous fuel through porous burners. *Combust Flame* 169:194–208. <https://doi.org/10.1016/j.combustflame.2015.12.008>
46. Le D, Labahn J, Beji T, et al (2018) Assessment of the capabilities of FireFOAM to model large-scale fires in a well-confined and mechanically ventilated multi-compartment structure. *J Fire Sci* 36:3–29. <https://doi.org/10.1177/0734904117733427>
47. Ji J, Li YF, Shi WX, Sun JH (2015) Numerical Studies On Smoke Spread In The Cavity Of A Double-Skin Facade. *J Civ Eng Manag* 22:470–479. <https://doi.org/10.3846/13923730.2014.897992>
48. Dréan V, Girardin B, Guillaume E, Fateh T (2019) Numerical simulation of the fire behaviour of facade equipped with aluminium composite material-based claddings-Model validation at large scale. *Fire Mater* 43:981–1002. <https://doi.org/10.1002/fam.2759>
49. Livkiss K, Husted BP, Beji T, van Hees P (2019) Numerical study of a fire-driven flow in a narrow cavity. *Fire Saf J* 108:102834. <https://doi.org/10.1016/j.firesaf.2019.102834>
50. Liu L, Guo Q-X (2001) Isokinetic Relationship, Isoequilibrium Relationship, and Enthalpy–Entropy Compensation. *Chem Rev* 101:673–696. <https://doi.org/10.1021/cr990416z>
51. Bal N, Rein G (2015) On the effect of inverse modelling and compensation effects in computational pyrolysis for fire scenarios. *Fire Saf J* 72:68–76. <https://doi.org/10.1016/j.firesaf.2015.02.012>

52. Khoo B, Skitt J (2019) The 1973 Summerland disaster — lessons to the building industry from the process industry. *Loss Prev Bull* 269:4
53. Bonner M, Rein G (2020) List of Facade Fires 1990 - 2020
54. Torero JL (2018) Grenfell Tower: Phase 1 Report
55. Board MF and ES (2014) Post Incident Analysis for Lacrosse Docklands
56. Slawson N (2017) Flames engulf 86-storey residential tower in Dubai. In: *Guardian*. <https://www.theguardian.com/world/2017/aug/03/flames-engulf-86-storey-residential-tower-in-dubai>. Accessed 15 Apr 2020
57. Harper D (1984) Memories must be jogged on Summerland's Lesson. *Fire* 77:31–34
58. Phillips I (2005) From 21st century leisure to 20th century holiday catastrophe: the Isle of Man Summerland fire disaster. unpublished
59. Byron D. (1971) Architect's account of the Summerland leisure centre. *Archit J* 156:5
60. Wilson-Dickson PS (1974) The Summerland Fire and Inquiry. *Fire Eng J* 34:8–14
61. Cantley J (1974) Report of the Summerland fire commission. Douglas
62. Barclay D (1974) Summerland Report: The Institute's response. *RIBA* 81:23
63. (2018) Survivor haunted by Summerland disaster that killed 50. In: *ITV*. <https://www.itv.com/news/utv/2018-08-02/survivor-haunted-by-summerland-disaster-that-killed-50>. Accessed 3 Dec 2022
64. Wong S (2019) Notre Dame's stonework isn't flammable but may be structurally damaged. In: *New Sci*. <https://www.newscientist.com/article/2199991-notre-dames-stonework-isnt-flammable-but-may-be-structurally-damaged/>. Accessed 26 Apr 2020
65. Dossi S (2021) Protection Layers Fire Safety of Buildings
66. (1974) Summerland: the analysis, the course of disaster, the blame, the recommendations. *Archit J* 159:1183–1188

67. Moore-Bick M (2019) Grenfell Tower Inquiry: Phase 1 Report
68. Yang K ~T., Chang L ~C. (1977) UNDSAFE-I: A computer code for buoyant flow in an enclosure. 33476
69. Yuen ACY, Yeoh GH, Timchenko V, et al (2016) Study of three LES subgrid-scale turbulence models for predictions of heat and mass transfer in large-scale compartment fires. *Numer Heat Transf Part A Appl* 69:1223–1241.
<https://doi.org/10.1080/10407782.2016.1139903>
70. Drysdale D (2011) *An Introduction to Fire Dynamics*. Wiley
71. Sharma A, Mishra KB (2021) Experimental investigations on the influence of ‘chimney-effect’ on fire response of rainscreen façades in high-rise buildings. *J Build Eng* 44:103257. <https://doi.org/10.1016/j.job.2021.103257>
72. Markatos NC, Malin MR, Cox G (1982) Mathematical modelling of buoyancy-induced smoke flow in enclosures. *Int J Heat Mass Transf* 25:63–75.
[https://doi.org/10.1016/0017-9310\(82\)90235-6](https://doi.org/10.1016/0017-9310(82)90235-6)
73. Lewis M, Moss J, Rubini P (1997) Cfd Modelling Of Combustion And Heat Transfer In Compartment Fires. *Fire Saf Sci* 5:463–474. <https://doi.org/10.3801/IAFSS.FSS.5-463>
74. Page F, Schlinger WG, Breaux DK, Sage BH (1952) Temperature Gradients In Turbulent Gas Streams. Point Values Of Eddy Conductivity And Viscosity. In *Uniform Flow Between Parallel Plates*. *Ind Eng Chem* 44:424–430.
<https://doi.org/10.1021/ie50506a059>
75. Gessner FB, Jones JB (1965) On some aspects of fully-developed turbulent flow in rectangular channels. *J Fluid Mech* 23:689–713.
<https://doi.org/10.1017/S0022112065001635>
76. Hussain AKMF, Reynolds WC (1975) Measurements in Fully Developed Turbulent Channel Flow. *J Fluids Eng* 97:568–578. <https://doi.org/10.1115/1.3448125>

77. Ideriah FJK (1980) Prediction of Turbulent Cavity Flow Driven by Buoyancy and Shear. *J Mech Eng Sci* 22:287–295.
https://doi.org/10.1243/JMES_JOUR_1980_022_054_02
78. Cheng C-H, Huang W-H, Kou H-S (1988) Laminar Free Convection Of The Mixing Flows In Vertical Channels. *Numer Heat Transf* 14:447–463.
<https://doi.org/10.1080/10407788808913655>
79. Moutsoglou A, Wong YH (1989) Convection-radiation interaction in buoyancy-induced channel flow. *J Thermophys Heat Transf* 3:175–181.
<https://doi.org/10.2514/3.145>
80. Maughan JR, Incropera FP (1990) Regions of heat transfer enhancement for laminar mixed convection in a parallel plate channel. *Int J Heat Mass Transf* 33:555–570.
[https://doi.org/10.1016/0017-9310\(90\)90189-2](https://doi.org/10.1016/0017-9310(90)90189-2)
81. Katoh Y, Miyamoto M, Kurima J, Kaneyasu S (1991) Turbulent Free Convection Heat Transfer from Vertical Parallel Plates : Effect of Entrance Bell-Mouth Shape. *JSME Int journal Ser 2, Fluids Eng heat Transf power, Combust Thermophys Prop* 34:496–501. https://doi.org/10.1299/jsmeb1988.34.4_496
82. Lyons SL, Hanratty TJ, McLaughlin JB (1991) Direct numerical simulation of passive heat transfer in a turbulent channel flow. *Int J Heat Mass Transf* 34:1149–1161. [https://doi.org/10.1016/0017-9310\(91\)90024-9](https://doi.org/10.1016/0017-9310(91)90024-9)
83. Kasagi N, Tomita Y, Kuroda A (1992) Direct Numerical Simulation of Passive Scalar Field in a Turbulent Channel Flow. *J Heat Transfer* 114:598–606.
<https://doi.org/10.1115/1.2911323>
84. Gau C, Yih KA, Aung W (1992) Reversed Flow Structure and Heat Transfer Measurements for Buoyancy-Assisted Convection in a Heated Vertical Duct. *J Heat Transfer* 114:928–935. <https://doi.org/10.1115/1.2911903>
85. Teitel M, Antonia RA (1993) Heat transfer in fully developed turbulent channel flow: comparison between experiment and direct numerical simulations. *Int J Heat Mass Transf* 36:1701–1706. [https://doi.org/10.1016/S0017-9310\(05\)80080-8](https://doi.org/10.1016/S0017-9310(05)80080-8)

86. Oberkampf WL, Trucano TG (2002) Verification and validation in computational fluid dynamics. *Prog Aerosp Sci* 38:209–272. [https://doi.org/10.1016/S0376-0421\(02\)00005-2](https://doi.org/10.1016/S0376-0421(02)00005-2)
87. Hong S-W, Exadaktylos V, Lee I-B, et al (2017) Validation of an open source CFD code to simulate natural ventilation for agricultural buildings. *Comput Electron Agric* 138:80–91. <https://doi.org/10.1016/j.compag.2017.03.022>
88. Miyamoto M, Katoh Y, Kurima J, Sasaki H (1986) Turbulent Free Convection Heat Transfer From Vertical Parallel Plates. In: *Proceeding of International Heat Transfer Conference 8*. Begellhouse, Connecticut, pp 1593–1598
89. (2017) FireFOAM, version dev. <https://github.com/fireFoam-dev/fireFoam-dev>
90. OpenFOAM, CFD package. <https://openfoam.org/>
91. Favre A (1983) Turbulence: Space-time statistical properties and behavior in supersonic flows. *Phys Fluids* 26:2851–2863. <https://doi.org/10.1063/1.864049>
92. Nicoud F, Ducros F (1999) Subgrid-scale stress modelling based on the square of the velocity. *Flow, Turbul Combust* 62:183–200. <https://doi.org/10.1023/A:1009995426001>
93. Ren N, Wang Y, Trouvé A (2013) Large eddy simulation of vertical turbulent wall fires. *Procedia Eng* 62:443–452. <https://doi.org/10.1016/j.proeng.2013.08.086>
94. Zhang W, Hamer A, Klassen M, et al (2002) Turbulence statistics in a fire room model by large eddy simulation. *Fire Saf J* 37:721–752. [https://doi.org/10.1016/S0379-7112\(02\)00030-9](https://doi.org/10.1016/S0379-7112(02)00030-9)
95. Maragkos G, Beji T, Merci B (2017) Advances in modelling in CFD simulations of turbulent gaseous pool fires. *Combust Flame* 181:22–38. <https://doi.org/10.1016/j.combustflame.2017.03.012>
96. Fureby C, Tabor G, Weller HG, Gosman AD (1997) A comparative study of subgrid scale models in homogeneous isotropic turbulence. *Phys Fluids* 9:1416–1429. <https://doi.org/10.1063/1.869254>

97. Wang Y, Meredith K, Zhou X, et al (2014) Numerical Simulation of Sprinkler Suppression of Rack Storage Fires. *Fire Saf Sci* 11:1170–1183. <https://doi.org/10.3801/IAFSS.FSS.11-1170>
98. Kakka P, Anupindi K (2020) Assessment of subgrid-scale models for large-eddy simulation of a planar turbulent wall-jet with heat transfer. *Int J Heat Mass Transf* 153:119593. <https://doi.org/10.1016/j.ijheatmasstransfer.2020.119593>
99. Morinishi Y, Tamano S, Nakabayashi K (2004) Direct numerical simulation of compressible turbulent channel flow between adiabatic and isothermal walls. *J Fluid Mech* 502:273–308. <https://doi.org/10.1017/S0022112003007705>
100. Yeoh GH, Yuen KK (2009) *Computational Fluid Dynamics in Fire Engineering*. Elsevier
101. Merci B, Beji T (2016) *Fluid Mechanics Aspects of Fire and Smoke Dynamics in Enclosures*, 1st ed. CRC Press
102. Tieszn SR, Gritzo LA (2008) Transport phenomena that affect heat transfer in fully turbulent fire. In: *Transport Phenomena in Fires*. pp 25–64
103. Spalding DB (1977) Development of the eddy-break-up model of turbulent combustion. *Symp Combust* 16:1657–1663. [https://doi.org/10.1016/S0082-0784\(77\)80444-X](https://doi.org/10.1016/S0082-0784(77)80444-X)
104. Magnussen BF, Hjertager BH (1977) On mathematical modeling of turbulent combustion with special emphasis on soot formation and combustion. *Symp Combust* 16:719–729. [https://doi.org/10.1016/S0082-0784\(77\)80366-4](https://doi.org/10.1016/S0082-0784(77)80366-4)
105. Bilger RW (1980) Turbulent flows with nonpremixed reactants. pp 65–113
106. McAllister S, Chen J-Y, Fernandez-Pello AC (2011) *Fundamentals of Combustion Processes*. Springer New York, New York, NY
107. Hamins A, Konishi K, Borthwick P, Kashiwagi T (1996) Global properties of gaseous pool fires. *Symp Combust* 26:1429–1436. <https://doi.org/10.1016/S0082->

108. Maragkos G, Merci B (2017) Large Eddy Simulations of CH₄ Fire Plumes. *Flow, Turbul Combust* 99:239–278. <https://doi.org/10.1007/s10494-017-9803-4>
109. Mcgrattan K, Floyd J, Forney G, et al (2003) Improved Radiation And Combustion Routines For A Large Eddy Simulation Fire Model. *Fire Saf Sci* 7:827–838. <https://doi.org/10.3801/IAFSS.FSS.7-827>
110. De Ris JL, Wu PK, Heskestad G (2000) Radiation fire modeling. *Proc Combust Inst* 28:2751–2759. [https://doi.org/10.1016/S0082-0784\(00\)80696-7](https://doi.org/10.1016/S0082-0784(00)80696-7)
111. Hidalgo JP, Torero JL, Welch S (2017) Experimental Characterisation of the Fire Behaviour of Thermal Insulation Materials for a Performance-Based Design Methodology. *Fire Technol* 53:1201–1232. <https://doi.org/10.1007/s10694-016-0625-z>
112. Hidalgo JP, Gerasimov N, Hadden RM, et al (2016) Methodology for estimating pyrolysis rates of charring insulation materials using experimental temperature measurements. *J Build Eng* 8:249–259. <https://doi.org/10.1016/j.jobbe.2016.09.007>
113. Marquis DM, Hermouet F, Guillaume É (2017) Effects of reduced oxygen environment on the reaction to fire of a poly(urethane-isocyanurate) foam. *Fire Mater* 41:245–274. <https://doi.org/10.1002/fam.2378>
114. Marquis DM, Batiot B, Guillaume E, Rogaume T (2016) Influence of reaction mechanism accuracy on the chemical reactivity prediction of complex charring material in fire condition. *J Anal Appl Pyrolysis* 118:231–248. <https://doi.org/10.1016/j.jaap.2016.02.007>
115. Hajduković M, Knez N, Knez F, Kolšek J (2017) Fire Performance of External Thermal Insulation Composite System (ETICS) Facades with Expanded Polystyrene (EPS) Insulation and Thin Rendering. *Fire Technol* 53:173–209. <https://doi.org/10.1007/s10694-016-0622-2>
116. Dréan V, Girardin B, Guillaume E, Fateh T (2019) Numerical simulation of the fire behaviour of facade equipped with aluminium composite material-based claddings—

- Model validation at intermediate scale. *Fire Mater* 43:839–856.
<https://doi.org/10.1002/fam.2745>
117. Hidalgo-Medina JP (2015) Performance-based methodology for the fire safe design of insulation materials in energy efficient buildings. The University of Edinburgh
 118. (2002) ISO 13785-1:2002 Reaction-to-fire tests for façades — Part 1: Intermediate-scale test. 10
 119. Blackshear PL, Murty KA (1965) Heat and mass transfer to, from, and within cellulosic solids burning in air. *Symp Combust* 10:911–923.
[https://doi.org/10.1016/S0082-0784\(65\)80234-X](https://doi.org/10.1016/S0082-0784(65)80234-X)
 120. Drean V, Schillinger R, Leborgne H, et al (2018) Numerical Simulation of Fire Exposed Facades Using LEPIR II Testing Facility. *Fire Technol* 54:943–966.
<https://doi.org/10.1007/s10694-018-0718-y>